國立交通大學

電機與控制工程學系

碩士論文

虛擬駕駛環境下腦波頻譜與反應時間之關聯

Changes in EEG Power Spectra Correlated with Driving Performance in Simulated Driving Environment

研 究 生：陳青甫

指導教授：林進燈　教授

中華民國九十八年七月

虛擬駕駛環境下腦波頻譜與反應時間之關聯

Changes in EEG Power Spectra Correlated with Driving Performance in Simulated Driving Environment

研究生：陳青甫　　Student: Ching-fu Chen

指導教授：林進燈　　Advisor: Chin-Teng Lin

國立交通大學

電機與控制工程學系

碩士論文

A Thesis
Submitted to Department of Electrical and Control Engineering
College of Electrical Engineering
National Chiao Tung University
in partial Fulfillment of the Requirements
for the Degree of
Master
in

Department of Electrical and Control Engineering

July 2009

Hsinchu, Taiwan

中華民國九十八年七月

虛擬駕駛環境下腦波頻譜與反應時間之關聯

研究生：陳青甫　　　　指導教授：林進燈教授

國立交通大學電機控制工程學系碩士班

摘　　要

疲勞駕駛不僅危險，並易造成交通事故，故瞌睡偵測系統的開發已成爲駕駛安全上重要課題。本實驗讓受測者在虛擬實境（VR）下，進行事件相關車輛偏移（event-related lane-departure）實驗，實驗中同時量測受測者的腦電波（EEG）訊號，以了解受測者駕車行爲反應與腦電波能量頻譜（power spectrum）之關聯。所錄得之腦電波訊號，在去除雜訊後，先以獨立成份分析（ICA）分出不同獨立訊號源，再將這些訊號源產生的腦波以時頻轉換（time-frequency transform）算出其頻譜。將所得頻譜依訊號源經過分群（clustering）並依相對應受測者反應時間排序後，觀察到兩側枕葉區（bilateral occipital）在 alpha 頻帶（band，頻率爲 8~12 赫茲）上的腦波頻譜能量會隨反應時間增加而上升，但若反應時間更長，則其能量會下降；而在 theta 頻帶（頻率爲 4~7 赫茲）的腦波頻譜能量則隨受測者反應時間增加持續而上升。實驗中亦觀察到若受測者反應時間增加，則該受測者通常會出現打瞌睡的行爲。因前述腦區之腦波能量改變現象不論實驗中是否提供動態刺激均可觀察到，故該腦區之腦波特徵可用於設計瞌睡偵測器，以保障駕駛人安全。

關鍵字：駕駛安全、疲勞駕駛、警覺程度、瞌睡偵測、事件相關車輛偏移實驗、駕駛行爲表現、虛擬實境（VR）、腦電波（EEG）、獨立成份分析（ICA）、時頻轉換（Time-Frequency transform）、腦波頻譜

Changes in EEG Power Spectra Correlated with Driving Performance in Simulated Driving Environment

Student: Ching-fu Chen Advisor: Professor Chin-Teng Lin

Department of Electrical and Control Engineering

National Chiao Tung University

ABSTRACT

Drowsy driving is a dangerous behavior and often results in a large number of fatal accidents each year; therefore, understanding the neural correlates of drowsy driving is crucial for the design and evaluation of devices for drowsiness detection. This study investigates the relation between spectral features of electroencephalographic (EEG) signals and driving performance. Subjects participated in long-haul simulated driving experiments on a motion platform, during which driving trajectories and 30-channel EEG signals were recorded simultaneously. Driving performance was measured by reaction time (RT) as defined in an event-related lane-departure paradigm. Following artifact rejection on behavioral and EEG data, independent component analysis (ICA) was used to decompose EEG signals into independent brain processes, and power spectra were computed from the activation time course of each independent component. Independent components with similar features, including topographic maps, dipole sources, and power spectra, were then grouped into clusters across subjects.

Across subjects, an independent component with sources in the bilateral occipital regions showed prominent changes in EEG power spectra as reaction time to lane-departure events increased. The alpha-band (8-12 Hz) power increased as reaction time increased and started to decrease as reaction time further increased (> 3 sec); however, theta-band (4-7 Hz) power increased monotonically as reaction time increased. These spectral features were consistent in both motionless and motion conditions. Finally, the results of this study may provide useful information, such as the selection of optimal electrode locations and frequency bands, for the development of drowsiness detection devices.

Index terms: Driving Safety, Drowsy Driving, Vigilance Level, Drowsiness Detection, Event-Related Lane Departure Paradigm, Driving Performance, Virtual-Reality (VR), Electroencephalographic (EEG) Signals, Independent Component Analysis (ICA), Time-Frequency Transform, EEG Power Spectrum

誌　謝

在完成論文的過程中，我受到很多人的協助；有大家的幫忙協助，才能順利完成這項研究。首先，我要感謝我的家人，並把這份論文獻給他們。我的家人除了讓我在整個過程中不用煩惱生活上的瑣事外，他們更在低潮時給我鼓勵，讓我有動力繼續前行。在此要向我的家人再次表達由衷的感謝。感謝美國加州大學聖地牙哥分校的黃瑞松博士，在整個研究過程中，黃博士十分耐心地指導我，爲我釋疑，並仔細檢查研究中的各個步驟。而指導教授——林進燈教授及實驗室的柯立偉博士，除了爲提供良好的研究環境不遺餘力外，並指引我研究的方向；同樣是美國加州大學聖地牙哥分校的鍾子平教授和段正仁博士，及交大的曲在雯教授，在研究結果的詮釋上提出不少建議，並指出我的盲點。感謝實驗室的黃騰毅學長在實驗場景上的設計及調整，李昂穎、莊謹譽、葉人慈三位學弟在實驗進行及資料分析上的支援及協助，及鄭仲良學長在實驗技巧和資料提供上給予的幫忙。最後，我要感謝實驗室其他學長姊、同學、學弟妹在資料分析及詮釋上的經驗分享，及實驗室助理在行政事務上的協助，謝謝大家。在此再向幫助過我的各位表達由衷感謝。

Acknowledgements

In the process of finishing this research, I received the help from many people. With their help, I can finish this study smoothly. In the beginning, I'd like to make special thank to my dear families and dedicate this thesis to all of them. Because of them, I didn't have to worry about my livings throughout the whole process; in addition, when I was frustrated, they consoled and cheered me and gave me more strength. I'd like to say "thank you" to all of them. I'd like to thank Doctor Ruey-Song Huang (黃瑞松博士), who instructed me with great patient and scrutinized the procedures for data analysis carefully. I'd also like to thank Professor Ching-Teng Lin (林進燈教授) and Doctor Li-Wei Ko (柯立偉博士) for the help in the great environment in the lab and the insights in the direction of my study, and Professor Tzyy-Ping Jung (鍾子平教授), Doctor Jen-Ren Duann (段正仁博士), and Professor Tzai-Wen Chiu (曲在雯教授) for the suggestions in interpreting results. Moreover, I'd like to thank Teng-Yi Huang (黃騰毅學長) for the programming of experiment environment, teammates Yang-yin Lee (李昂穎), Chin-yu Chuang (莊謹譽), and Ren-cih Yeh (葉人慈) for the assistances in data analysis and further experiments, and Jong-Liang Jeng for the instructions in skills in conduction experiments and experiment data. Finally, I'd like to thank other lab researchers for sharing their experiences and other suggestions in their own studies to make this thesis even better, and the assistants in the lab for other helps. Thank you. Thank you very much.

Contents

Lists of Tables

Lists of Figures

Abbreviations

EEG: electroencephalographic

ICA: independent component analysis

IC(s): independent component(s)

RT: reaction time (the reaction time in a trial)

RTs: reaction time (the reaction time in the trials in a group)

VR: virtual reality

LDWS: lane departure warning system

ESC: electronic stability control

EOG: electrooculography

HRV: heart-rate variability

DOF: degree of freedom

DFT: discrete Fourier transform

Chapter I Introduction

Drowsy driving is a dangerous behavior and results in a large number of fatal accidents each year. When the drivers are drowsy, they have 1) impaired reaction time (RT), judgment, and vision, 2) problems with information processing and short-term memory, 3) decreased performance, vigilance and motivation, and 4) increased moodiness and aggressive behaviors [1]; in addition, they also exhibit dangerous behaviors like running off the road, crossing the center line, or wandering into other lanes or onto the shoulder during drowsy periods [2]. It was reported that in 2008, 54% of adult drivers in the US felt drowsy while driving a vehicle, and 28% of them actually fell asleep at the wheel; moreover, of those who had nodded off, over 50% said they have done so at least once a month [3]. In order to improve driving safety and reduce casualties, it is of great importance to study the neural correlates of drowsy driving, develop devices for monitoring the driver's vigilance state, and provide timely and effective feedback to the driver.

Several techniques have been developed for drowsiness detection. One of them monitors the driver's behavior or the vehicle's lane position, such as the lane-departure warning system (LDWS) [4][5], and other techniques monitor the driver's physiological activities such as heart-rate variability (HRV) and electrooculography (EOG) [6]. The former mainly integrates image-processing based methods to detect lane marking (boundary) and monitor the driver's activities such as yawning, head positions, or eye blink duration via optical sensors or video cameras [7][8]; however, image- or video-based techniques are sensitive to external weather conditions (e.g., rain or snow) and the driver's posture inside the car. Although the monitoring of physiological signals, such as HRV and EOG, does have the same limitation as image- or video-based techniques, the temporal resolution of these physiological signals is low, making them less effective in the tracking of vigilant states. Among other physiological signals, electroencephalography (EEG) is the most direct and effective measures of vigilant states; however, EEG signals are usually recorded from dozens of scalp electrodes and sampled at 100-500 Hz, which is less viable for on-line signal processing. Owing to the advances in signal acquisition devices and computer speed, recently, real-time analysis and automatic detection of EEG patterns of drowsiness have become more viable [9][10][11].

Numerous studies have suggested that changes in EEG power spectra are related to vigilance and drowsiness. For example, Beatty et al. demonstrated augmented occipital theta activities when the radar operators were less vigilant [12]. Huang et al. demonstrated tonic EEG power increase in low-frequency bands in the occipital cortex during high-error periods in a continuous tracking task [13], and they also demonstrated similar tonic EEG power increase in low-frequency bands in the occipital cortex in simulated driving experiments [14]. In addition, Lin et al. demonstrated the correlation between alpha and theta band power and driving error, defined as mean deviation from lane center in each moving window [9][15], in a virtual-realty (VR) environment. To this day, most studies on drowsy driving have conducted experiments in static laboratory setting; however, in the real world, drivers receive kinesthetic stimuli, e.g. vibration on the road, in addition to visual and auditory stimuli. It does not know the effect of kinesthetic stimuli on the EEG power spectra and the accuracy of drowsiness detection, but conducting experiments on the road could be costly and dangerous to the subjects; hence, a dynamic laboratory setting, e.g. a VR environment with a motion platform, is necessary in investigating this issue.

In this study, subjects participated in simulated nighttime driving experiments on a motion platform in a well-controlled VR-based environment [9][15]. An event-related lane-departure paradigm [16][17] was used to continuously monitor the subjects’ arousal states, as measured by reaction time to perturbing events on the road. Subjects participated in different sessions, during which the motion platform was active (motion condition) or inactive (motionless condition), and their driving trajectories, behavioral responses, and 30-channel EEG signals were recorded simultaneously. Independent component analysis (ICA) was used to decompose the 30-channel EEG signals into temporally independent processes, whose sources originated from multiple brain regions, and power spectra were computed from the activation time course of each independent component. Finally, independent components with similar features, such as topographic maps, dipole sources, and power spectra, were grouped into clusters across subjects.

This study aims to 1) identify independent brain processes in different cortical regions whose EEG power spectral changes were related or not related to drowsiness, 2) find the trends of different frequency bands in EEG power spectra from alertness to drowsiness across subjects and sessions, and identify frequency bands that are most suitable for drowsiness detection, and 3) compare the above trends in motionless and motion conditions, and find the influence of kinesthetic inputs on EEG power spectra. Finally, the results of this study may provide insights into the design and assessment of drowsiness detection systems for real-life driving.

Chapter II Experiment Design and Setup

2.1 VR-Based Driving Simulator and Steward Motion Platform

Simulated driving experiments were conducted in a VR-based driving simulator. A real car body was mounted on a six degree-of-freedom (DOF) Steward motion platform (Figure 1 and Figure 2), which simulated the vibration caused by uneven road surface as well as kinesthetic force during real-life driving. Seven video projectors were used to generate the 360-degree VR scene of night-time driving in a darkened room. This setup provided the subjects with immersive environment and enables the experimenters to control the experiment in a different room.

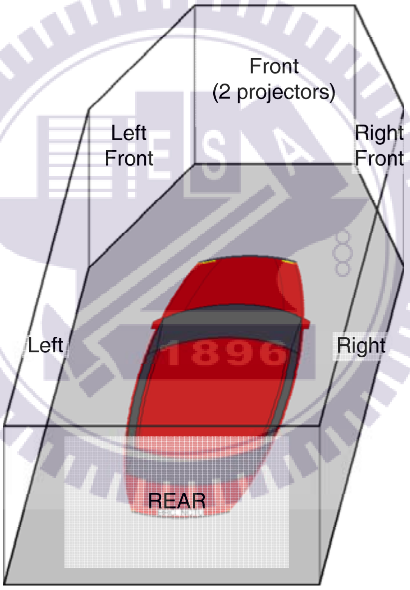

Figure 1: The layout of the screens in the VR environment at Brain Research Center (BRC), National Chiao Tung University (NCTU). The texts indicate the position of the screens.

Figure 2: A car body mounted on a 6-DOF Steward motion platform.

2.2 Event-Related Lane-Departure Paradigm

The event-related lane departure paradigm [16][17] was implemented in the VR-based driving simulator using WorldToolKit (WTK) R9 Direct and Visual C++. The paradigm was designed to quantitatively measure the subject's reaction time to perturbations during continuous driving. Figure 3 shows a bird's eye view of this task. In this setup, every a few seconds, the car is programmed to randomly drift to the left or right out of a cruising lane with equal probability. Without these lane-departure events, the subject might fall asleep while the car continues to move straight in the lane without deviation in a driving simulator, making it difficult to objectively monitor the subject vigilance level. Following each deviation, subjects were required to steer the cars back to the approximate center of the cruising lane as quick as possible using the steering wheel, and were instructed not to make fine adjustment to the position of the cars and hold on to the wheel after the car returns to the center of the cruising lane. If the subject does not respond promptly, the vehicle will eventually hit the virtual curb on either side without crashes and continue to move along the curb even the subject falls asleep. Such experimental design allows the observation of continuous transition from complete alertness to deep drowsy states.

Each lane-departure event is defined as a “trial” which includes three critical moments: “deviation onset” is the moment when the car starts to drift away, “response onset” represents the moment when the subject perceives the drift and begins to steer the cars back to the cruising lane, and “response offset” is the moment when the car returns to the center of the cruising lane, and the subject ceases to rotate the steering wheel. The next lane-departure event occurs again 5~10 sec after the “response offset.” The reaction time is defined as the interval between deviation onset and response onset in a trial.

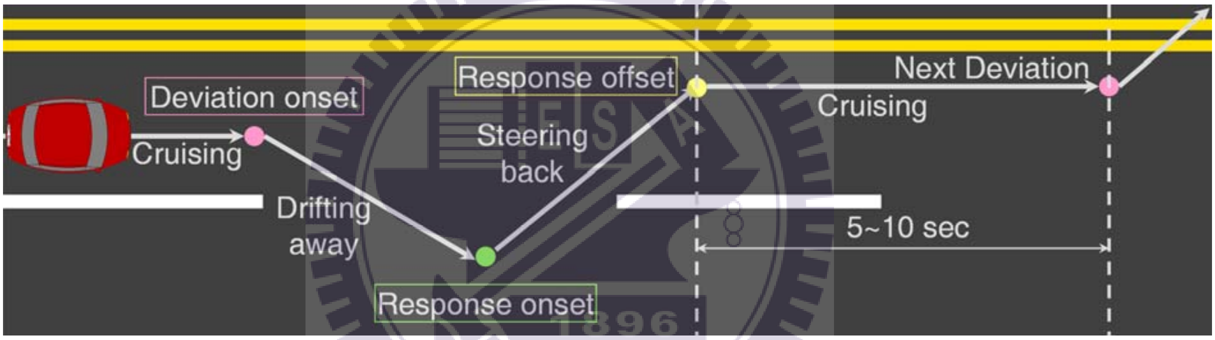

Figure 3: A bird’s eye view of the event-related lane-departure paradigm. Figure recreated with permission from [16][17].

In order to test the effect of kinesthetic inputs on brain activities and drowsiness, subjects participated in “motionless” and “motion” sessions on different days. The 6-DOF motion platform generated kinesthetic stimuli only in the “motion” sessions. In the “motionless” sessions, the platform was stationary, and no kinetic stimuli were given to the subjects.

2.3 Subjects

Eleven healthy male subjects with normal or corrected-to-normal vision were paid to participate in the experiments. All of them were recruited from NCTU, and none of them were BRC members at the time they participated in the experiments.

None of them reported psychiatric or sleep disorders. Subjects were given instruction on how to respond to the events before participating in the experiment for the first time. All subjects have participated in the “motionless” session, and seven of them also participated in the “motion” session.

2.4 EEG Recording

The EEG data were recorded at 500 Hz sampling rate from an electrode cap (Neuromedical Supplies 32-channel Quik-Cap) based on the international 10-20 system [18] using a NeuroScan NuAmps amplifier with a band-pass filter (0.1 to 50 Hz). Two reference channels, A1 and A2, were placed on the left and right mastoids, respectively. The impedance of each electrode was ensured to be less than 5k ohms before the EEG acquisition began.

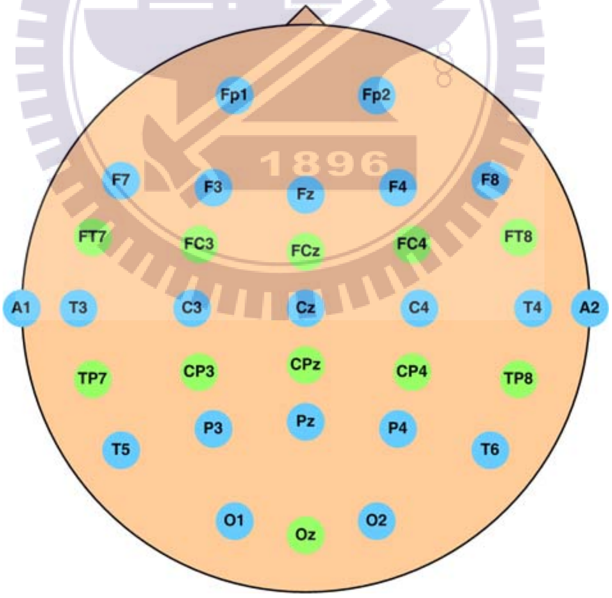

Figure 4: The layout of electrodes on the EEG caps used in the experiments. The blue electrodes are the ones in the international 10-20 system, and the green ones are additional electrodes on the cap.

Chapter III Data Analysis

In this study , all data analyses and signal processing were implemented by scripts running in MathWorks MATLAB (R2007a) and the EEGLAB Toolbox (version 5.03) developed by the Swartz Center for Computational Neuroscience, the University of California San Diego (UCSD) [19]. Figure 5 shows the flowchart of data analysis and signal processing.

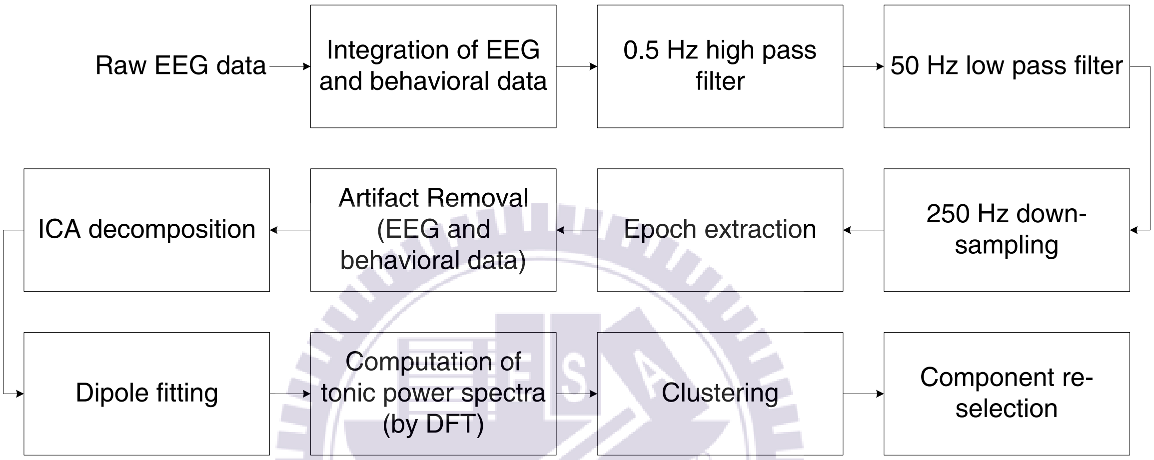

Figure 5: The flowchart of data analysis and signal processing.

3.1 Integration of EEG and Behavioral Data

During each experiment, the stimulus computer that generated the VR scene recoded the trajectories of the car as well as the events with time points in a “log” file. The stimulus computer also sent synchronized triggers (which were also recorded in the “log” file) to the Neuroscan EEG acquisition system. At the same time, the Neuroscan system recoded the EEG data with the time stamps of those trigger in an “ev2” file. Since the numbers of time points in both recorded files were different, the first step was to integrate these two files into a new file with aligned event timing and behavioral data. The new event file was then imported by EEGLAB in MATLAB.

3.2 Epoch Extraction

An epoch is a segment of multi-channel EEG signals time-locked to a specific type of behavioral event. Since there may be more than one event in a trial, the continuous EEG signals in a trial can be extracted into different types of epochs. In order to observe the fluctuation in EEG signals to specific events, the continuous 30-channel EEG signals were extracted into eight-second epochs, time-locked to 1 sec before and 7 sec after each deviation onset.

The “tonic” and “phasic” activities in the recorded data are defined as below [13]. The “tonic” activities in EEG data refer to the longer-term changes in baseline arousal levels. In this study, tonic activities were measured from the cruising period before the deviation onset in each epoch. The “phasic” EEG activities refer to transient event-related brain dynamics time-locked to the deviation onset or response onset/offset.

3.3 Artifact Removal

3.3.1 Removal of Behavioral Artifacts

Two types of abnormal trials in the recorded behavioral data (vehicle trajectories and RTs) were rejected before further analysis. First, those trials with RTs shorter than 0.3 sec were rejected due to the subject’s unintentional responses or the jitters of the steering wheel. Second, when the car returned to the lane center, the trajectories in some trials exhibited “overshoot” or zigzag patterns, making it difficult to clearly define the exact timing of response offset, and thus hard to interpret EEG data; therefore, those trials that did not show “flat” trajectories between the current response offset and the next deviation onset were rejected. Figure 6 demonstrates the removal of abnormal trials in behavioral data. Trials 163 and 164 show typical patterns of trajectory of a lane-departure event and were included in the data analysis, and trials 159, 160, and 162 were rejected because the subject continued to turn the wheel after response offsets (as indicated in blue dots). In some trials, the steering wheel was not turned into the exact central position (zero angle) after the subject cease to steer, but the computer program misinterpreted the nonzero angle as rotation and made the car continue to drift. For example, trial 161 shows a linear drift during the pre-deviation period, which could be assumed that the subject was not actually steering, and thus this trial was not rejected.

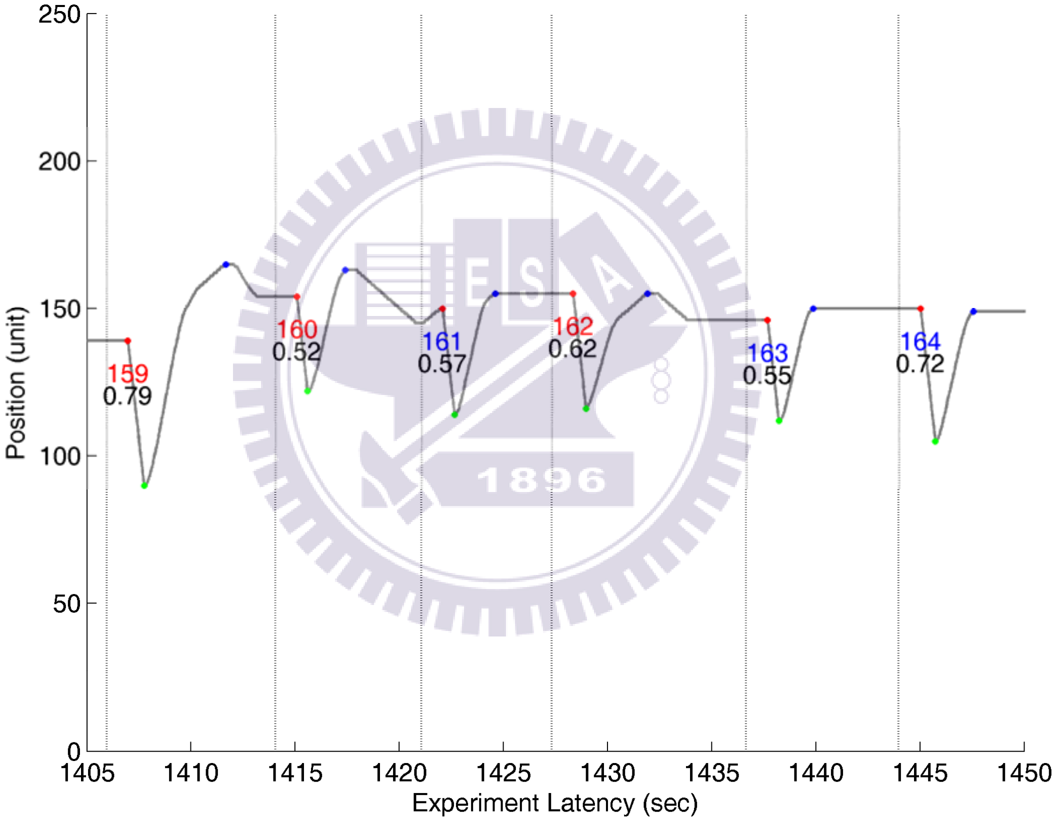

Figure 6: A segment of the driving trajectory in a representative session. X- and y- axes: experiment duration (in seconds) and the lane position of the car (in units), respectively; gray curve: driving trajectory; red, green, and blue dots: driving events: deviation onsets, response onsets, and response offsets, respectively; vertical dotted lines: the beginning of each epoch (one second before deviation onset); numbers below the red dots: indices of trials (red: rejected trial; blue: remained trials after artifact removal) and corresponding RTs (black).

3.3.2 Removal of EEG Artifacts

In this study, the event-related lane departure task required frequent manual responses using the steering wheel, and sometimes involved body movements to counterbalance with the forces of motion platform during “motion” sessions. These movements often resulted in severe noise in the EEG signals. In addition, a few electrodes lost skin contacts in some periods or throughout the experiment and resulted in signals with extreme values in the recorded data. These artifacts could not be dissociated from other brain processes using independent component analysis (ICA), and must be removed before further analysis. Figure 7 demonstrates an example of artifact removal on the recorded EEG data. The following criteria were applied to artifact removal in EEG data: 1) channels with extreme values due to poor skin contact throughout the entire or most parts of the session, and 2) epochs with severe fluctuations across most EEG channels. In Figure 7, epochs 154-156 were rejected due to large fluctuations in channels Fp1, Fp2, F3, and F4; in addition, epoch 158 was rejected because it not only showed large fluctuations on channels Fp1, Fp2, F3, and F4, but also showed widespread noise across all channels.

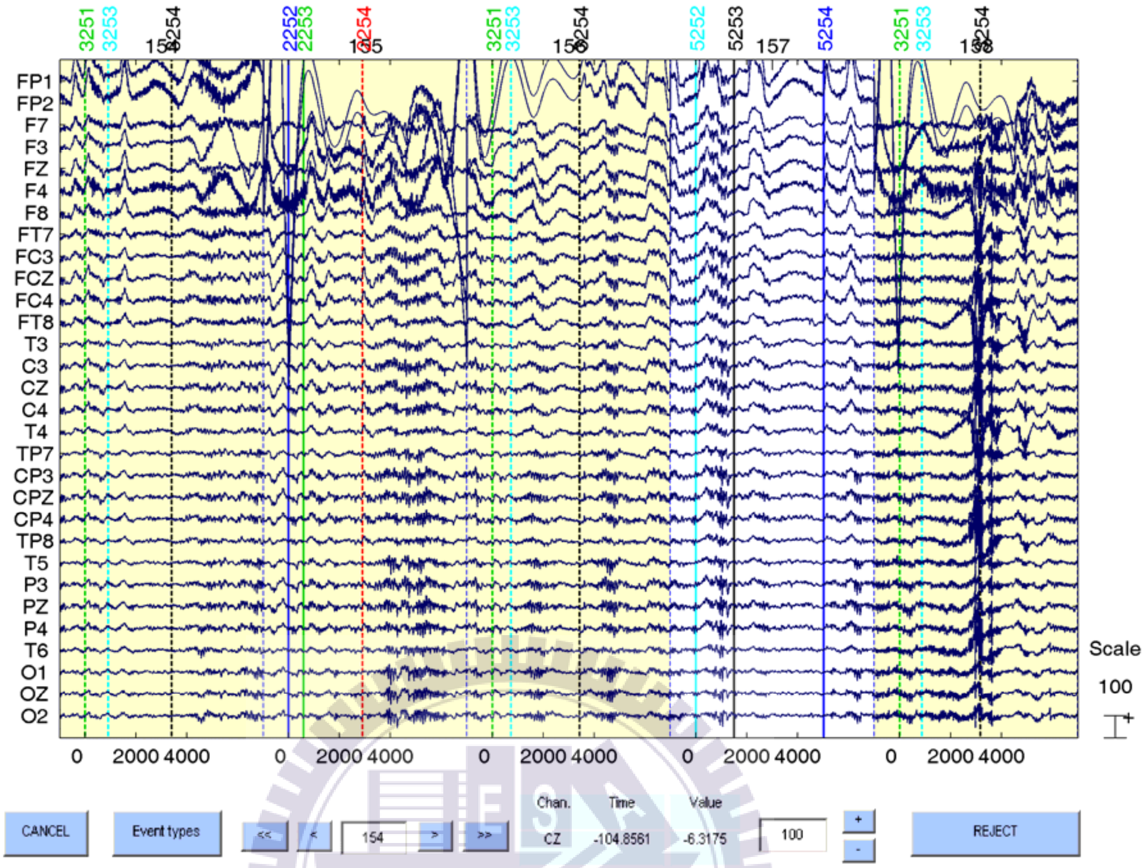

154

Chan. CZ
Time -104.8561
Value -6.3175
100

Figure 7: An example of artifacts removal of the recorded EEG signals. This figure is a screen snapshot of the `eegplot()` *function in the EEGLAB toolbox. Horizontal and vertical axes: latency of epochs (in milliseconds, 0: deviation onset of each epoch) and channels, respectively; horizontal traces: the recorded EEG signals; vertical lines: deviation onset, response onset, response offset, and boundaries of epochs; numbers on top: trial indices (horizontal) and event types (vertical).*

3.4 Independent Component Analysis (ICA)

3.4.1 Background and Algorithm of Independent Component Analysis

ICA algorithms are a family of related methods for unmixing linearly mixed signals using only recorded time course information (that is, “blind” to detailed models of the signal sources as required by earlier signal processing approaches) [20]. Four main assumptions underlie ICA decomposition of EEG time series: 1) signal conduction times are equal, and summation of currents at the scalp sensors is linear, 2) spatial projections of components are fixed across time and conditions, 3) source activations are temporally independent of one another across the input data, and 4) statistical distributions of the component activation values are not Gaussian [21]. Given a matrix, **W**, a vector *w*, a random vector, $\mathbf{x} = [x_1 \dots x_N]^T$, and the linear transform, $\mathbf{u} = \mathbf{Wx} + w$, the objective of ICA decomposition is to find the elements in $\mathbf{u} = [u_1 \dots u_N]^T$ are statistically independent. ICA imposes that the multivariate probability density function (p.d.f.) of **u** factorized as $f_{\mathbf{u}}(\mathbf{u}) = \prod_{i=1}^{N} f_{u_i}(u_i)$, and makes the mutual information between the u_i go to 0: $I(u_i, u_j) = 0 \; \forall i, j$. In Informax ICA, which was adopted in this study, the input signals are scaled and shifted to make each of the unknown independent components, u_i, have the same form of cumulative density function (c.d.f.) with the form $F_u(u)$. Next, ICA is performed by maximizing the entropy H(y) of a non-linearly transform vector $\mathbf{y} = F_u(\mathbf{u})$ and thus yields stochastic gradient ascent rules for adjusting **W** and *w*:

$$\Delta \mathbf{W} \propto \left[\mathbf{W}^T\right]^{-1} + \hat{\mathbf{y}}\mathbf{x}^T, \Delta w \propto \hat{\mathbf{y}}$$

(1)

where $\hat{\mathbf{y}} = [\hat{y}_1 \dots \hat{y}_N]^T$, and

$$\hat{y}_i = \frac{\partial}{\partial y_i} \frac{\partial y_i}{\partial u_i} \qquad [\text{which if } \mathbf{y} = F(\mathbf{u})] \qquad = \frac{\partial f_u(u_i)}{\partial F_u(u_i)}$$

(2)

Instead of using the original c.d.f. of the original signals, the applied c.d.f. in ICA training is $y_i = \left(1 + e^{-u_i}\right)^{-1}$; henceforth, $\hat{y}_i = 1 - 2y_i$ and thus resulting a simple form in this algorithm. These results were obtained even though the p.d.f. of the original signals may not exactly match by the gradient of the logistic function [22].

3.4.2 Independent Component Activations and Topographic Maps

After artifact rejections, the remained channels and epochs were concatenated into a matrix, **x**, of size [channels × epochs] and subjected to ICA decomposition using the `runica()` function of the EEGLAB toolbox. ICA finds an “unmixing” matrix, **W**, which decomposes or linearly unmixes the multi-channel EEG data, **x**, into a sum of maximally temporally independent and spatially fixed components **u**, where $\mathbf{u} = \mathbf{W}\mathbf{x}$. Each row of the output data matrix, u (or rows of `icaact` in the EEGLAB dataset), is the activation time course of each independent component. Each column of the inverse of matrix, **W** (or `icawinv` in the EEGLAB dataset), indicates the activation weights distributed across electrodes for each independent component, which can be rendered as a two-dimensional (2-D) topographic map on the scalp.

Figure 8 shows 2-D topographic maps of 30 independent components in a representative session. Components 2, 3, 4, 6, 7, 8, 9, 10, 11, 14, 18, and 21 are considered as potentially related to brain processes, and others are considered non-brain artifacts (blinks, eye movements, muscle artifacts, single-channel noise, etc.).

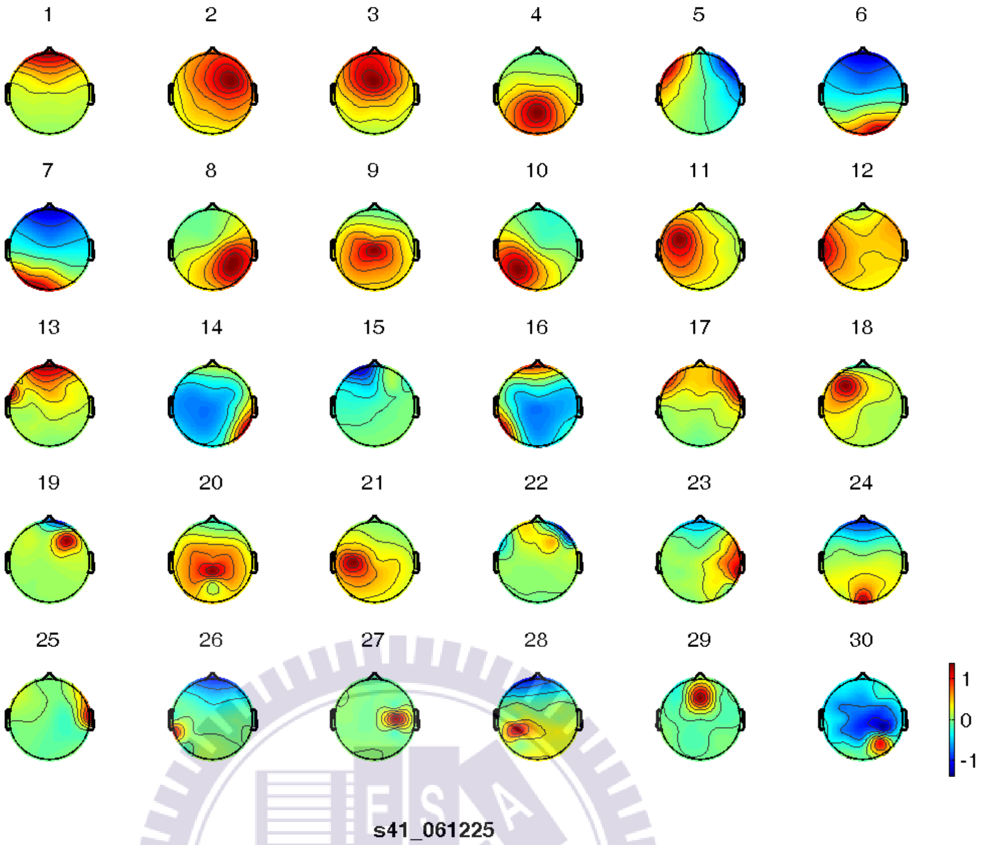

Figure 8: Topographic maps of ICA decomposition in a representative session.

3.5 Dipole Fitting

Dipole fitting is one of the methods to solve the inverse problem: given an EEG scalp distribution of activity observed at given scalp electrodes, any number of brain source distributions can be found that would produce it [23]. After applying ICA decomposition, many i have scalp maps that nearly perfectly match the projection of a single equivalent dipole on the cortex, and this finding is consistent with their presumed generation via partial synchrony of local field potential (LFP) processes within a connected domain or patch of cortex. The problem of finding the location of a single equivalent dipole generating a given dipolar scalp map is well posed; however, the location of the equivalent dipole for synchronous LFP activity in a "cortical patch" will in general not be in the center of the active cortical patch, especially the patch is radially oriented (e.g. on a gyrus, thus aimed toward the supervening scalp surface), the equivalent dipole location tends to be deeper than the cortical source patch [23]. In this study, the dipole source location of each independent component was estimated using the resulting weight matrix of ICA decomposition and the 3-D positions of electrodes. Dipole fitting was implemented using the `dipfit` plugin in EEGLAB, which finds the optimal dipole location and moments (vectors) that maximally account for the independent component activities with minimum residual variance.

3.6 Computation of Tonic Power Spectra

3.6.1 Time-Frequency Transform

Time-frequency transform is a spectrotemporal decomposition technique that evaluates event-related perturbations in the power spectra (as well as phase and coherence perturbations; not discussed in this study) of single-channel EEG signals or activation time courses of single IC [19]. Figure 9 shows the procedure of time-frequency transform. For each single-channel epoch, the time series are chronically divided into designated numbers of overlapped sub-windows, and the power of each sub-window is then computed by discrete Fourier transform (DFT) using `timefreq()` function in EEGLAB and `fft()` function in MATLAB in this study. Finally, a matrix with size [frequency bins × time windows] was obtained for each epoch. The same procedures were applied to all epochs for all EEG channels or IC activations.

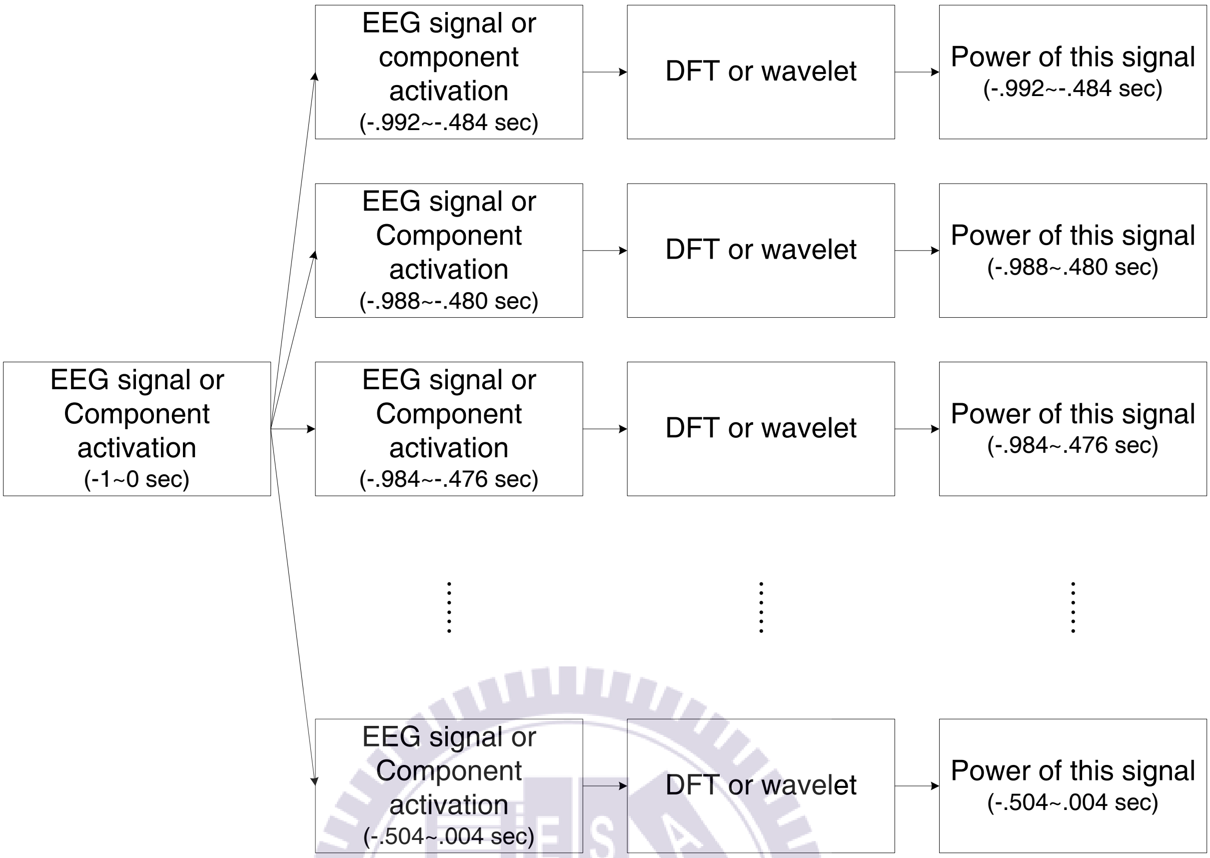

Figure 9: The procedures of time-frequency transform of a single-trial and single-channel EEG signals or ICA activation time courses in an epoch. In this research, time-frequency transform was applied only on ICA component activations and using DFT to compute power spectra. Assume this epoch is -1~0 sec (0: deviation onset), and the output is set to 100 time points. The intervals of each sub-window were reported by the function `timefreq()`*.*

3.6.2 Tonic Power Spectra

The goal of this study is to investigate the relation between the changes in tonic EEG power spectra of independent component activations and the fluctuation of driving performance (as measured by reaction time). In order to minimize the effects of phasic EEG power fluctuations during lane departure events, tonic power spectra were computed only from the cruising period before each deviation onset [14]. Figure 10 shows the procedures for computing tonic power spectra, spectral normalization, and statistical tests. For each subject (session), logarithmic (log) tonic power spectra were computed from a 1-sec window before the “deviation onset” in each 8-sec epoch extracted from each IC activation time courses using DFT (window size: 256 ms; 44 frequency bins between 2.93 and 44.92 Hz, the 2.93-Hz bin was excluded in plotting power images since this frequency bin was beyond the range in this study; 100 time steps between -742.976 and -253.204 sec where 0 sec: deviation onset). The average power spectra were then obtained by averaging across time points to get a mean baseline. Detailed output frequency bins and time points are shown in Table A1 and Table A2).

For each IC of each subject, the tonic power spectra of all epochs (trials) were sorted by their RTs, and then normalized by subtracting the mean power spectra of the “alert trials” with the shortest RT (first 10% of all RT-sorted trials). In this study, the mean power spectra of the alert trials are defined as the “alert baseline power spectra.” Finally, moving average (window size: 10% of total trials; stepping at one trial) was applied to the sorted, normalized power spectra. A two-tailed *t*-test (`ttest2()` function in MATLAB) was used to assess if the mean power spectra in each moving window was statistically different from those of the alert trials ($p < 10^{-4}$, corrected with a Bonferroni multiple comparison method).

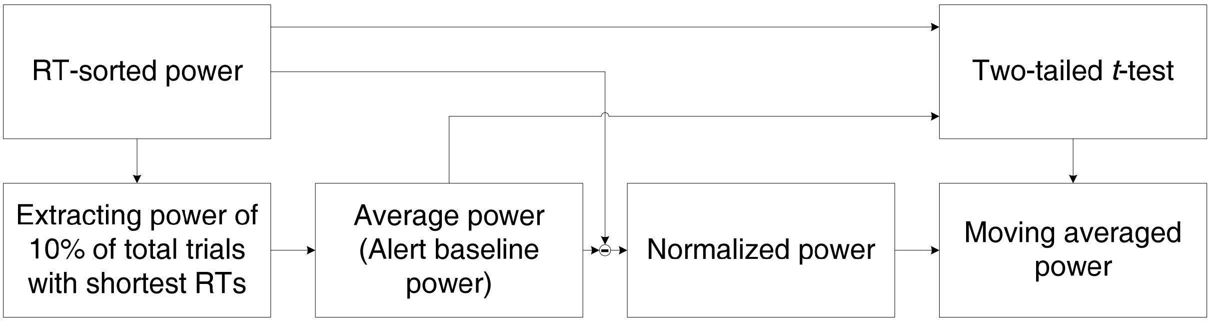

Figure 10: The flowchart of computing tonic power spectra.

3.7 Independent Component Clustering

3.7.1 Clustering and Re-Selection of Independent Components

In order to characterize the common pattern of spectral activities of similar ICs from different subjects and sessions, these ICs were manually grouped into several IC clusters according to their 2-D topographic maps. Next, initial clustering results were further refined iteratively based on dipole source locations and alert baseline power spectra of ICs in each IC cluster. Components that showed abnormal patterns in their topographic maps, dipole source locations, or power spectra deviated from the cluster's mean were considered outliers. These outliers were rejected from the cluster, and the mean alert baseline power spectra were recomputed from the remaining components in the cluster. In this study, eight IC clusters of brain-related processes were obtained.

3.7.2 Group Trend of Tonic Power Spectra

In order to find the group trend of tonic power spectra, all trials (epochs) in the same IC cluster were grouped and sorted by reaction time, which was used as a common behavioral index to compare the EEG power spectra at similar alertness levels across subjects. The procedures for computing group tonic power spectra from clustered data and statistical tests were slightly different from those applied to single-subject data. In single-subject data, the power spectra of each trial were normalized by the mean power spectra of "alert trials" in the same subject; in the clustered data, the power spectrum of each trial in a moving window was normalized by the mean power spectra of alert trials from its original session, not the mean power of "alert trials" in this cluster. For example, if a trial was from session 3, the power spectra of this trial were normalized by the alert baseline power spectra in that session. In single-subject data, the significance level was estimated by comparing the mean power spectra of trials in a moving window with the alert baseline power spectra from the same session; in the clustered data, the significance level ($p < 10^{-10}$, corrected) was estimated by comparing the mean power spectra of trials from multiple sessions in a moving window with the weighted baseline (alert) power spectra from the trials' original sessions. For example, in a moving window with trials 30% from session 1, 30% from session 3, and 40% from session 5, the significance level of this window was estimated by comparing its mean power spectra with the weighted baseline (alert) power from sessions 1, 3, and 5 in consideration of the proportion of trials.

Chapter IV Results

4.1 Motionless Datasets

4.1.1 Behavioral Data

Table 1 shows the distribution of behavioral data of individual subjects in the "motionless" condition. The shaded rows show the numbers of trials remained after EEG and behavioral artifact removal. Subjects are sorted in descending order by their drowsiness levels, defined as the percentage of remained trials with RT > 3 sec. In total, 48.66% of original trials in all subjects remained due to severe artifacts in the driving experiments. The car drifted to the left (right) in 49.68% (50.32%) of all the remained trials.

TABLE 1: BEHAVIORAL DATA OF MOTIONLESS DATASETS

Subject Index	Trials	Data Length (sec)*	Trials Re-mained (%)**	Min. RT (sec)	Max. RT (sec)	Avg. RT (sec)	SD of RT (sec)	Med. of RT (sec)	Trials w. RT > 3 sec (%)	Dev. to Left (%)
s40_070207	437	6552.12	--	0.02	110.52	6.09	9.93	2.06	43.71	48.05
	222	--	50.80	0.38	46.37	7.61	9.37	3.38	**52.70**	45.95
s44_070325	568	6353.32	--	0.02	49.75	2.16	3.43	0.87	21.13	52.11
	223	--	39.26	0.58	49.75	2.74	4.74	0.84	**26.91**	41.70
s36_061221	592	6918.08	--	0.02	109.35	3.09	5.98	1.19	25.00	55.24
	336	--	56.76	0.64	32.15	3.38	4.74	1.24	**26.49**	54.46
s42_070105	548	6514.88	--	0.05	628.43	3.45	26.98	1.25	23.54	51.09
	197	--	35.95	0.62	66.26	2.81	5.29	1.50	**26.40**	50.76
s01_061102	533	6304.28	--	0.02	40.17	2.94	4.23	1.39	19.14	45.03
	287	--	53.85	0.62	40.17	3.24	4.69	1.35	**21.60**	44.95
s35_070322	555	5968.00	--	0.02	56.98	2.44	5.21	0.79	15.32	52.61
	195	--	35.14	0.47	56.98	2.33	6.15	0.73	**12.82**	60.00
s32_061031	550	7301.76	--	0.02	30.79	3.16	3.89	1.90	25.64	49.09
	250	--	45.45	0.64	6.64	1.85	0.84	1.67	**10.40**	48.00
s05_061101	716	6592.20	--	0.10	8.46	1.22	1.12	0.88	6.42	52.37
	402	--	56.15	0.55	8.01	1.31	1.24	0.90	**7.71**	50.00
s43_070208	628	5823.40	--	0.02	26.06	1.24	1.92	0.77	6.21	51.91
	430	--	68.47	0.50	26.06	1.39	2.22	0.79	**7.67**	53.72

s41_061225	670	6353.32	--	0.02	10.65	1.12	1.05	0.75	5.82	49.55
	282	--	42.09	0.32	8.62	1.17	1.15	0.74	**7.45**	47.16
s31_061103	566	6231.08	--	0.03	11.23	1.78	1.35	1.35	10.95	48.06
	272	--	48.06	0.72	8.68	1.61	1.16	1.22	**7.35**	47.43
All subjects	6363	--	--	0.02	628.43	2.46	9.02	1.05	17.32	50.32
	3096	--	48.66	0.32	66.26	2.50	4.51	1.05	**17.31**	49.68

Note: shaded areas: distribution of the trials remained after artifacts removal. *: original datasets. **: datasets after artifacts removal.

Figure 11 shows the cumulative distribution of sorted reaction time across subjects in the “motionless” datasets. The x- and y- axes are reaction time (in log scale) and percentage of RT-sorted index, respectively, and the vertical dashed line indicates 3-sec RT. The curve shows an approximate bi-linear distribution of RTs (when the x-axis is plotted in linear scale). Only 20% of all remained trials have RTs longer than 3 sec, which suggest the subjects were not very drowsy in these trials.

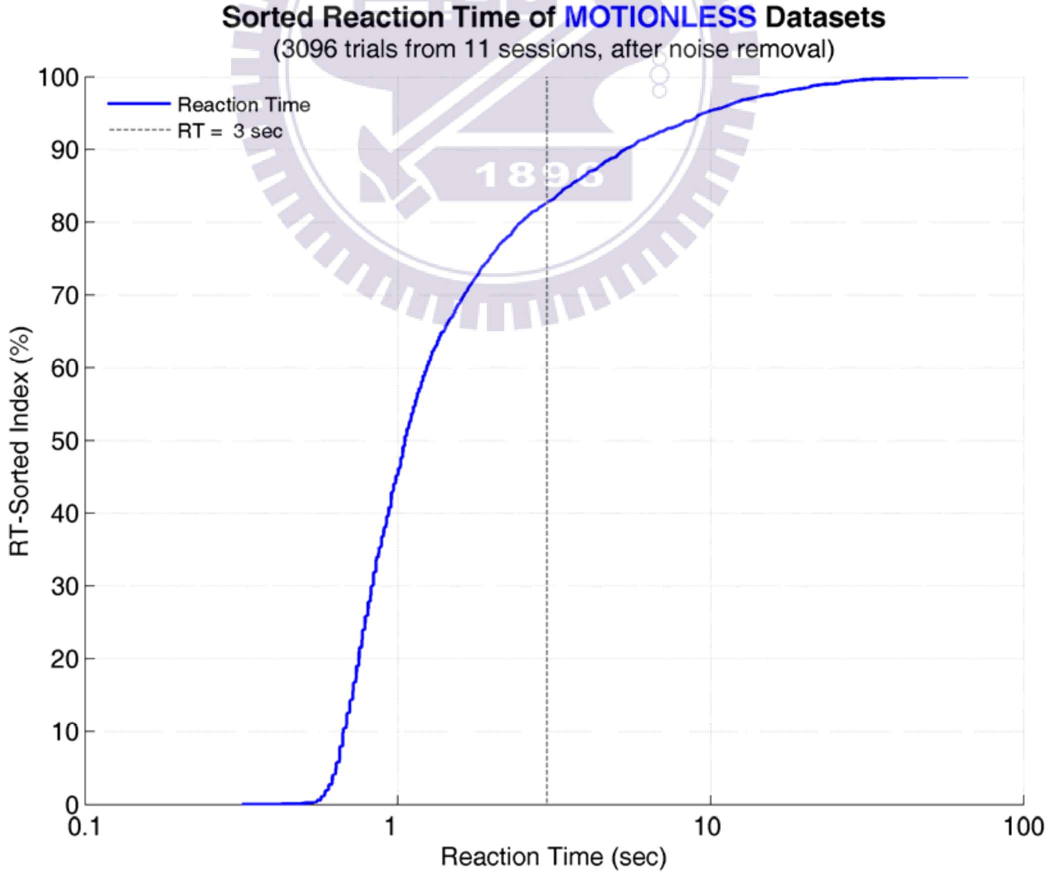

Figure 11: Cumulative distribution curve of sorted reaction times in the motionless datasets.

4.1.2 Clustered Scalp Maps and Dipole Locations

Eight clusters of independent components with dipole sources located in the frontal, central, parietal, somatomotor, and occipital regions were identified based on their scalp maps from the results of ICA decomposition. The average scalp maps of these IC clusters are shown in Figure 12. Figure A1-Figure A24 show the scalp maps, and Table A3-Table A10 summarize the Talairach coordinates of each dipole in the remaining clusters.

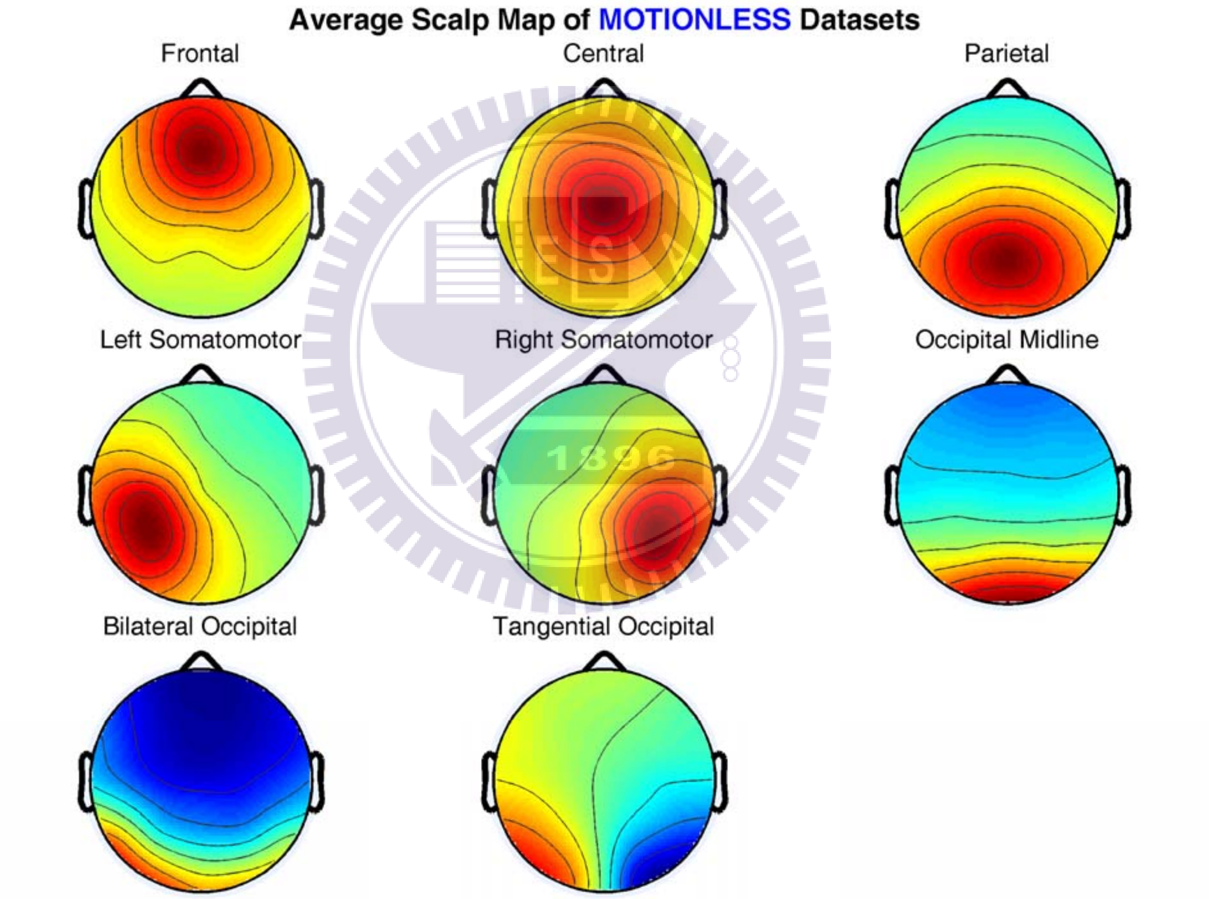

Figure 12: The average scalp maps of eight IC clusters in the motionless datasets.

4.1.3 Tonic Power Spectra

4.1.3.1 The Frontal Cluster

Figure 13 shows the results of the frontal cluster, including the average scalp map, dipole source locations, baseline power spectra, tonic power image, and trends of tonic power changes in four frequency bands. The power image and traces in Figure 13 D and E, respectively, show about 1~2 dB increase in the theta band when the mean RTs are longer than 1.88 sec, and such increase shifts to the lower frequencies when RTs further increase and become significant ($p < 10^{-10}$, two-sampled *t*-test, corrected) when RTs are longer than 6.67 sec.

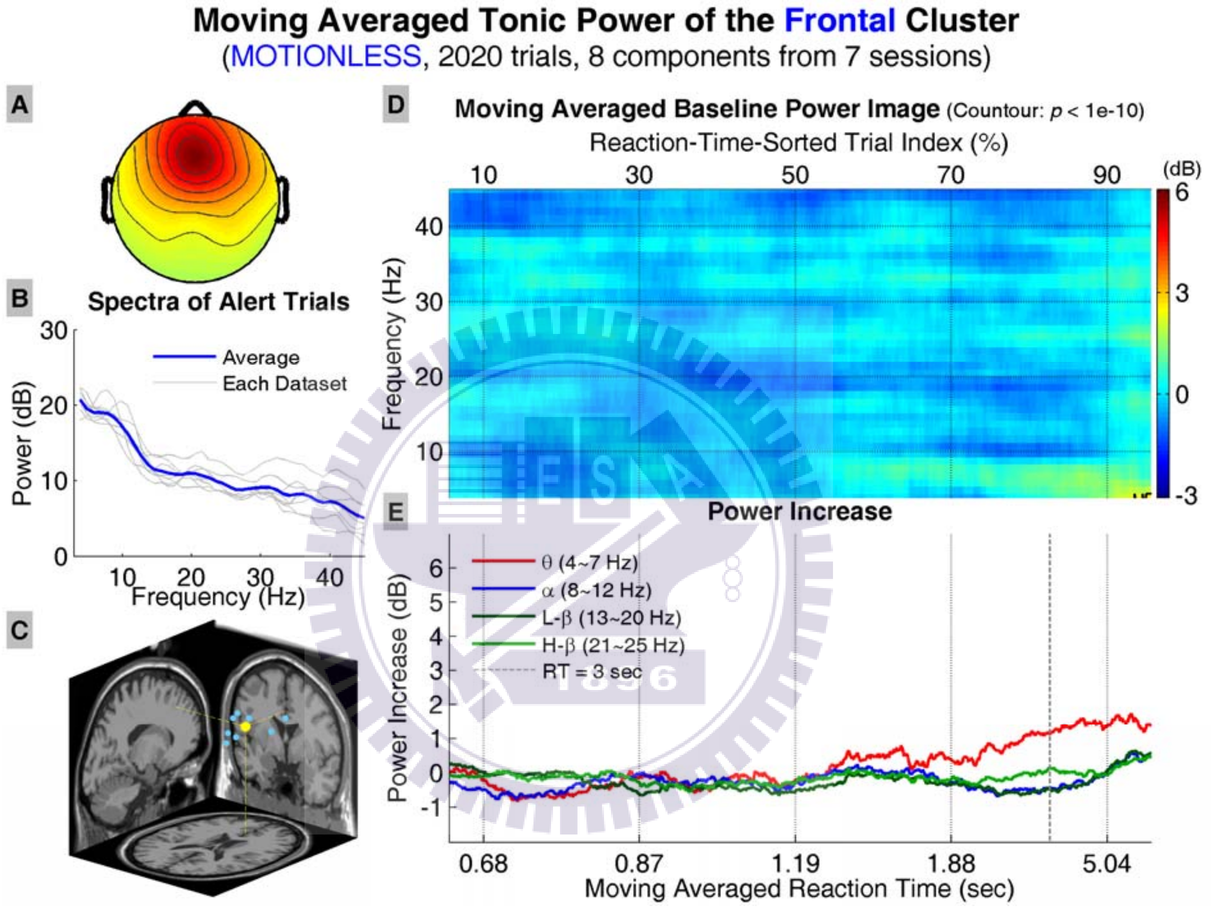

Figure 13: Results of the frontal cluster in the motionless datasets. A: the average scalp map of all IC in the cluster, B: mean power spectra of alert trials in each dataset and cluster average (blue trace), C: dipole locations (yellow dot: cluster average), D: the moving averaged power image (x-axis: RT-sorted index in percentage and the corresponding reaction time in seconds; y-axis: frequency in Hz; regions inside contour: $p < 10^{-10}$, two-tailed t-test, corrected for multiple comparison), and E: trends of mean tonic power in four frequency bands (extracted from D; x-axis: RT-sorted index and the corresponding reaction time in seconds; y-axis: power increase in dB).

4.1.3.2 The Central and Parietal Clusters

Figure 14 shows the results of the central cluster, including the average scalp map, dipole source locations, baseline power spectra, tonic power image, and trends of tonic power changes in four frequency bands. The power image and trends show significant increase in the low theta band when RTs are longer than 3 sec, and significant increase near 20 Hz when RTs are longer than 7.29 sec.

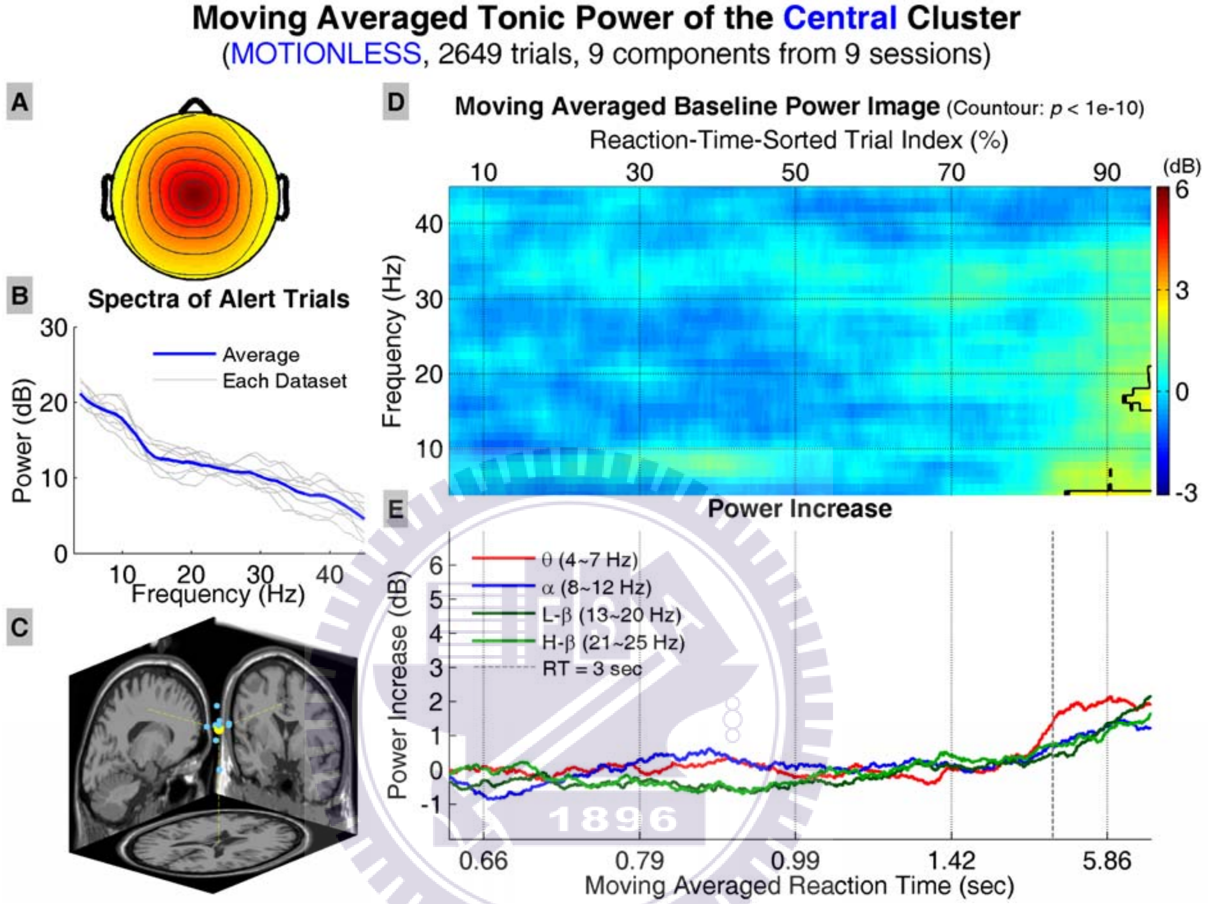

Figure 14: Results of the central cluster in the motionless datasets. All conventions follow Figure 13.

Figure 15 shows the results of the parietal cluster, including the average scalp map, dipole source locations, baseline power spectra, tonic power image, and trends of tonic power changes in four frequency bands. The power image and trends show the onset RTs of significant increase in the alpha and theta bands are around 2.27 sec and around 3 sec, respectively; in addition, such increase shifts to the lower frequencies when RTs further increase. Note that the power on the alpha band falls when RTs are longer than 3 sec, but theta band power continues to increase.

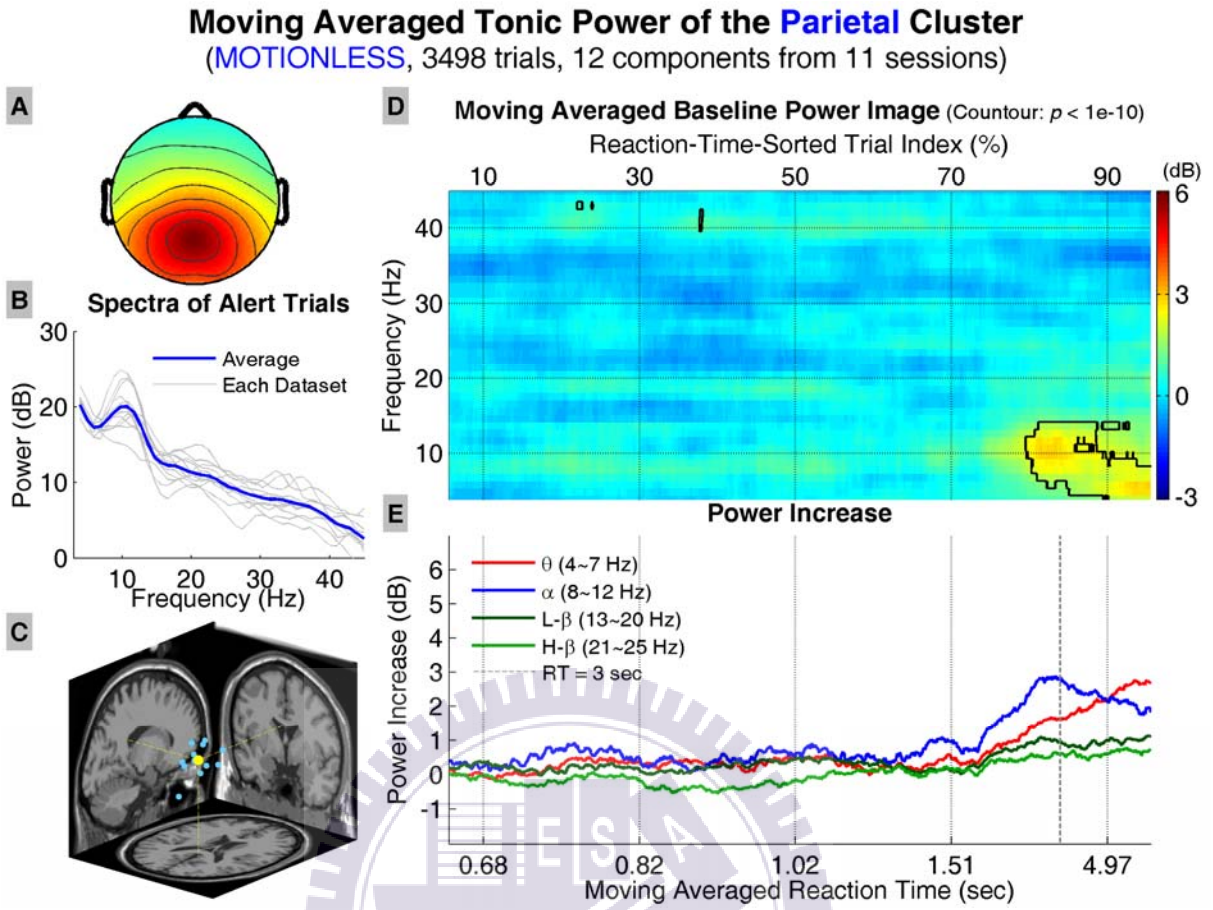

Figure 15: Results of the parietal cluster in the motionless datasets. All conventions follow Figure 13.

4.1.3.3 The Somatomotor Clusters

The results of the left and right somatomotor clusters, including the average scalp maps, dipole source locations, baseline power spectra, tonic power image, and trends of tonic power changes in four frequency bands, are shown in Figure 16 and Figure 17, respectively. The power images and trends show significant increase in the lower frequencies in the left (right) somatomotor cluster when RTs are longer than 2.17 (5.97) sec.

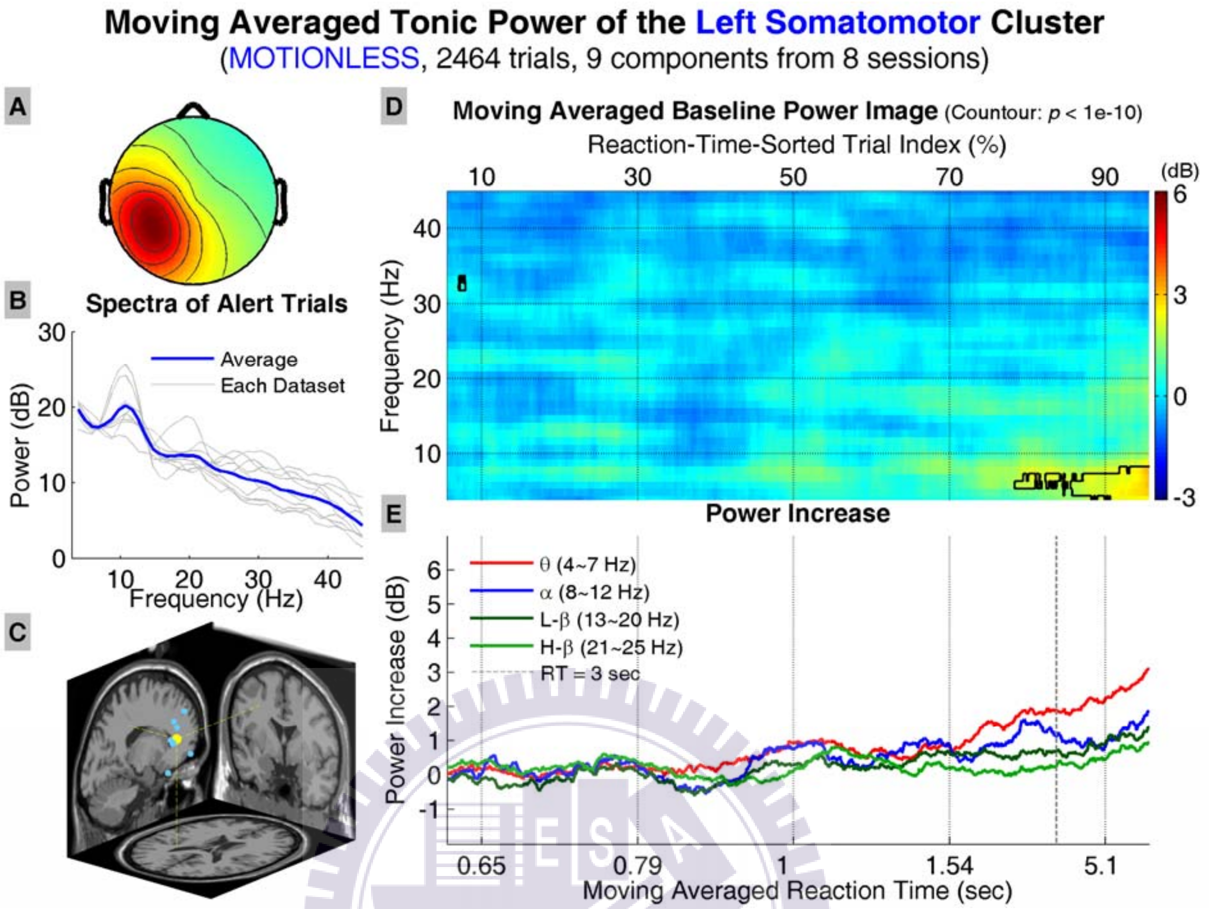

Figure 16: Results of the left somatomotor cluster in the motionless datasets. All conventions follow Figure 13.

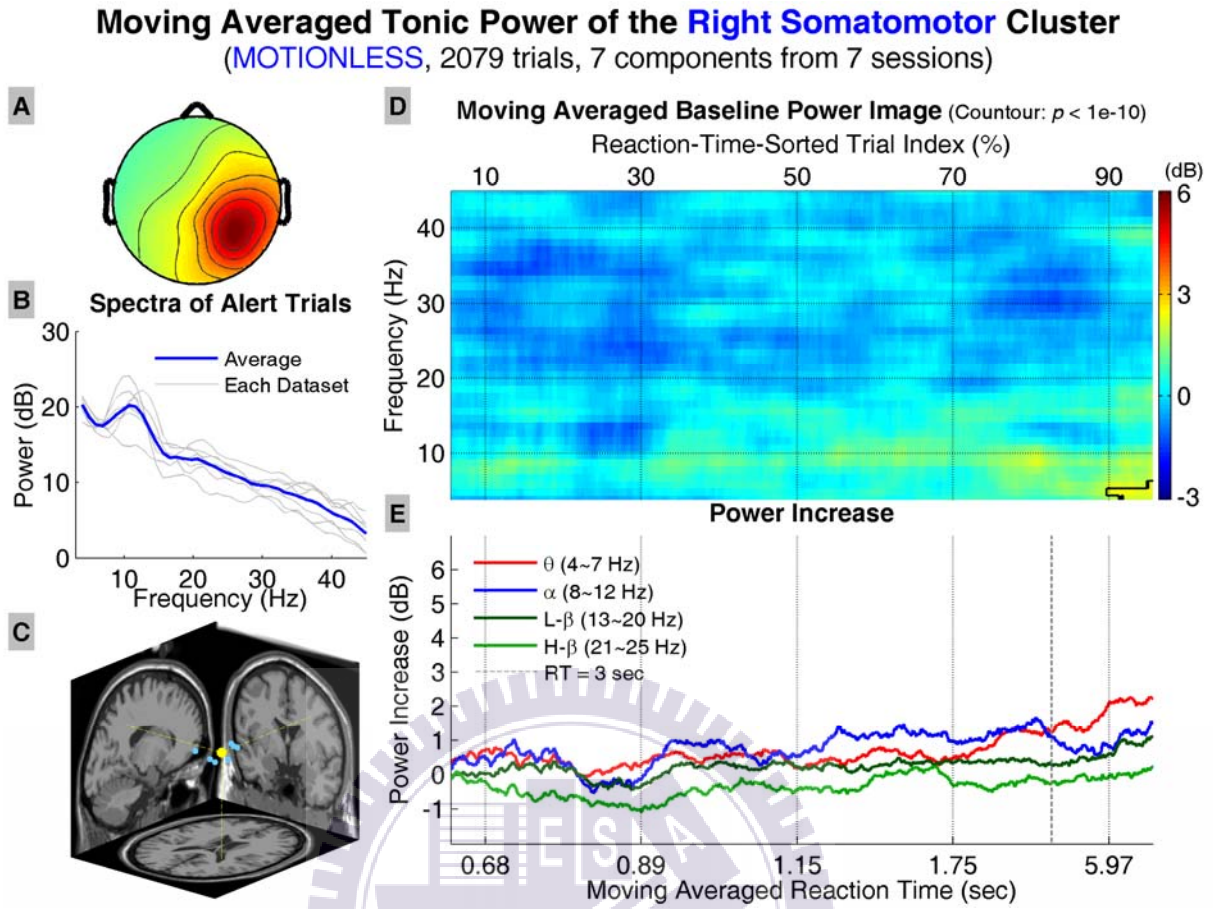

Figure 17: Results of the right somatomotor cluster in the motionless datasets. All conventions follow Figure 13.

4.1.3.4 The Occipital Clusters

Figure 18 shows the results of the occipital midline cluster, including the average scalp map, dipole source locations, baseline power spectra, tonic power image, and trends of tonic power changes in four frequency bands. The power image and trends start to show increase in the lower frequency bands when RTs are longer than ~1.27 sec. The power increase becomes significant when RTs are longer than ~3 sec, and shifts to the lower frequencies when RTs become even longer. The trend in alpha band power starts to decrease at RTs lower than those where the descending trend occurs in the theta band power.

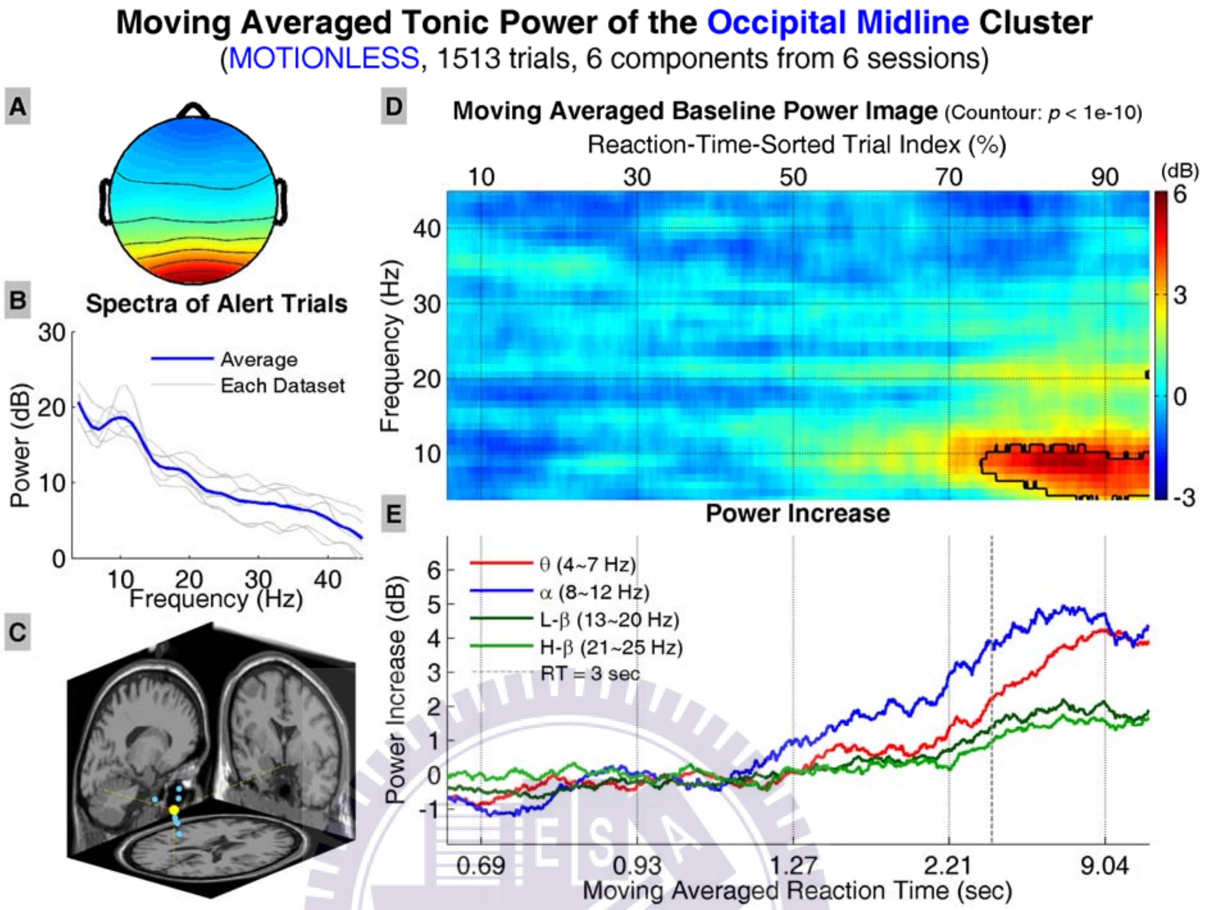

Figure 18: Results of the occipital midline cluster in the motionless datasets. All conventions follow Figure 13.

Figure 19 shows the results of the bilateral occipital cluster, including the average scalp map, dipole source locations, baseline power spectra, tonic power image, and trends of tonic power changes in four frequency bands. The power image and trends start to show increase in the lower frequency bands when RTs are longer than ~1 sec. The power increase becomes significant when RTs are longer than ~1.3 sec and shifts to the lower frequencies when RTs become even longer. The trends in alpha band and low beta band power start to decrease when RTs are over ~3 sec; however, the trend in theta band power continues to increase as RTs further increase.

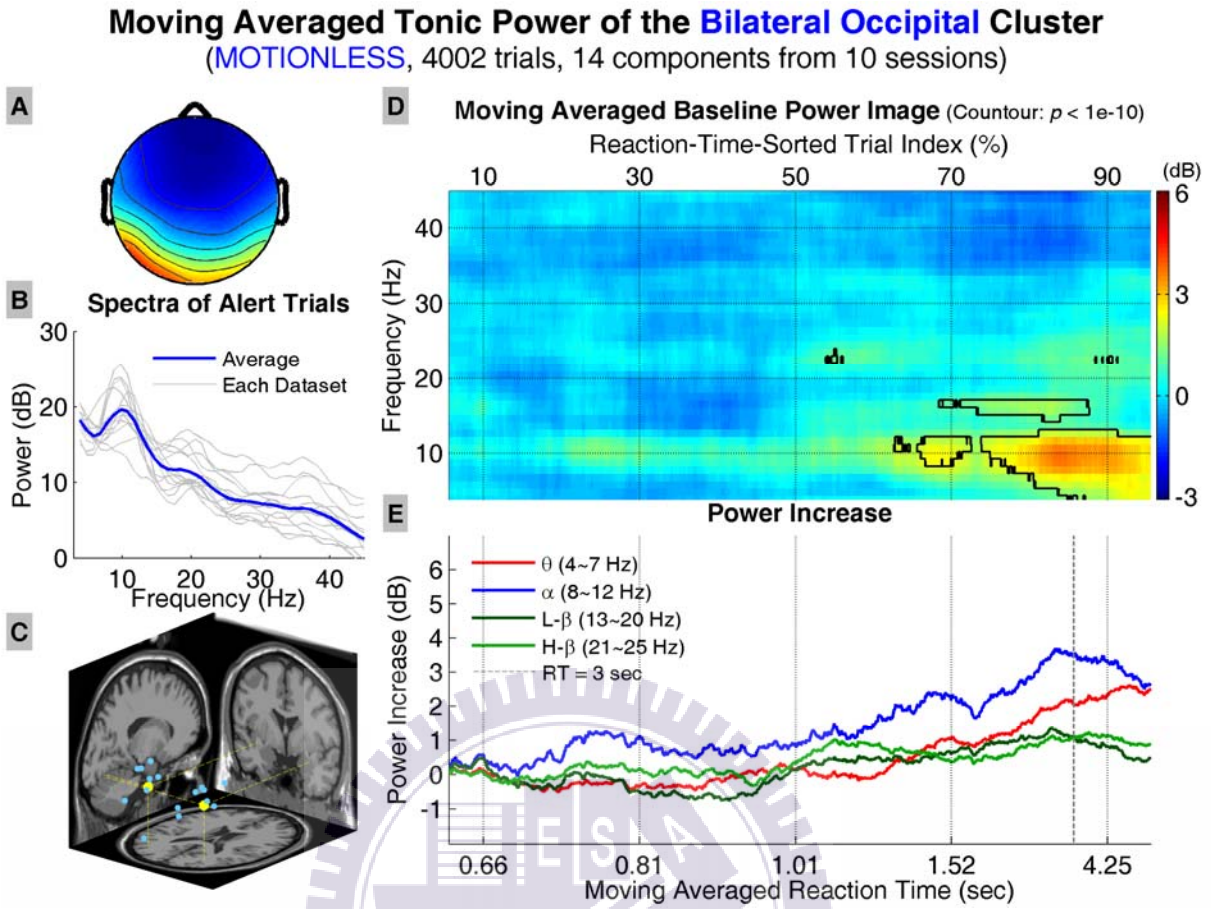

Figure 19: Results of the bilateral occipital cluster in the motionless datasets. All conventions follow Figure 13.

Figure 20 shows the results of the tangential occipital cluster, including the average scalp map, dipole source locations, baseline power spectra, tonic power image, and trends of tonic power changes in four frequency bands. The power image and trends start to show increase in the lower frequency bands when RTs are longer than ~1.15 sec. The power increase becomes significant when RTs are longer than ~1.8 sec and shifts to the lower frequencies when RTs become even longer. The trends in alpha band and low/high beta band power start to decrease when RTs are over ~3 sec; however, the trend in theta band power continues to increase monotonically as RTs further increase.

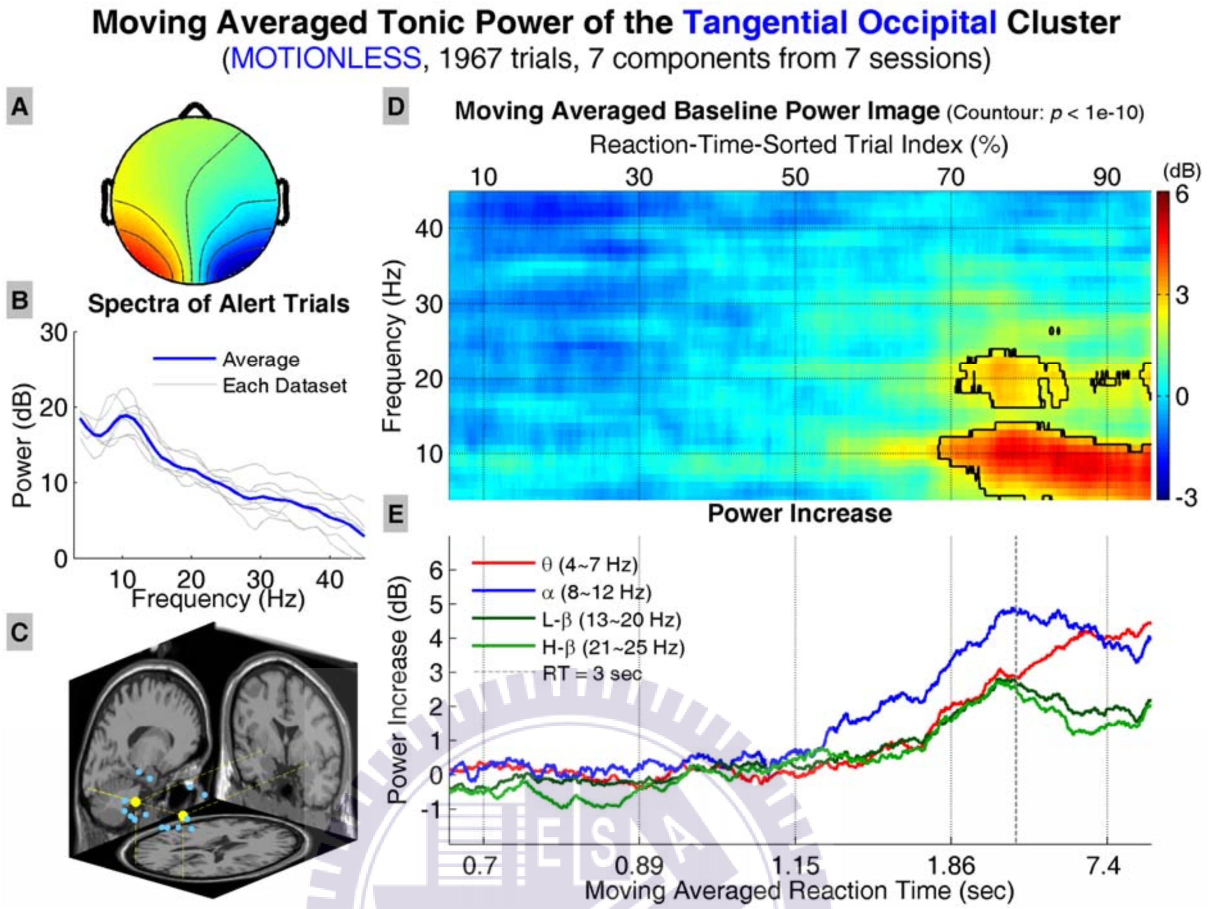

Figure 20: Results of the tangential occipital cluster in the motionless datasets. All conventions follow Figure 13.

4.2 Motion Datasets

4.2.1 Behavioral Data

Table 2 shows the distribution of behavioral data of individual subjects in the “motion” condition. The shaded rows show the numbers of trials remained after EEG and behavioral artifact removal. Subjects are sorted in descending order by their drowsiness levels. In total, 52.84% of original trials in all subjects remained due to severe artifacts in the driving experiments. The car drifted to the left (right) in 51.7% (49.3%) of all the remained trials.

TABLE 2: BEHAVIORAL DATA OF MOTION DATASETS

	Trials	Data Length (sec)*	Trials Re-mained (%)**	Max. RT (sec)	Min. RT (sec)	Avg. RT (sec)	SD of RT (sec)	Med. of RT (sec)	Trials w. RT > 3 sec (%)	Dev. to Left (%)
s44_070209	662	5815.36	--	18.79	0.15	1.54	2.09	0.80	11.48	53.78
	409	--	61.78	14.74	0.45	1.74	2.25	0.84	**14.18**	52.57
s05_061019	683	6315.52	--	11.3	0.02	1.29	1.54	0.87	6.88	53.44
	319	--	46.71	11.3	0.54	1.58	1.96	0.85	**10.34**	53.61
s35_070115	540	6515.16	--	383.60	0.02	3.05	19.28	0.89	9.44	52.41
	301	--	55.74	27.40	0.33	1.56	2.87	0.80	**6.98**	55.48
s36_061122	685	6535.12	--	22.52	0.02	1.53	1.89	1.14	4.67	51.39
	330	--	48.18	22.52	0.45	1.79	2.49	1.13	**7.27**	47.58
s40_070131	632	6562.20	--	27.14	0.02	1.51	2.14	1.07	5.85	49.05
	316	--	50.00	27.14	0.38	1.59	2.54	1.07	**5.06**	46.52
s43_070202	711	6533.24	--	12.74	0.10	1.01	1.21	0.70	2.25	51.62
	315	--	44.30	12.74	0.43	1.11	1.66	0.69	**4.76**	54.60
s31_061020	640	7061.04	--	10.81	0.02	1.36	0.85	1.25	2.50	52.34
	416	--	65.00	8.39	0.52	1.39	0.68	1.29	**2.16**	51.68
All subjects	4553	--	--	383.6	0.02	1.57	6.84	0.97	6.04	52.01
	2406	--	52.84	27.40	0.33	1.54	2.14	0.99	**7.32**	51.70

Note: shaded areas: distribution of the trials remained after artifacts removal. *: original datasets. **: datasets after artifacts removal.

Figure 21 shows the cumulative distribution of sorted reaction time across subjects in the “motion” datasets. The x- and y- axes are reaction time (in log scale) and percentage of RT-sorted index, respectively, and the vertical dashed line indicates 3-sec RT. The curve shows an approximate bi-linear distribution of RTs (when the x-axis is plotted in linear scale). About 10% of all remained trials have RTs longer than 3 sec, which suggest the subjects were not very drowsy in these trials.

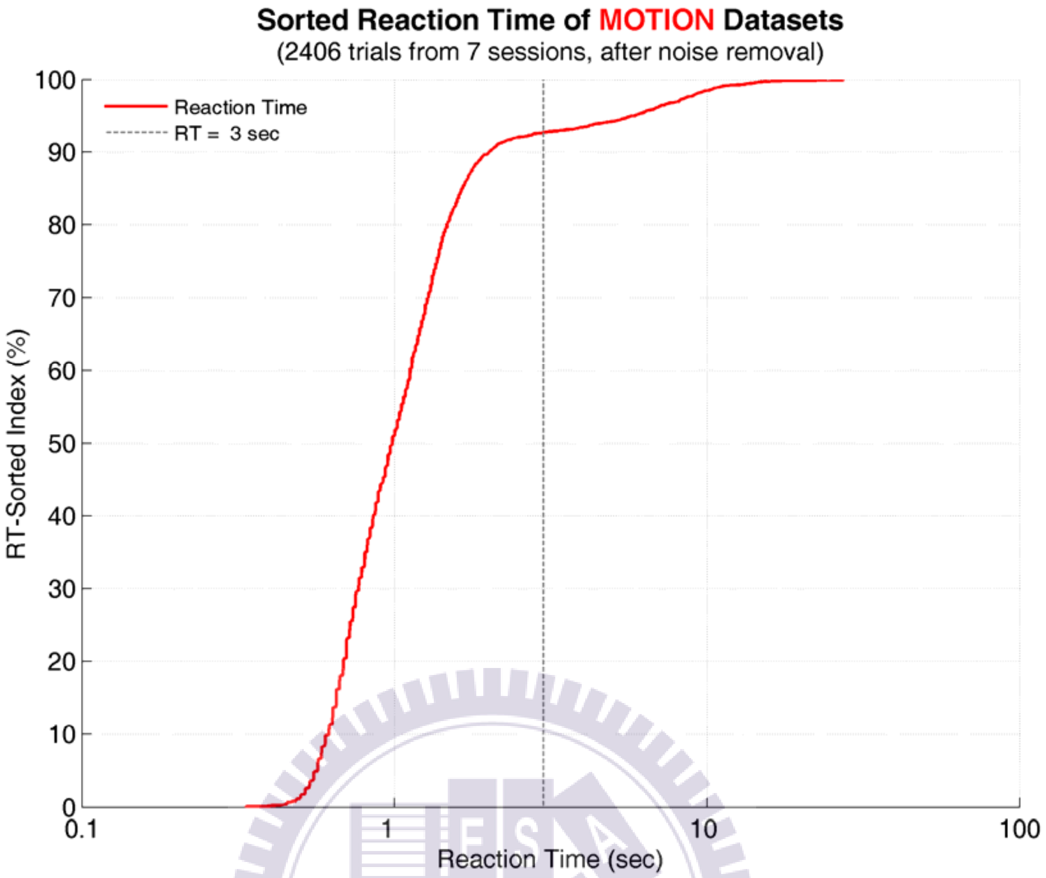

Figure 21: Cumulative distribution curve of sorted reaction times in the motion datasets.

4.2.2 Clustered Scalp Maps and Dipole Locations

Eight clusters of independent components were identified based on their scalp maps from the results of ICA decomposition. The average scalp maps of these IC clusters are shown in Figure 22. Figure A25-Figure A48 show the scalp maps, and Table A11-Table A18 summarize the Talairach coordinates of each dipole in the remaining clusters.

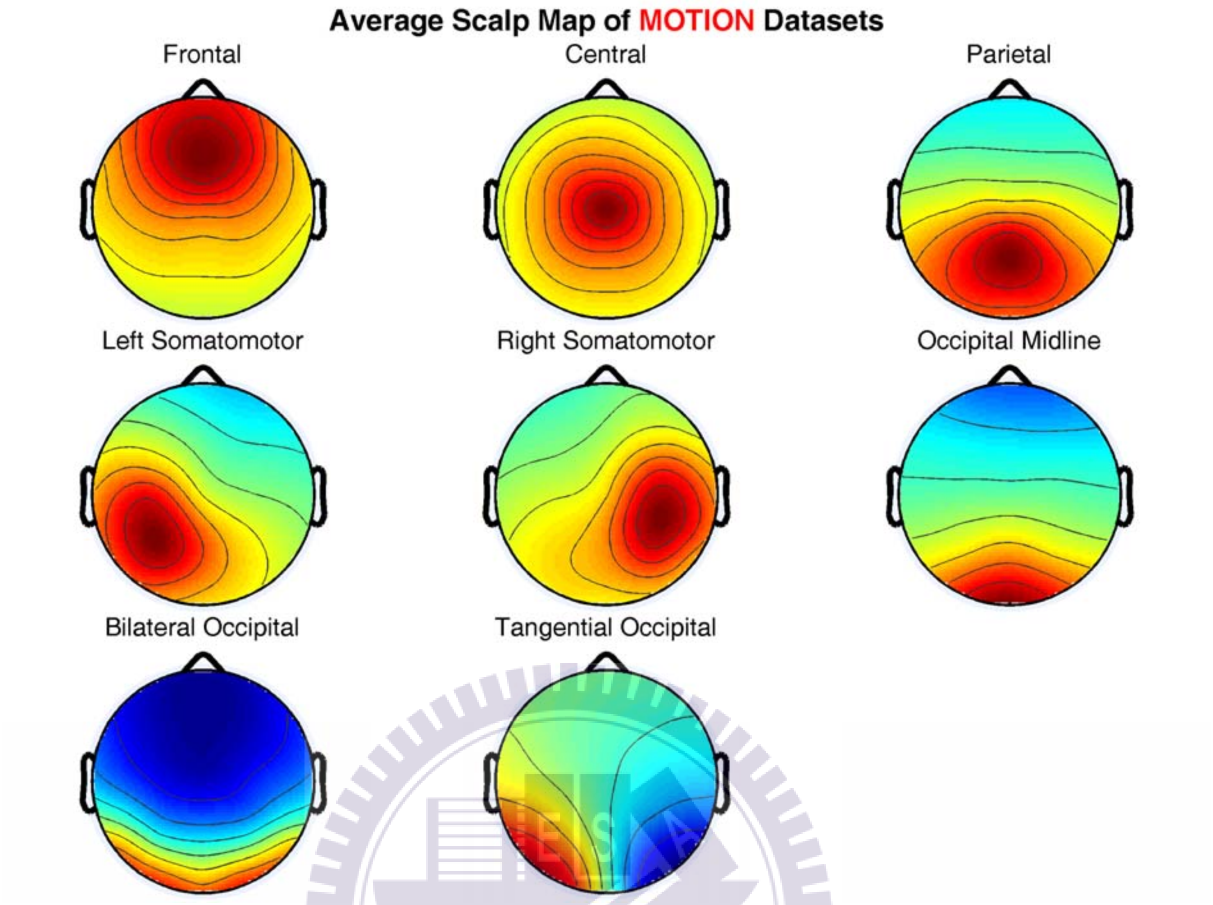

Figure 22: The average scalp maps of eight IC clusters in the motion datasets.

4.2.3 Tonic Power Spectra

4.2.3.1 The Frontal Cluster

Figure 23 shows the results of the frontal cluster, including the average scalp map, dipole source locations, baseline power spectra, tonic power image, and trends of tonic power changes in four frequency bands. The power image and trends in Figure 23 D and E, respectively, show increase in the theta band when the mean RTs are longer than 1.31 sec, and such increase shifts to the lower frequencies when RTs further increase and become significant ($p < 10^{-10}$, corrected) when RTs are longer than 2.38 sec.

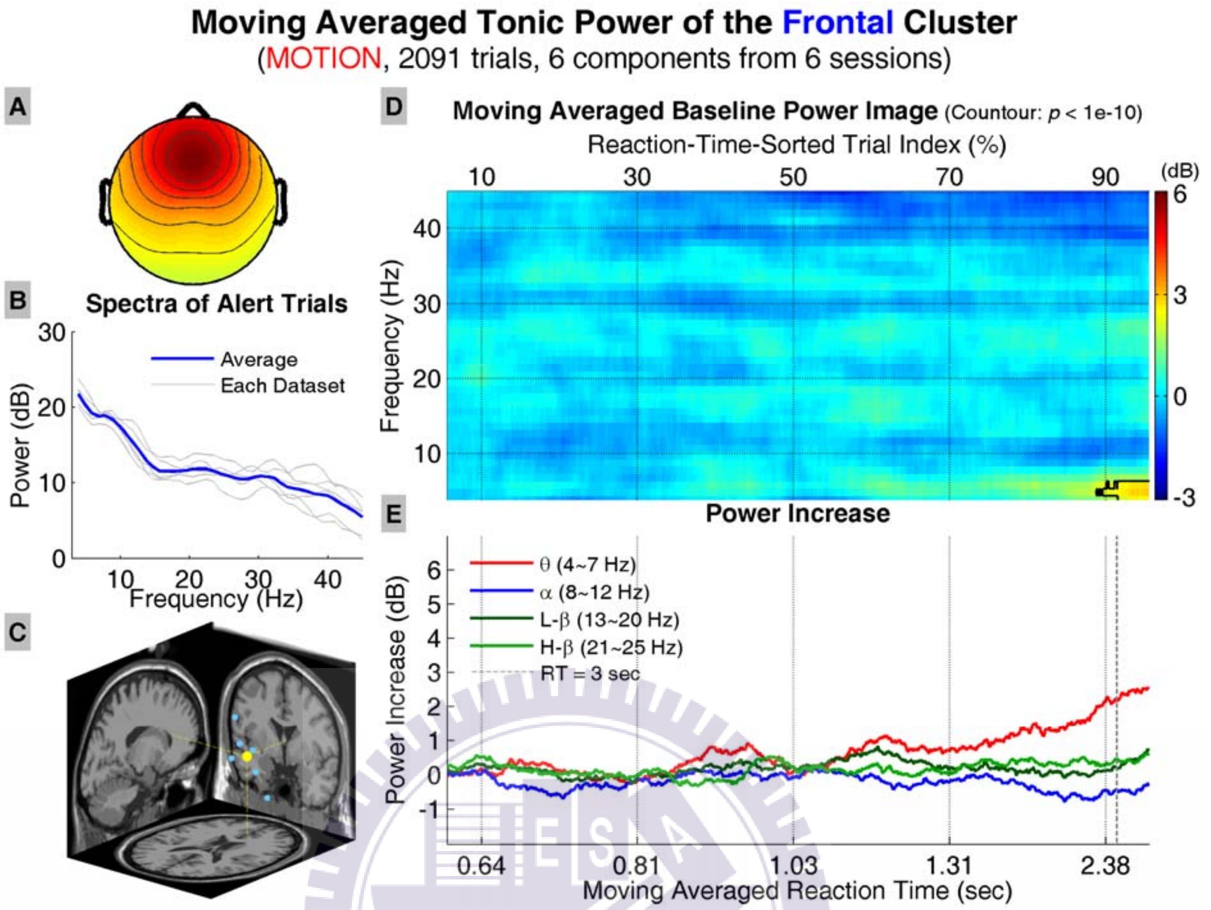

Figure 23: Results of the frontal cluster in the motion datasets. All conventions follow Figure 13.

4.2.3.2 The Central and Parietal Clusters

Figure 24 shows the results of the central cluster, including the average scalp map, dipole source locations, baseline power spectra, tonic power image, and trends of tonic power changes in four frequency bands. The power image and trends show significant increase in the low theta band when RTs are longer than ~2.5 sec, and significant increase near 20 Hz when RTs reach the maximum value.

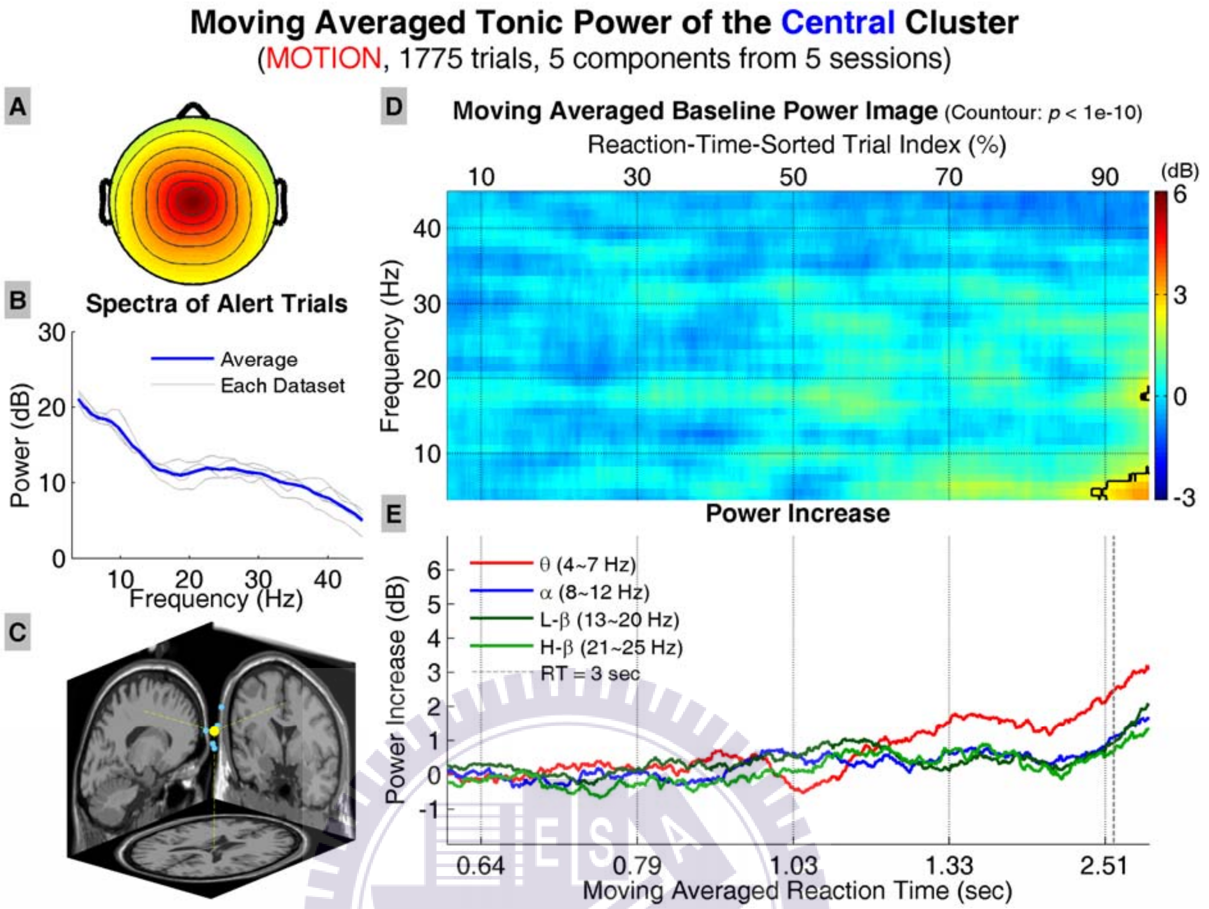

Figure 24: Results of the central cluster in the motion datasets. All conventions follow Figure 13.

Figure 25 shows the results of the parietal cluster, including the average scalp map, dipole source locations, baseline power spectra, tonic power image, and trends of tonic power changes in four frequency bands. The power image and trends show increase in the alpha and beta bands when RTs increase moderately, and the increase shifts to the lower frequencies when RTs further increase. However, the increase in the entire power spectra does not reach the significance level.

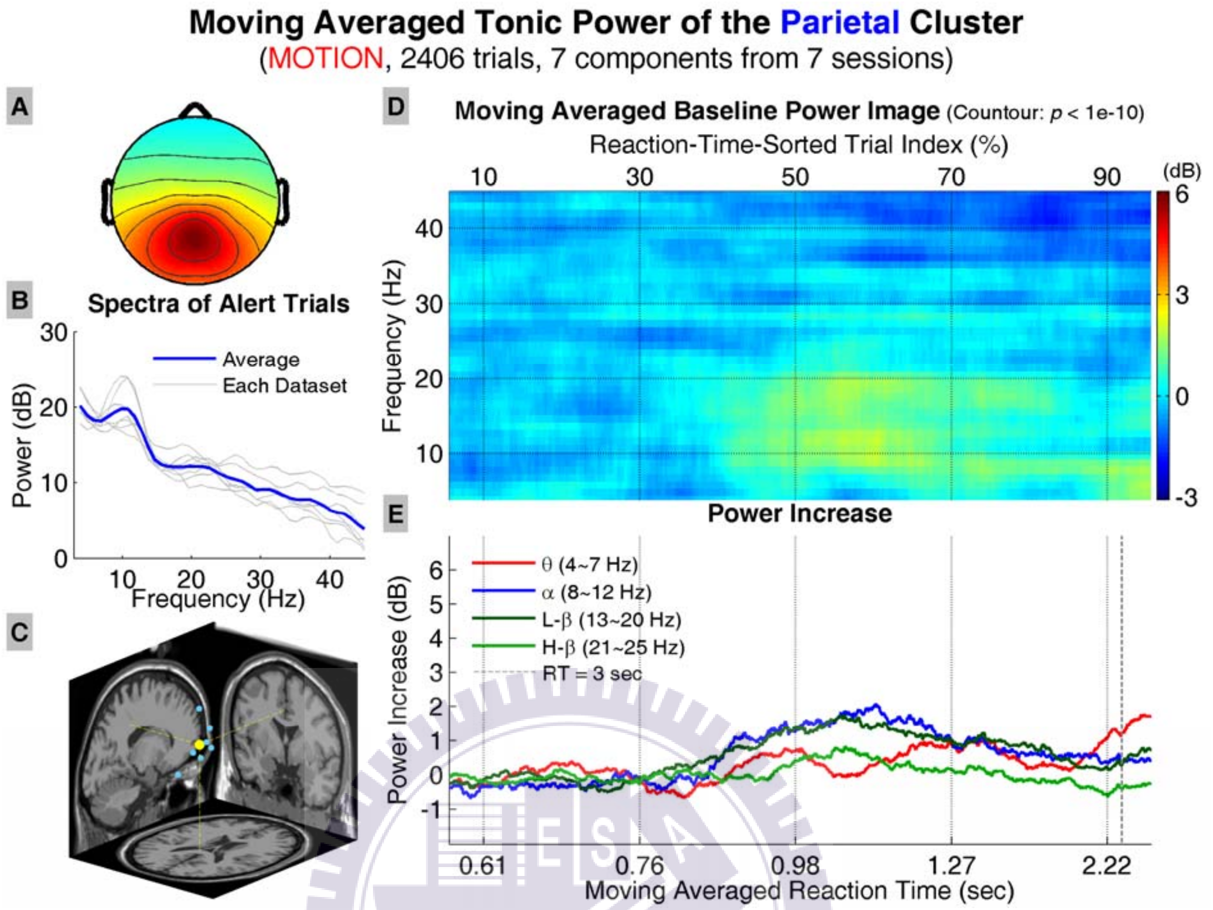

Figure 25: Results of the parietal cluster in the motion datasets. All conventions follow Figure 13.

4.2.3.3 The Somatomotor Clusters

The results of the left and right somatomotor clusters, including the average scalp maps, dipole source locations, baseline power spectra, tonic power image, and trends of tonic power changes in four frequency bands, are shown in Figure 26 and Figure 27, respectively. Both somatomotor clusters show no significant changes when RTs increase.

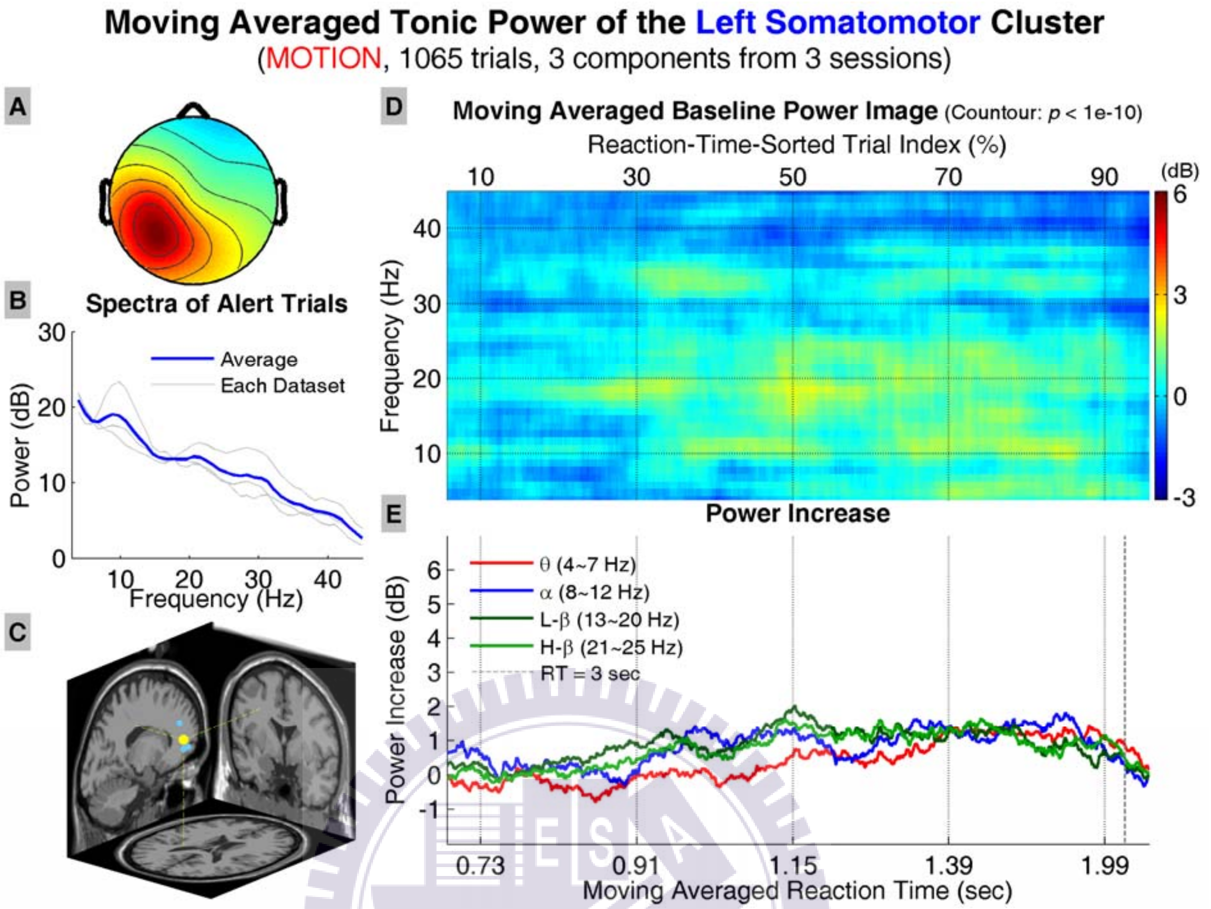

Figure 26: Results of the left somatomotor cluster in the motion datasets. All conventions follow Figure 13.

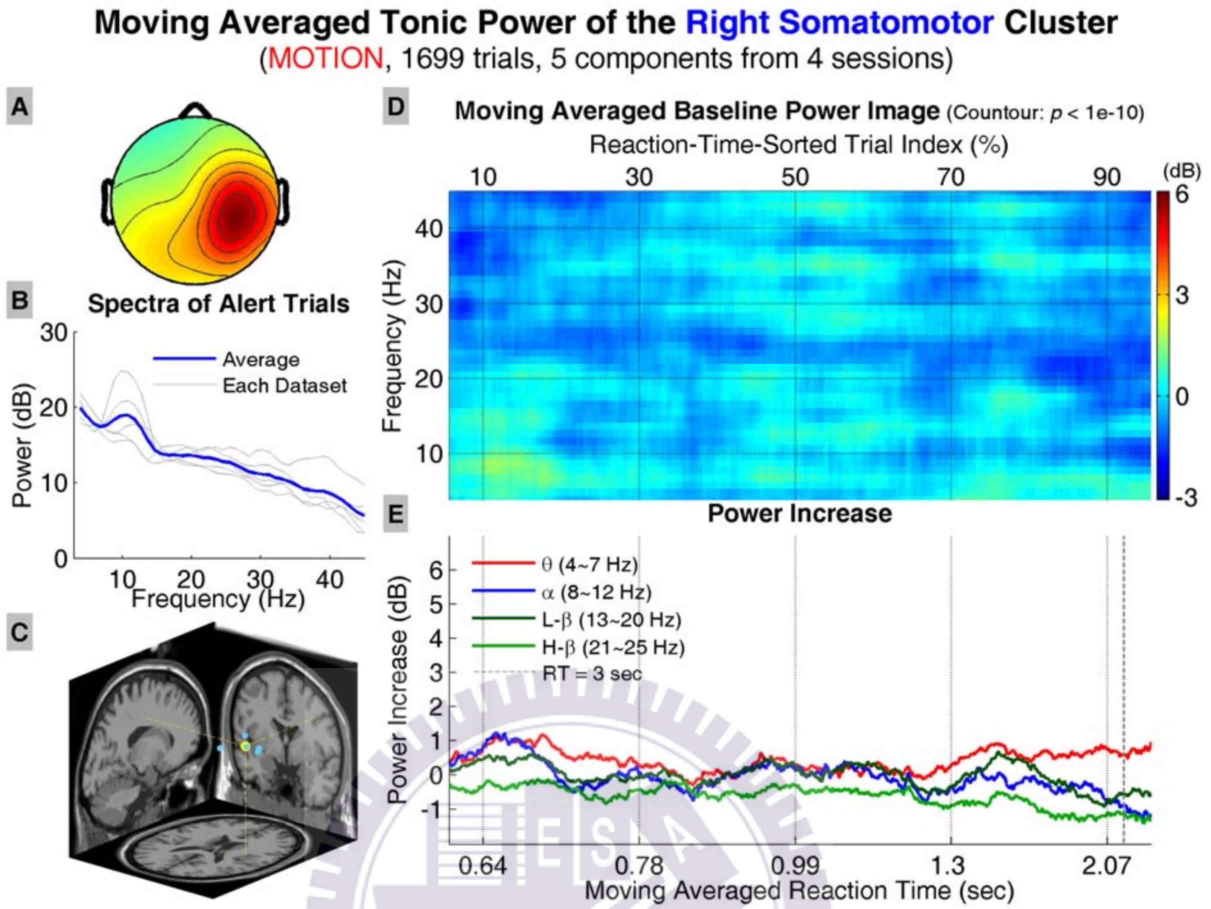

Figure 27: Results of the right somatomotor cluster in the motion datasets. All conventions follow Figure 13.

4.2.3.4 The Occipital Clusters

Figure 28 shows the results of the occipital midline cluster, including the average scalp map, dipole source locations, baseline power spectra, tonic power image, and trends of tonic power changes in four frequency bands. The power image and trends start to show increase in the lower frequency bands when RTs are longer than ~0.9 sec. The power increase in alpha (theta) band becomes significant when RTs are longer than ~1.6 (~2.4) sec, and the increase shifts to the lower frequencies when RTs become even longer. The increase in power in the alpha band is larger than that in the other bands, and it reaches a plateau when RTs are longer than ~1.23 sec; however, theta band power continues to increase monotonically with long RTs.

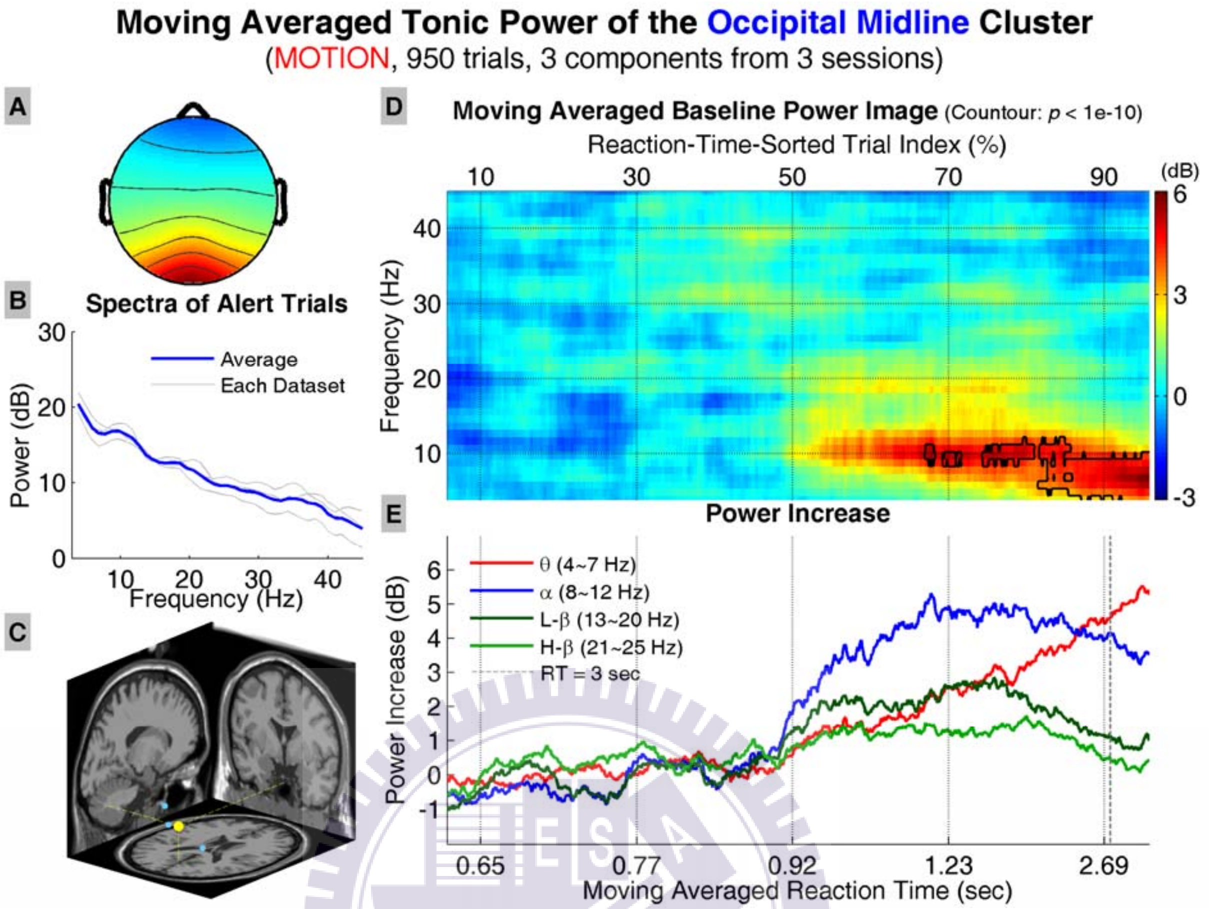

Figure 28: Results of the occipital midline cluster in the motion datasets. All conventions follow Figure 13.

Figure 29 shows the results of the bilateral occipital cluster, including the average scalp map, dipole source locations, baseline power spectra, tonic power image, and trends of tonic power changes in four frequency bands. The power image and trends start to show significant increase in the lower frequency bands (alpha and theta) when RTs are longer than ~0.9 sec, and shifts to the lower frequencies when RTs become even longer. The increase in alpha band power is higher than that in the other frequency bands. The trends in alpha band and beta band power start to decrease when RTs are over ~1.1 sec; however, the trend in theta band power continues to increase as RTs further increase.

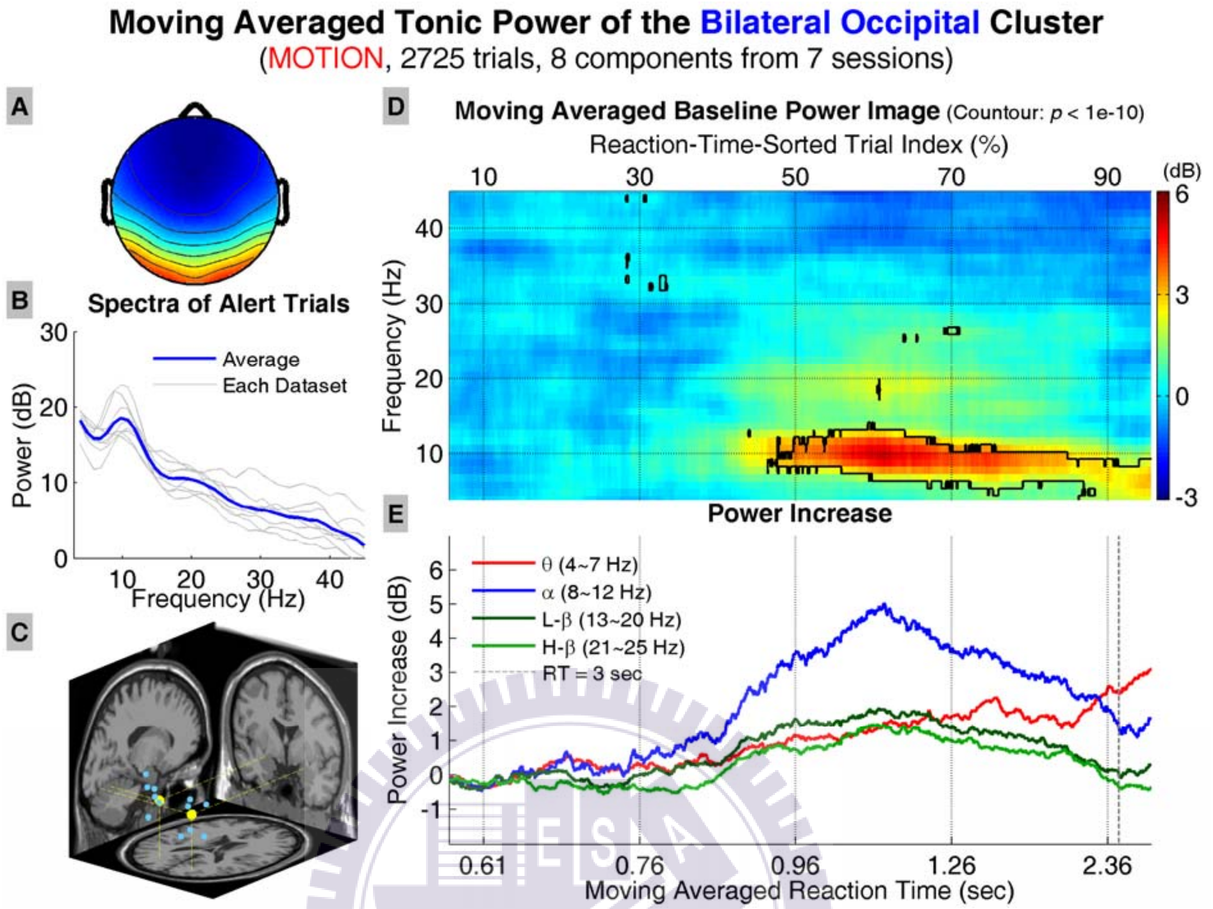

Figure 29: Results of the bilateral occipital cluster in the motion datasets. All conventions follow Figure 13.

Figure 30 shows the results of the tangential occipital cluster, including the average scalp map, dipole source locations, baseline power spectra, tonic power image, and trends of tonic power changes in four frequency bands. The power image and trends show increase in the alpha and beta bands when RTs increase, and the power increase in alpha (beta) band becomes significant when RTs are longer than 1.08 (0.99) sec, respectively. The trend in alpha (beta) band power reverses to the downside when RTs are longer than 1.23 (1.08) sec, and theta band power increases abruptly when RTs are longer than 1.61 sec.

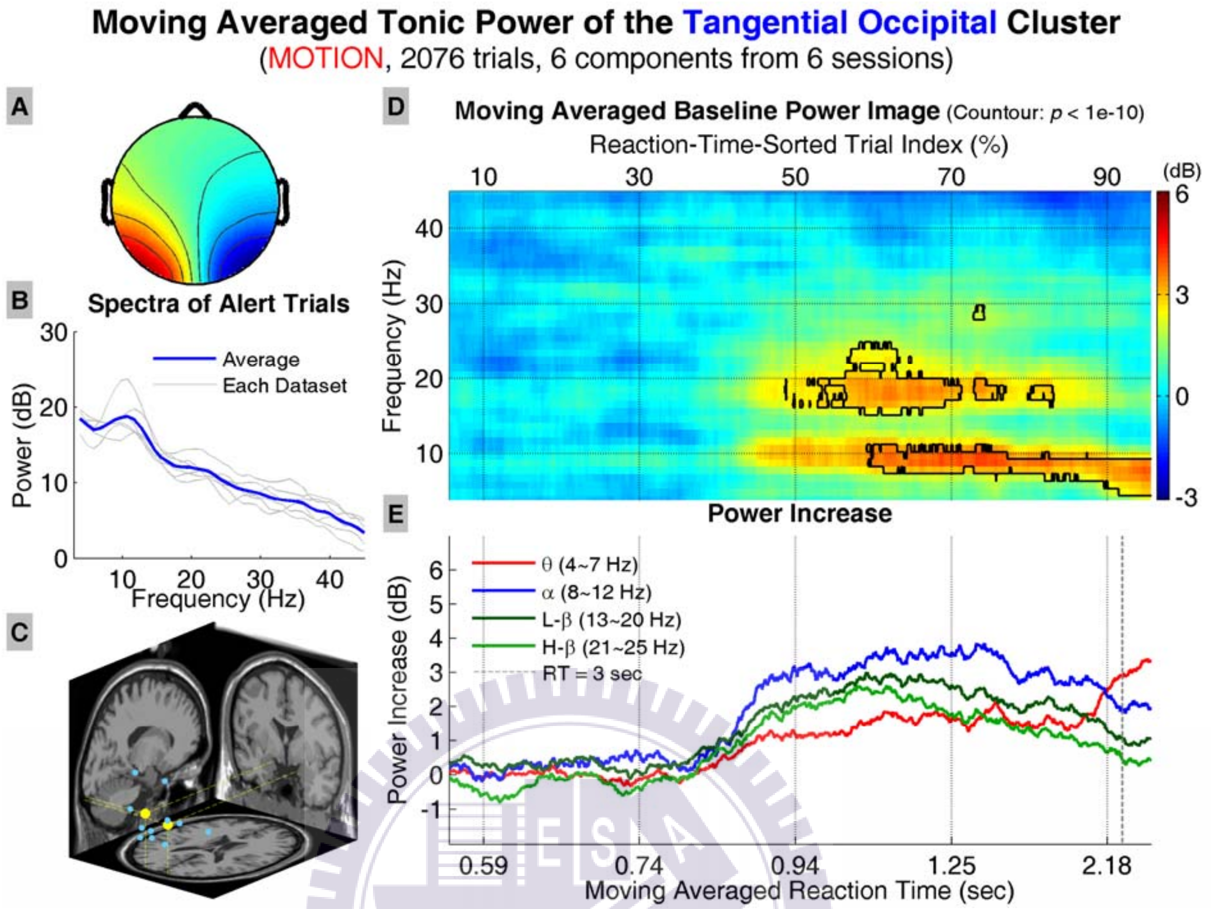

Figure 30: Results of the tangential occipital cluster in the motion datasets. All conventions follow Figure 13.

4.3 Comparison Between Motionless and Motion Datasets

In real-life driving, the driver receives kinesthetic stimuli in addition to visual and auditory stimuli on the road. In order to investigate the effect of kinesthetic stimuli on the EEG data especially during drowsy driving, seven subjects who participated in both motion and motionless sessions were selected for comparison, and the behavioral data and trends in EEG power spectra were compared between motion and motionless conditions. Subjects s01, s32, s41, and s42 did not participate in motion sessions, so their EEG data in the motionless datasets were not included in the comparison.

4.3.1 Behavioral data

Figure 31 shows the cumulative distributions of sorted reaction times across subjects in the “motion” (red trace) and “motionless” (blue trace) datasets, respectively. The x- and y- axes are reaction time (in log scale) and percentage of RT-sorted index, respectively, and the vertical dashed line indicates 3-sec RT. Both curves show approximate bi-linear distributions of RTs (when the x-axis is plotted in linear scale). The traces show that over 90% of trials have RTs less than 3 sec in the motion datasets, and only over 80% of trial RTs are below 3 sec in the motionless datasets. In addition, in the motion datasets, the shortest 1/3 (802 trials, RTs = 0.38~0.82 sec, mean = 0.66 ± 0.09 sec, median = 0.67 sec) and longest 1/3 (802 trials, RTs = 1.22~27.40 sec, mean = 2.97 ± 3.25 sec, median = 1.59 sec) RTs are longer than corresponding portions of RTs in the motionless datasets (shortest 1/3: 693 trials, RTs = 0.38~0.82 sec, mean = 0.71 ± 0.07 sec, median = 0.72 sec; longest 1/3: 693 trials, RTs = 1.27~56.98 sec, mean = 6.15 ± 7.28 sec, median = 3.36 sec). The curves in both conditions are statistically different ($p < 10^{-10}$, two-sample *t*-test); however, the middle 1/3 of RTs in both conditions are not significant (motionless datasets: 694 trials, RTs = 0.82~1.27 sec, mean = 1.00 ± 0.12 sec, median = 0.97 sec; motion datasets: 802 trials, RTs = 0.80~1.22 sec, mean = 0.99 ± 0.13 sec, median = 0.99 sec; $p = 0.41$).

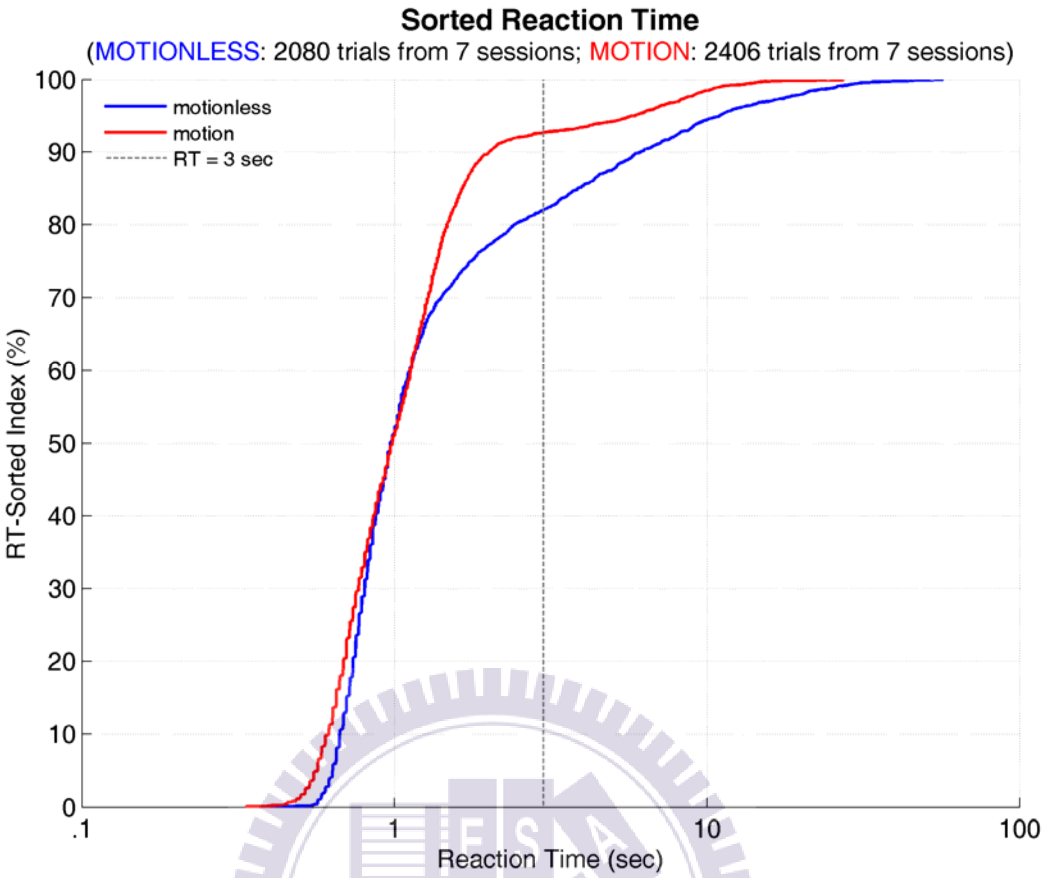

Figure 31: Cumulative distributions of sorted reaction times in motionless (blue trace) and motion (red trace) conditions.

4.3.2 Tonic Power Spectra

4.3.2.1 The Frontal Clusters

Figure 32 shows the results of the frontal clusters in motionless and motion conditions, including the average scalp maps, tonic power images, and trends of tonic power changes in four frequency bands. The power images in Figure 32 C show the onset of significant increase in the theta band power at shorter RTs in the motion condition than those in the motionless condition. In addition, the trends in Figure 32 D show monotonic power increase in theta band when RTs increase in the motion condition, and theta band power in the motionless condition initially increases with RTs and starts to decline above 3-sec RT. The alpha band power is lower in the motion condition than that in the motionless condition when RTs are longer than 1 sec, and the overall high-beta band power is lower in the motionless condition than that in the motion condition. These results suggest that kinesthetic stimuli have influences on the alpha and band power in the frontal cluster.

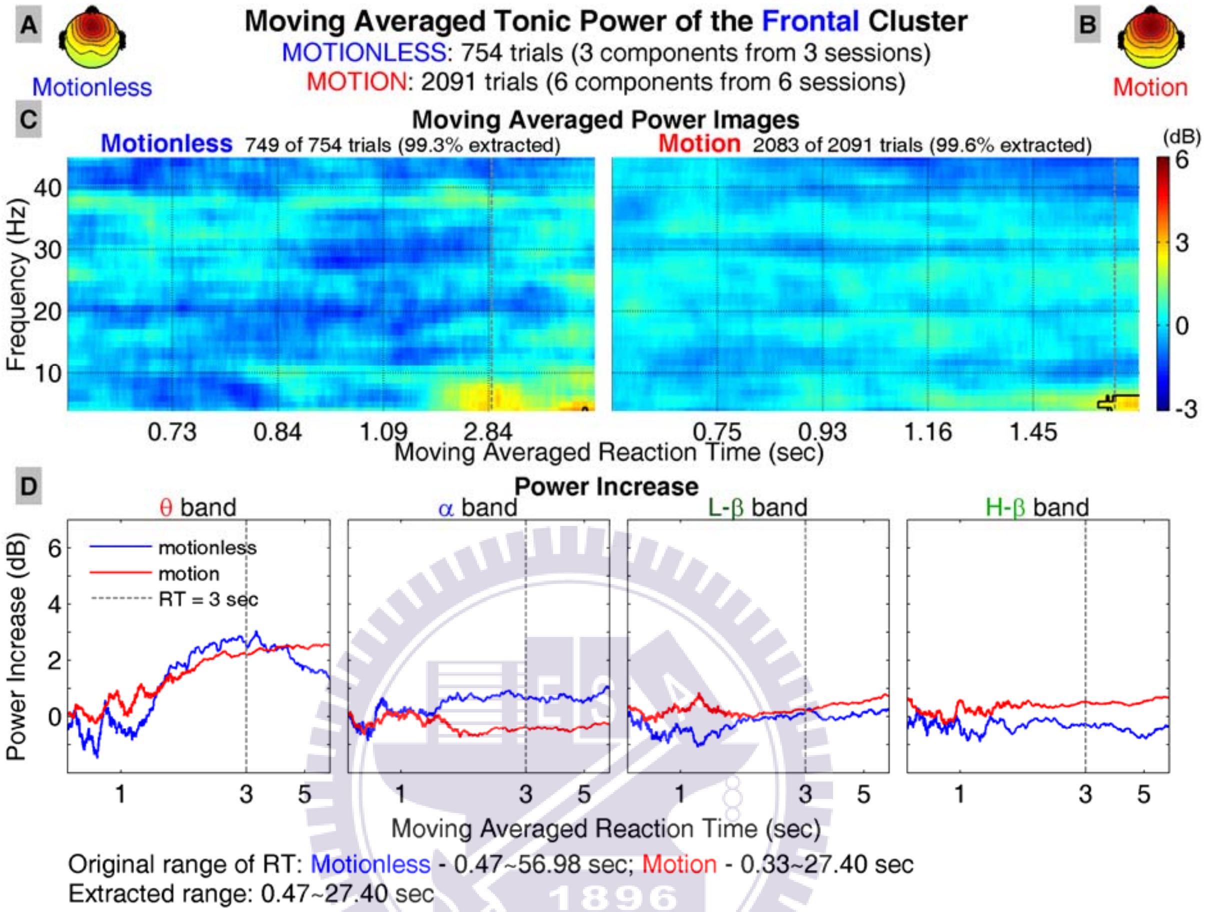

Figure 32: Comparison of the trends of tonic power spectra between motionless and motion conditions of the frontal cluster. A and B: average scalp maps in the motionless and motion datasets, respectively, C: moving averaged power images (left panel: the motionless datasets, right panel: the motion datasets; x-axis: reaction time, y-axis: frequency; regions inside contour: $p < 10^{-10}$, two-sample t-test, corrected), and D: trends of power in four frequency bands (extracted from C; blue and red traces: motionless and motion conditions, respectively; vertical dashed line: RT = 3 sec).

4.3.2.2 The Central Clusters

Figure 33 shows the results of the central clusters in motionless and motion conditions, including the average scalp maps, tonic power images, and trends of tonic power changes in four frequency bands. The power images in Figure 33 C show the onset of significant increase in the theta band power at shorter RTs in the motion condition than those in the motionless condition. The trends in Figure 33 D show higher increase in the theta band power in the motion condition than that in the motionless condition when RTs are longer than ~ 1 sec; however, the trends in alpha and beta band power are virtually the same in both motion and motionless conditions. These comparisons suggest that kinesthetic stimuli only influence the theta band power in the central cluster.

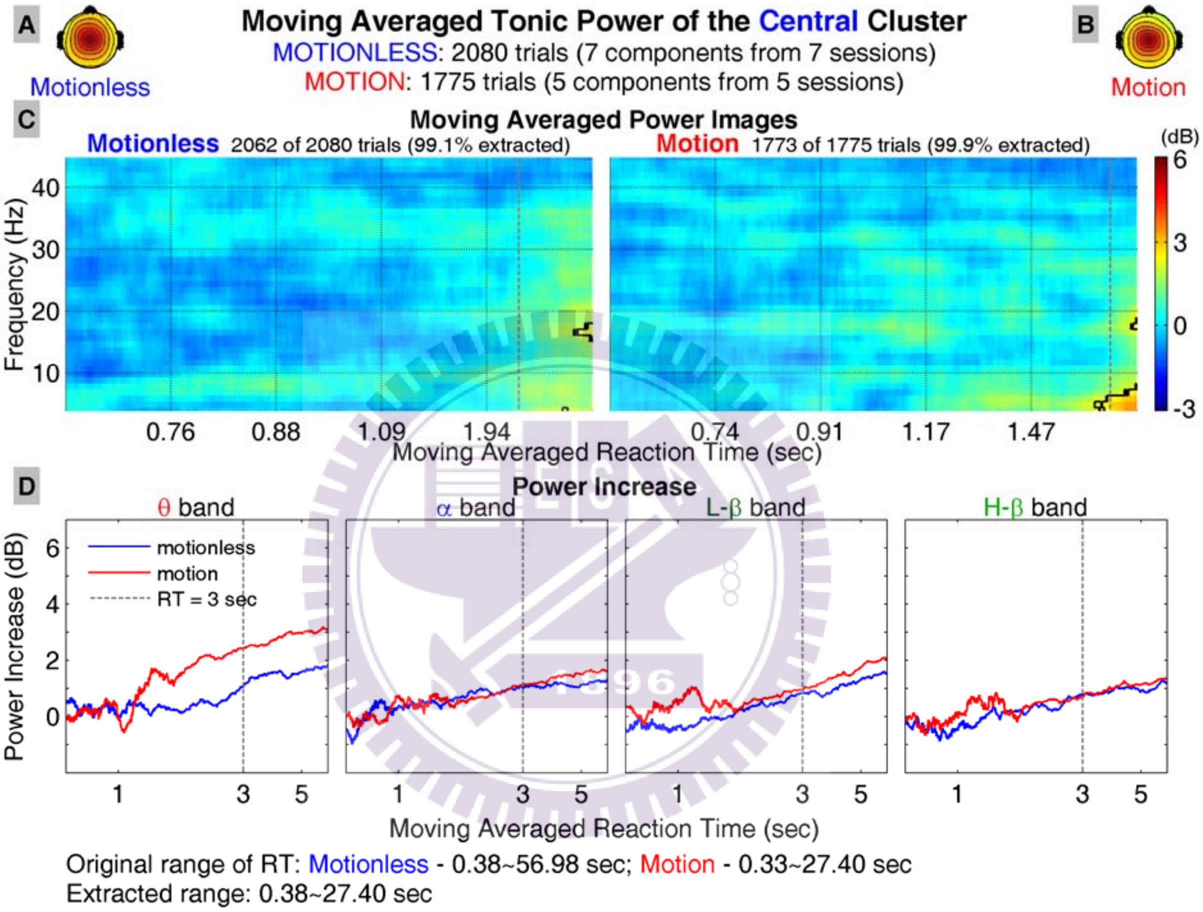

Figure 33: Comparison of the trends of tonic power spectra between motionless and motion conditions of the central cluster. All conventions follow Figure 32.

4.3.2.3 The Parietal and Somatomotor Clusters

The results of the parietal, left somatomotor, and right somatomotor clusters in both conditions (Figure 34-Figure 36) have similar trends in their tonic power spectra. The power images in the parietal and left somatomotor clusters show significant power increase in theta band in motionless datasets when RTs are longer than 3 sec; however, the power spectra of all three clusters in the motion condition show do not show any significant increase, and all three clusters in the motion condition show relative lower in alpha and beta bands than that in the motionless condition. These comparisons suggest that kinesthetic stimuli influence the alpha and beta band power in the parietal and somatomotor clusters.

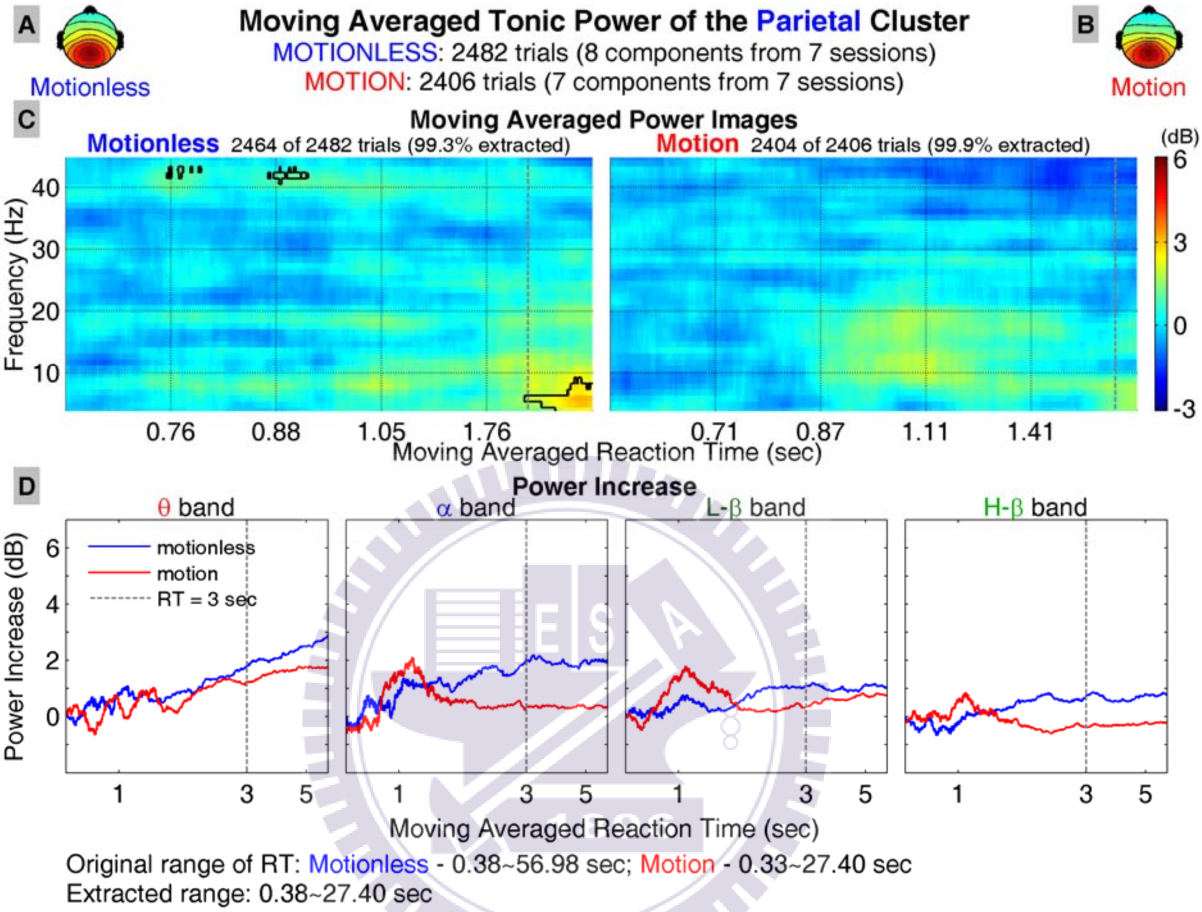

Figure 34: Comparison of the trends of tonic power spectra between motionless and motion conditions of the parietal cluster. All conventions follow Figure 32.

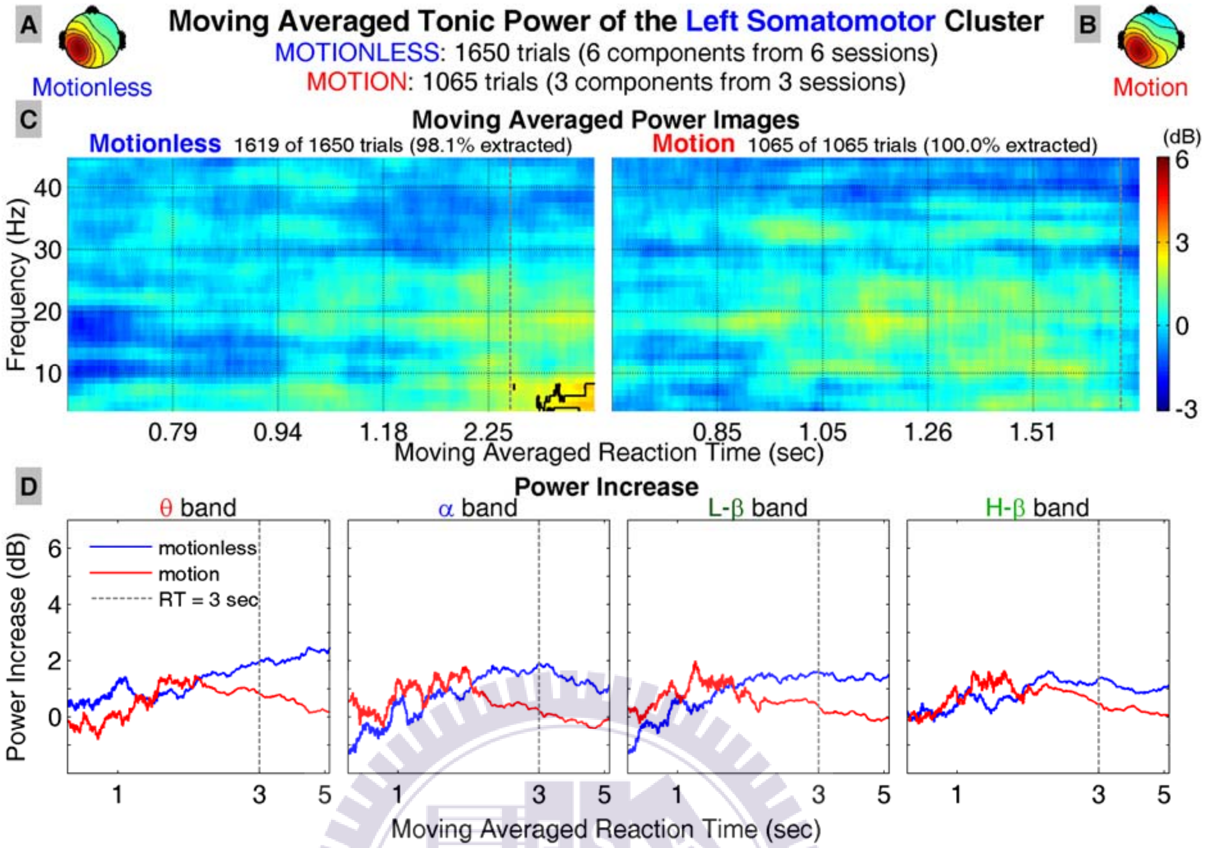

Original range of RT: Motionless - 0.38~56.98 sec; Motion - 0.45~22.52 sec
Extracted range: 0.45~22.52 sec

Figure 35: Comparison of the trends of tonic power spectra between motionless and motion conditions of the left somatomotor cluster. All conventions follow Figure 32.

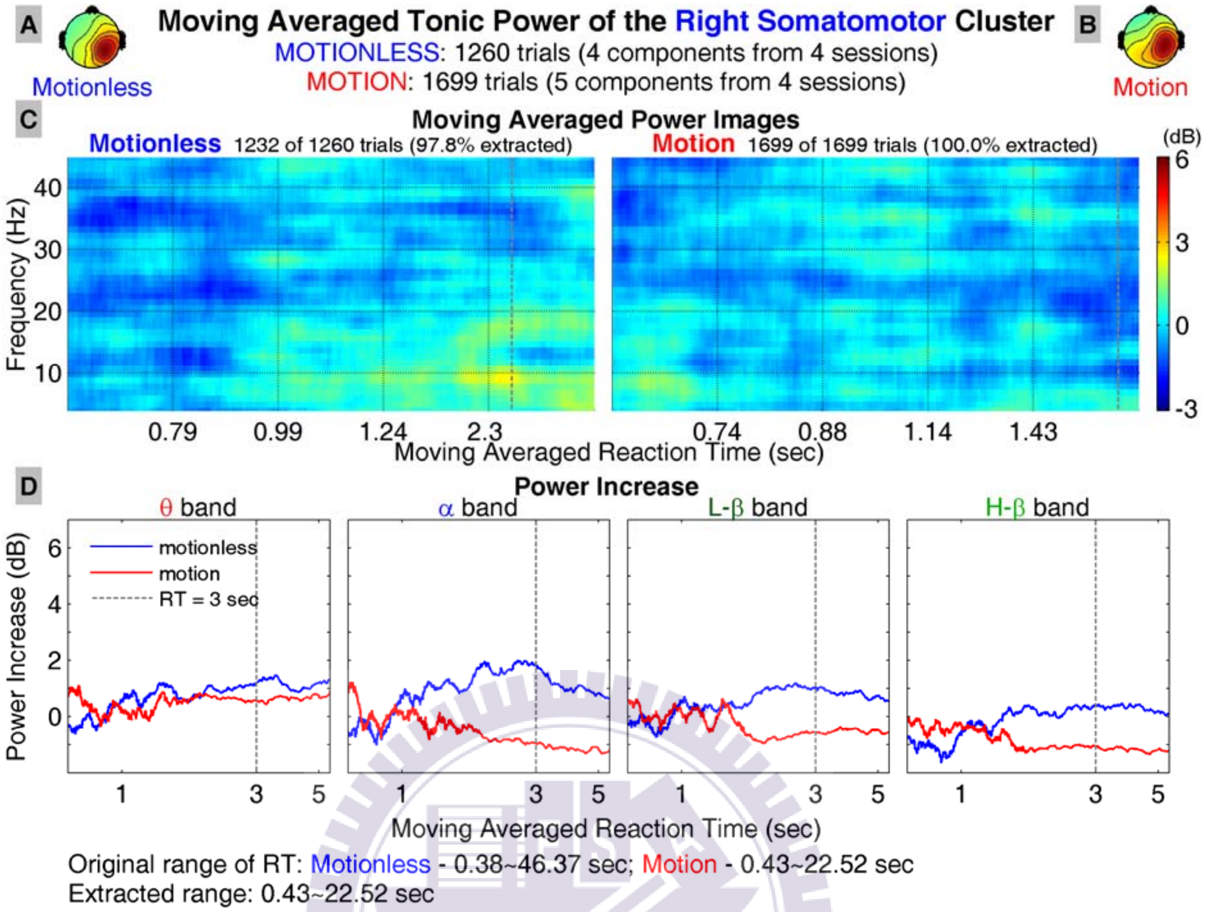

Figure 36: Comparison of the trends of tonic power spectra between motionless and motion conditions of the right somatomotor cluster. All conventions follow Figure 32.

4.3.2.4 The Occipital Clusters

The tonic power spectra of three occipital clusters (Figure 37-Figure 39) show different trends between motion and motionless conditions. The power images in both conditions show power increase below 30 Hz when RTs increase in all three clusters; furthermore, the motion condition shows significant power increase at lower RTs than those in the motionless condition. The power increase in beta band becomes insignificant when RTs further increase in the tangential cluster.

The trends of alpha and beta band power in all three clusters increase at shorter RTs and then decrease at longer RTs, and these trends of increase-and-decrease trends are steeper in the motion condition then those in the motionless condition. All three clusters show monotonic increase in theta band power when RTs increase, and the increase in the theta band power of the occipital midline and bilateral occipital clusters in the motion condition is faster than those in the motionless condition. These comparisons suggest that kinesthetic stimuli show major influence on the trends of alpha and beta band power in the occipital clusters.

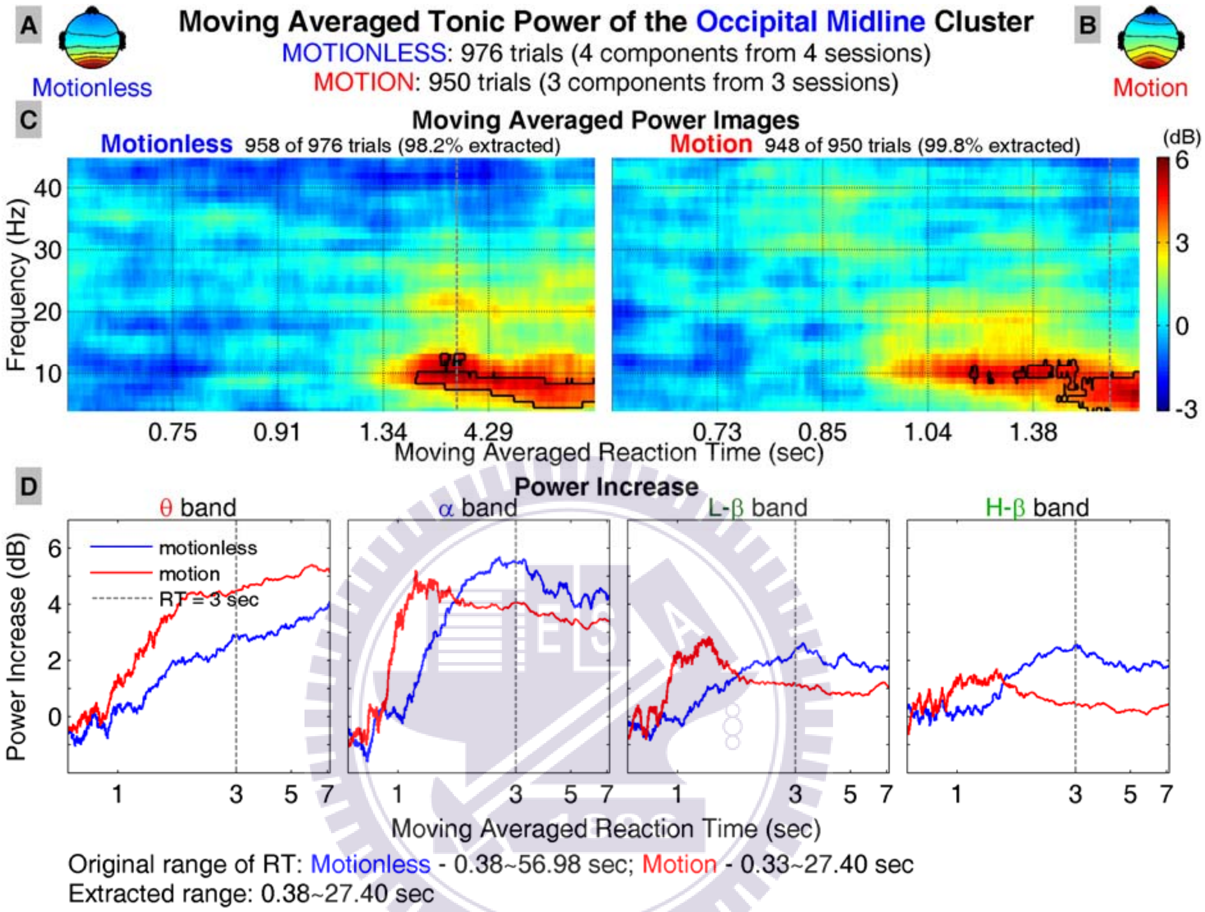

Figure 37: Comparison of the trends of tonic power spectra between motionless and motion conditions of the occipital midline cluster. All conventions follow Figure 32.

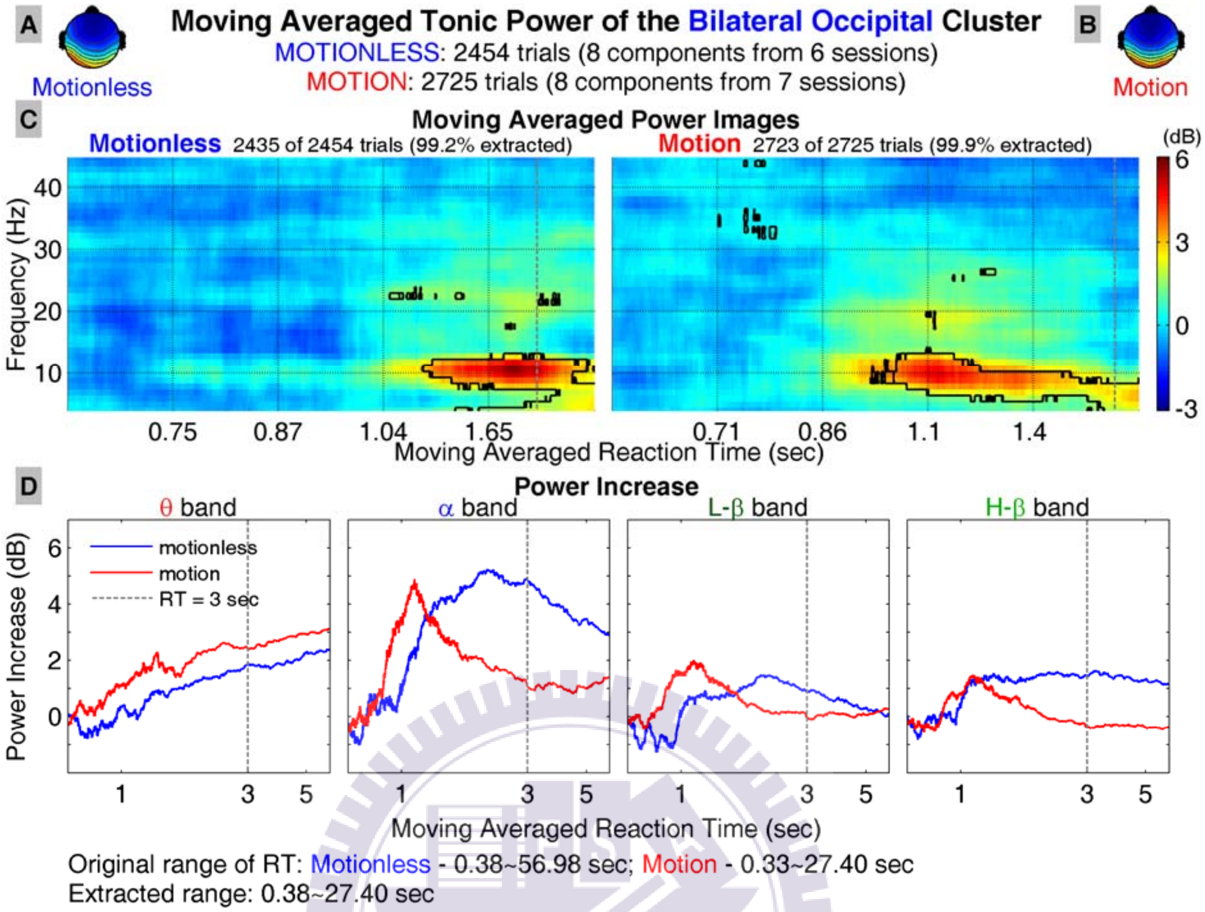

Figure 38: Comparison of the trends of tonic power spectra between motionless and motion conditions of the bilateral occipital cluster. All conventions follow Figure 32.

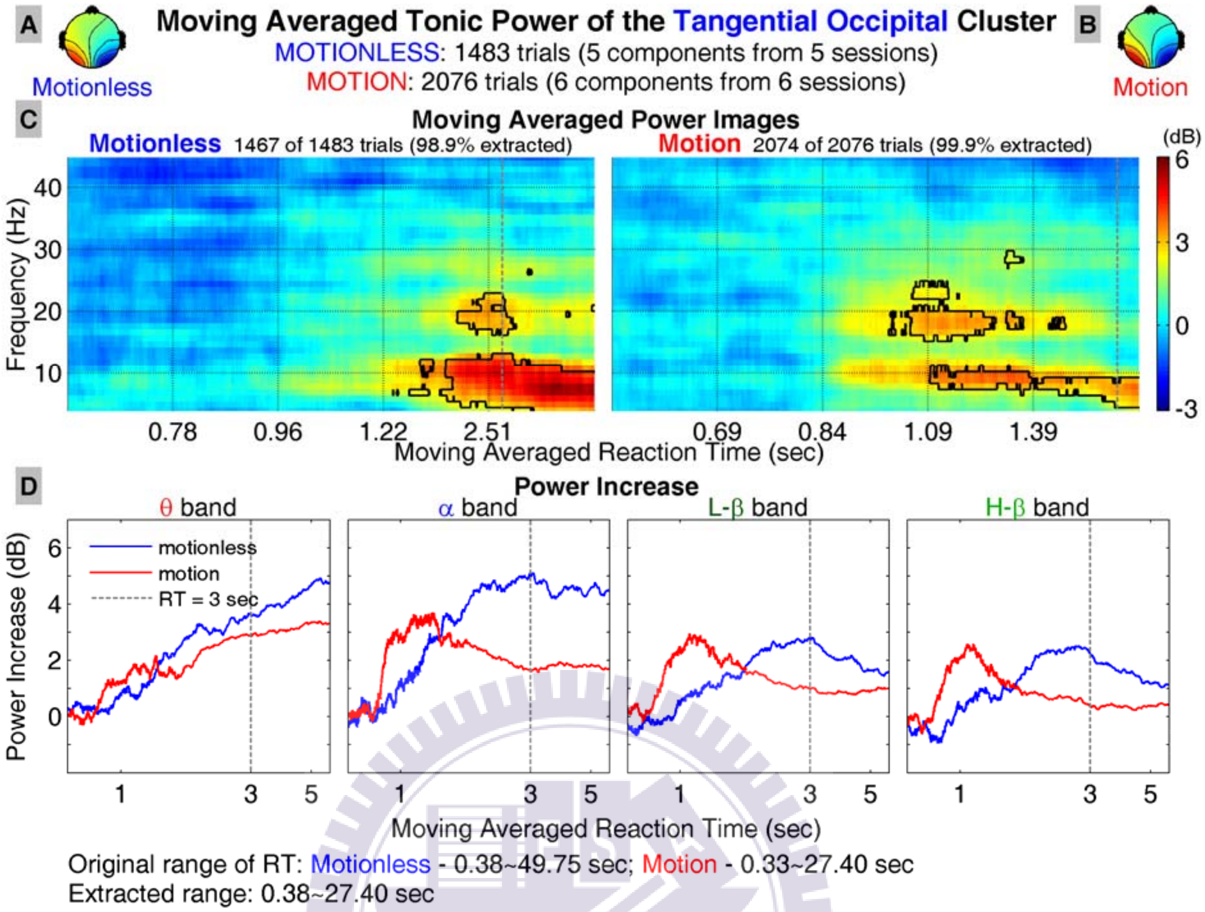

Original range of RT: Motionless - 0.38~49.75 sec; Motion - 0.33~27.40 sec
Extracted range: 0.38~27.40 sec

Figure 39: Comparison of the trends of tonic power spectra between motionless and motion conditions of the tangential occipital cluster. All conventions follow Figure 32.

Chapter V Discussions

5.1 Behavior Indices in the Driving Simulator and in the Real Life

Driving is a complex behavior in the real life and could be difficult to study in a laboratory setting. The goal of this study is to establish the relation between changes in EEG power spectra and fluctuations of driving performance in a simulated driving environment; hence, the first step is to define a behavioral index of driving performance that objectively and quantitatively measures the subject's vigilance levels during continuous driving. The event-related lane departure paradigm uses reaction time as a direct and instantaneous measure of the subject's readiness to respond to deviation in each trial, and average reaction time can also be obtained in a longer window (e.g., 90 sec) to assess the subject's "global" or "contextual" vigilance levels at a larger time scale. It is assumed that the longer it takes to respond to the deviation, the lower the subject's vigilance level is.

The mapping between EEG power spectra and reaction time established on a driving simulator may be used as a norm for the development of drowsiness detection system. In the real life, although it could be difficult to define explicit events and measure reaction times, the changes in EEG power spectra can be used to predict the subject's implicit reaction time to situations on the road. Several next generation cars are already equipped with intelligent systems (e.g., electronic stability control, ESC [24] and lane departure warning system, LDWS [25]) that monitor the vehicle's stability or lane position. These behavioral measures could be integrated into the EEG-based drowsiness detection system to provide better estimation of the driver's vigilance level.

5.2 Effects of Kinesthetic Stimuli

5.2.1 Behavior Data

In Section 4.3.1, the results show that the average RT in the motion datasets is shorter than that in the motionless datasets; in addition, the first one-third and the last one-third of the sorted RTs in the motion datasets are lower than the corresponding portions of RTs in the motionless datasets. The difference of RTs between motion and motionless datasets could be explained by the uneven distribution of alertness levels across different sessions, i.e. subjects happen to be more alert in the motion sessions than in their motionless sessions, and the other possibility is that the shorter RT distribution could be explained by the kinesthetic stimuli during motion sessions. In our recent experiments (data not shown in this study), all subjects reported that the centrifugal force after deviation onset in the motion sessions seemed to provide the kinesthetic cues for responses; therefore, it could be suggested that the subjects in this study had similar experience and were able to respond with shorter RTs during motion sessions. This is an interesting topic that requires further investigation.

5.2.2 Tonic Power Spectra

In Section 4.3.2, the comparisons between motion and motionless conditions suggest that kinesthetic stimuli have almost no influence on the rising trend of theta band power except that in the left somatomotor cluster; furthermore, theta band power of the central cluster is generally higher in the motion condition than that in the motionless sessions.

The power in alpha and beta bands is suppressed at longer RTs (> 2 sec) in motion sessions in most IC clusters. In the central cluster, the kinesthetic stimuli have almost no effect on power in the alpha and beta bands. The power images of the parietal and somatomotor clusters in the motion sessions show no significant changes from their alert baseline power spectra.

In the occipital clusters, the trends of increase and decrease of power are steeper in the motion condition than those in the motionless condition; in addition, significant power increase occurs at shorter RTs in the motion condition than those in the motionless condition. These results could provide a foundation for the development of drowsiness detection system on the road since the driver receives kinesthetic stimuli (similar to those simulated by the motion platform) in real-life driving.

5.3 Effects of Driving Events

Real-life driving usually involves a lot of motor activities, including steering, braking, stepping on the gas paddle, and shifting gears, in response to events or situations on the road. These events and responses generally induce transient (phasic) perturbation in the EEG power spectra, which are referred to as event-related spectra perturbations (ERSPs) [17][26]; however, it is not known whether these phasic activities may affect the trends in EEG power spectra and the validity of drowsiness detection. In Chapter IV, tonic EEG power spectra were only computed from a 1-sec window prior to deviation onset in each epoch, which was less contaminated by phasic activities; in this section, EEG power spectra from the whole 8-sec epoch, which contained the effects of different events (deviation onset, response onset, and response offset), were estimated using the same methods described in Section 3.6 and Section 3.7. The discussions in this section suggest that phasic activities did influence the trends in some frequency bands of some IC clusters. The goal for developing a reliable drowsiness detection system is to identify those IC clusters and frequency bands that are less affected by phasic activities.

Only motion datasets are discussed since the experiment conditions are closer to real-life driving than their motionless counterparts.

5.3.1 The Frontal Cluster

Figure 40 shows the comparison between “tonic” (only the pre-deviation period in each epoch) and “mixed” (both pre- and post-deviation period in each epoch) power spectra of the frontal cluster. The power images (Figure 40 A) show that increase in “mixed” power spectra is less salient than that in the “tonic” ones; however, significant theta band power increase occurs at lower RTs in the “mixed” power spectra. The trends in Figure 40 B show the “mixed” power increase in the theta band is lower than that of “tonic” power increase at longer RTs, but the monotonic rising trend is not affected by phasic activities in the “mixed” power spectra, suggesting that the theta band power in the frontal cluster could be a stable index for drowsiness detection in real-life driving.

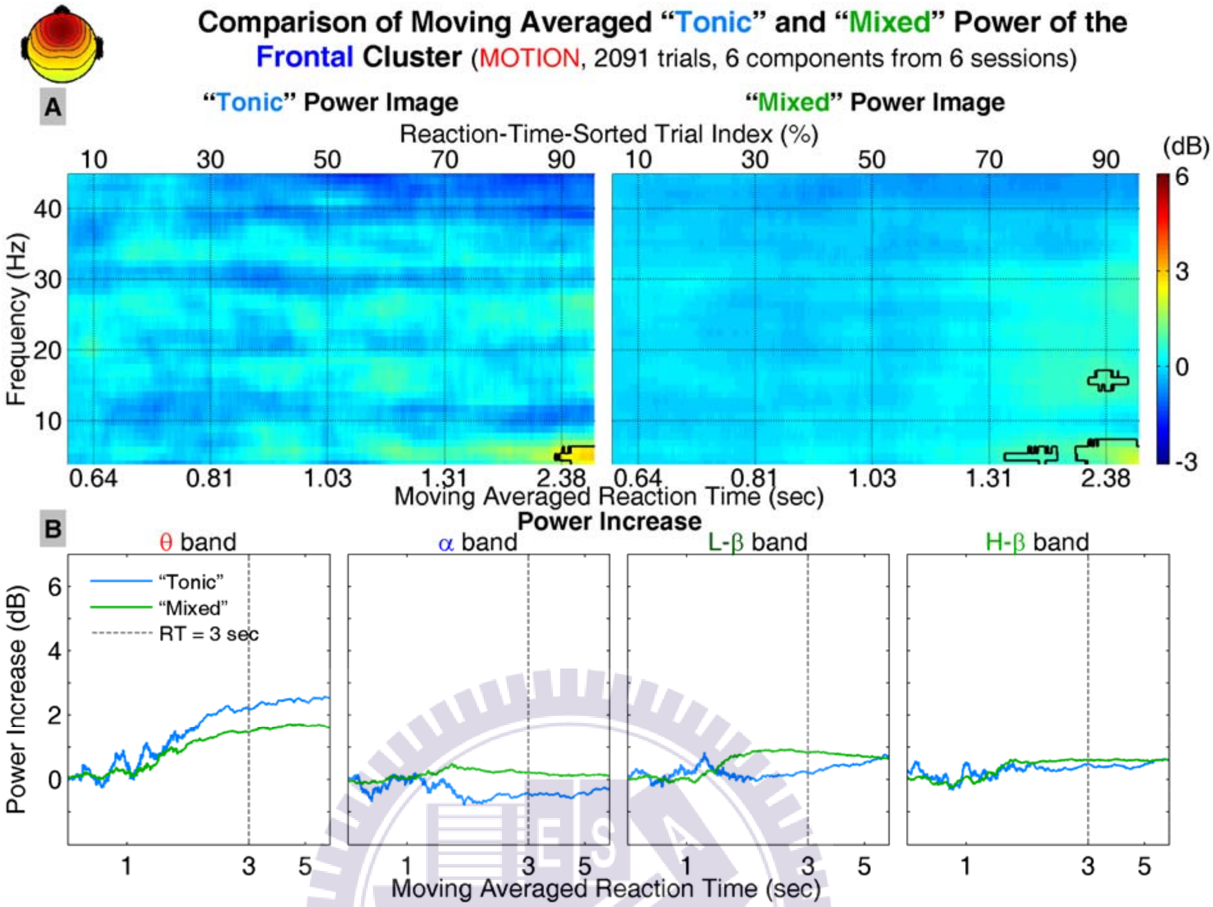

Figure 40: Comparison of the trends between "tonic" and "mixed" power spectra of the frontal cluster. A: moving averaged power images (left panel: "tonic" power spectra, right panel: "mixed" power spectra; regions inside contour: $p < 10^{-10}$ by two-tailed t-test, corrected). B: trends of power increase in four frequency bands extracted from A; light-blue traces: trend in "tonic" power, light-green traces: trend in "mixed" power).

5.3.2 The Central and Parietal Clusters

The comparison between the trends in "tonic" and "mixed" power spectra in the central cluster is shown in Figure 41. The "mixed" power image shows significant increase in both theta and beta bands at long RTs (> 2.5 sec), and the overall "mixed" power in the theta and alpha bands is lower than that in the "tonic" power spectra. The rising trend of theta band power in the "mixed" power spectra suggest that theta band power is less affected by "phasic" activities and may be suitable for drowsiness detection in real-life driving.

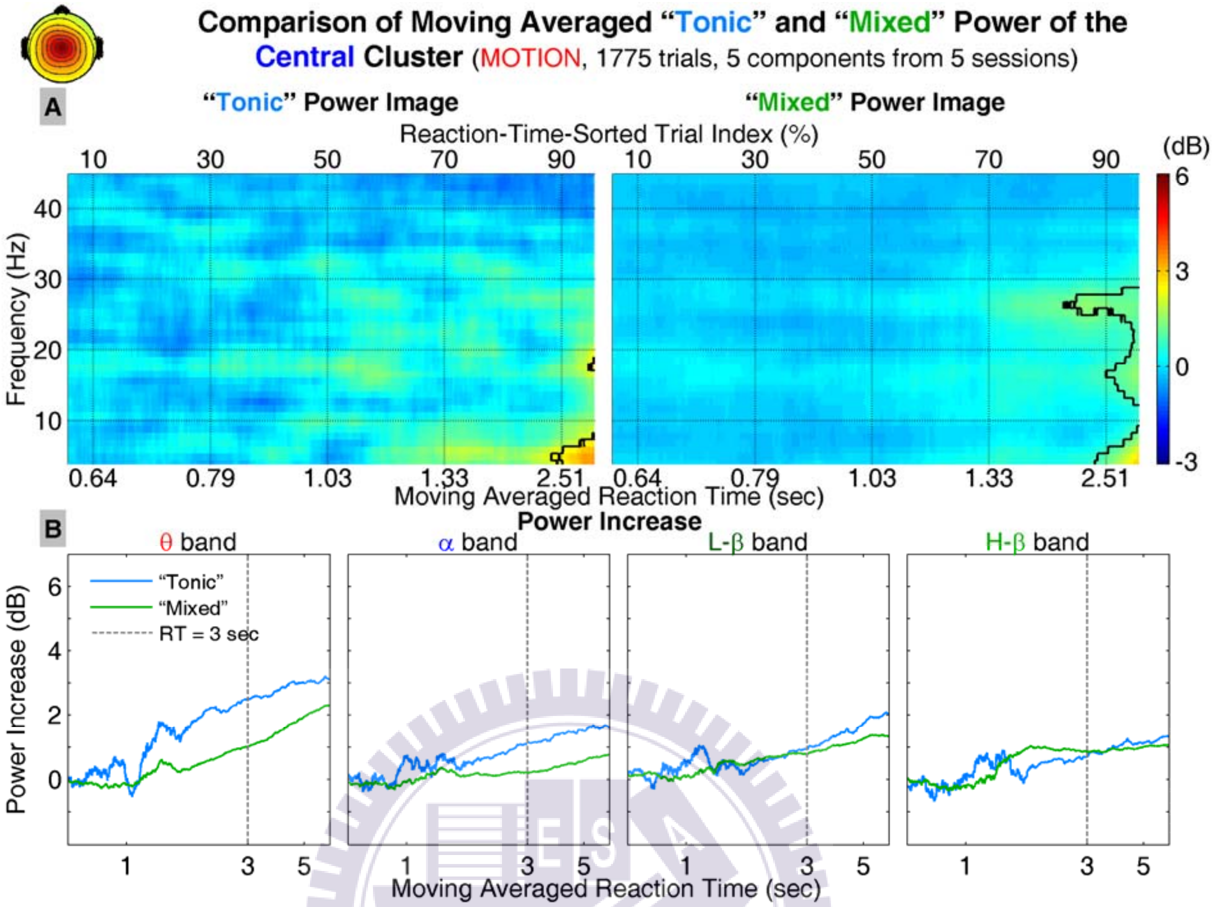

Figure 41: Comparison of the trends between "tonic" and "mixed" power spectra of the central cluster. Other conventions follow Figure 40.

Figure 42 shows the comparison between "tonic" and "mixed" power spectra in the parietal cluster. The power images show almost no changes in "mixed" power spectra except theta band power when RTs are longer than ~2.22 sec. The trends of "mixed" power only show small increase in the theta band and remain unchanged in other frequency bands. These results suggest that "mixed" power spectra of the parietal cluster are largely affected by "phasic" activities, and may not be suitable for drowsiness detection.

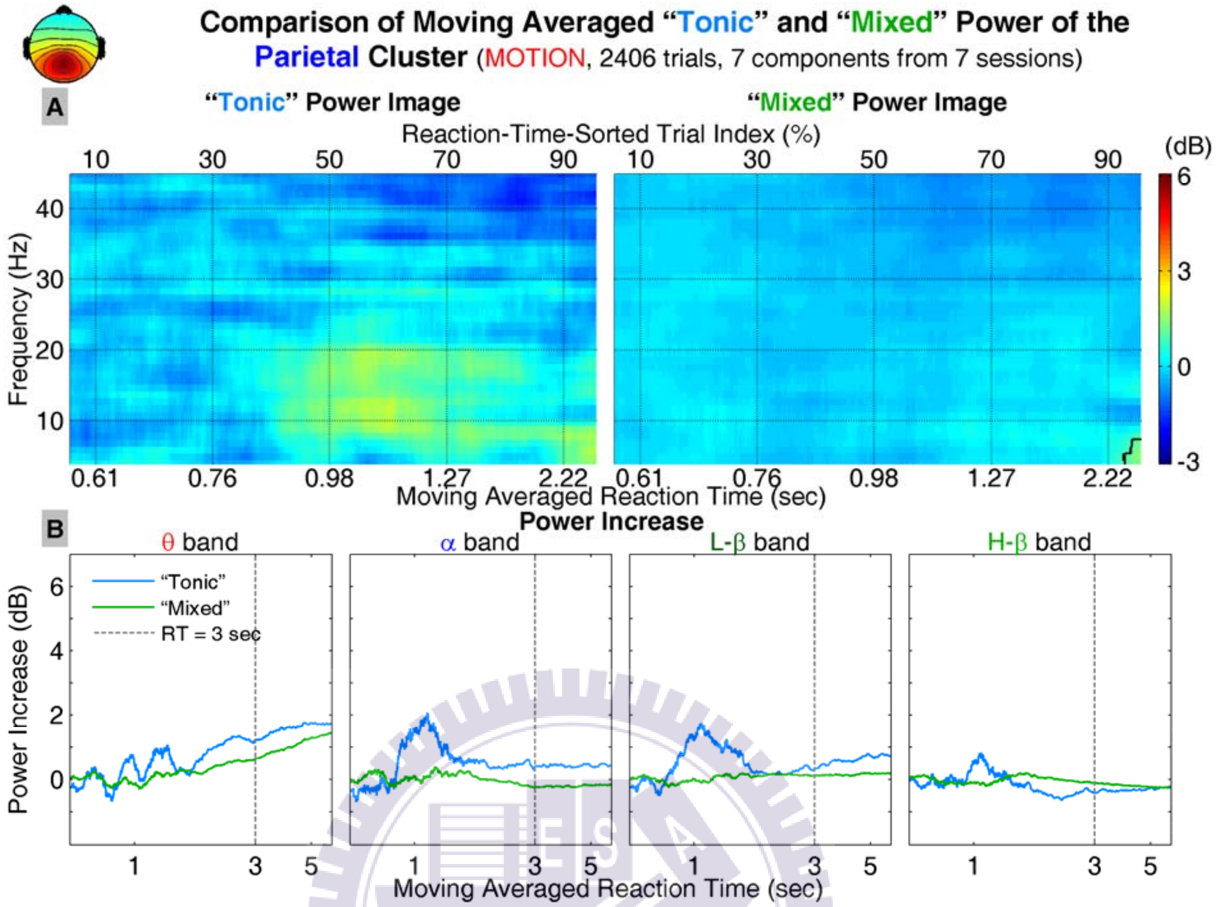

Figure 42: Comparison of the trends between "tonic" and "mixed" power spectra of the Parietal cluster. Other conventions follow Figure 40.

5.3.3 The Somatomotor Clusters

Figure 43 and Figure 44 show the comparisons of trends between "tonic" and "mixed" power spectra in the left and right somatomotor clusters. The power images and trends of the left somatomotor cluster show the changes in "mixed" power spectra are generally smaller than those in the "tonic" power spectra; moreover, alpha and beta band power is further suppressed with increasing RTs. The power images and trends of the right somatomotor cluster do not show consistent difference between "tonic" and "mixed" power spectra in four frequency bands. These results suggest that the trends of power spectra of the somatomotor clusters are affected by motor responses and are not suitable for drowsiness detection.

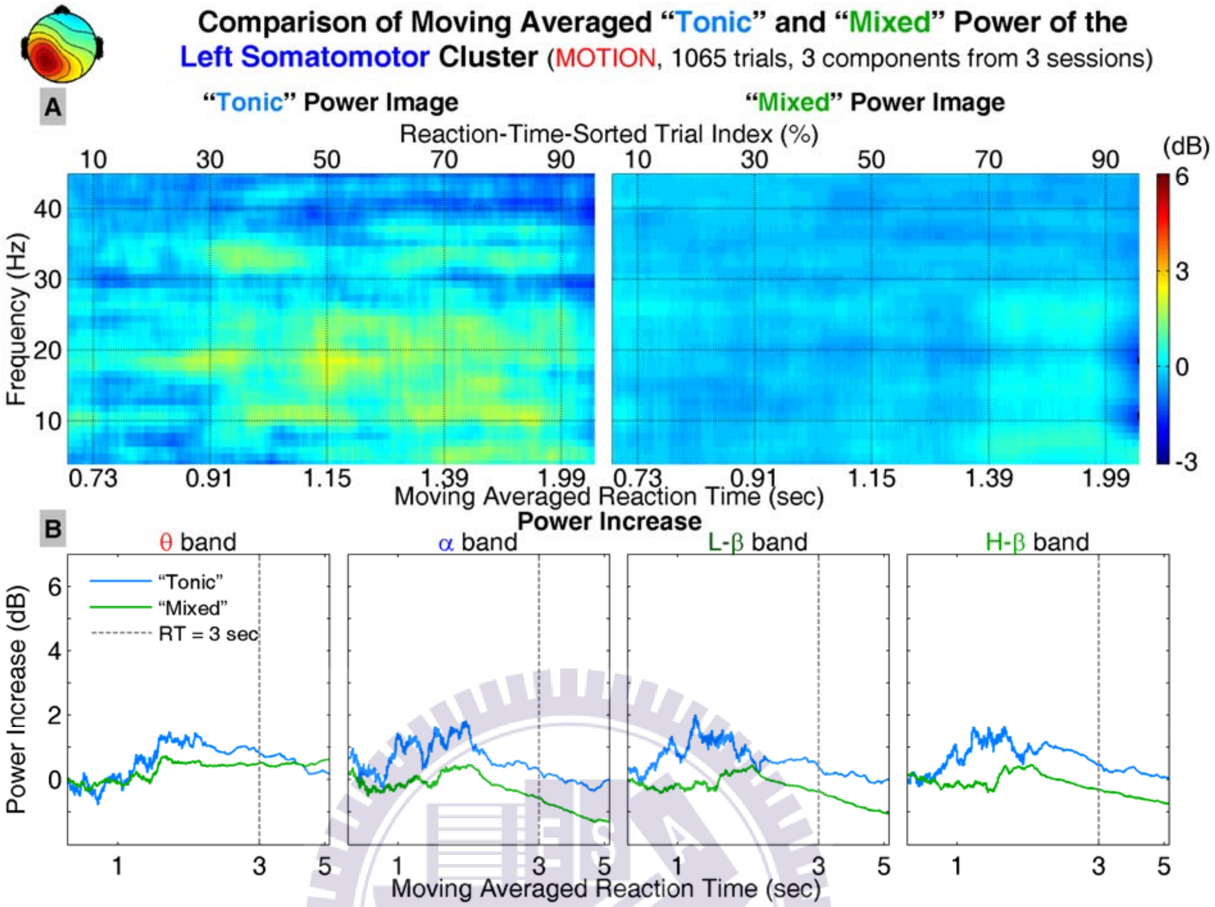

Figure 43: Comparison of the trends between "tonic" and "mixed" power spectra of the left somatomotor cluster. Other conventions follow Figure 40.

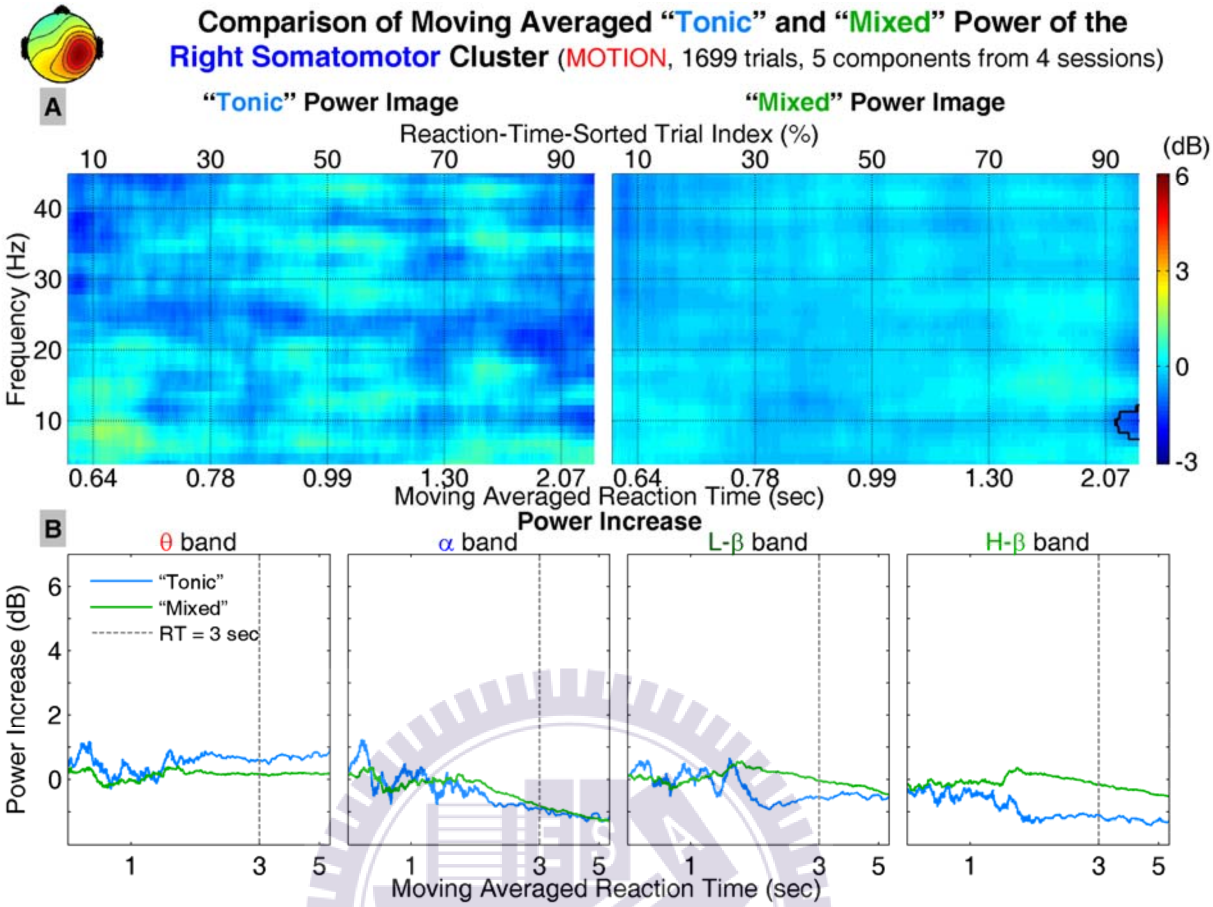

Figure 44: Comparison of the trends between "tonic" and "mixed" power spectra of the right somatomotor cluster. Other conventions follow Figure 40.

5.3.4 The Occipital Clusters

Figure 45-Figure 47 show the comparisons of trends between "tonic" and "mixed" power spectra in three occipital clusters. The power images and trends show that the overall power in the "mixed" power spectra is generally lower than that of the "tonic" power spectra in all three occipital clusters. In particular, alpha band power is greatly reduced in the "mixed" power spectra, which could be explained by the subject's attention and responses following deviation onset. The trends of theta band power in the "mixed" power spectra remain virtually the same as those in the "tonic" power spectra; in addition, significant power increases occur at longer RTs in the "mixed" power spectra. These results suggest that theta band power in the occipital clusters could be a reliable index for drowsiness detection in situations that are similar to real-life driving.

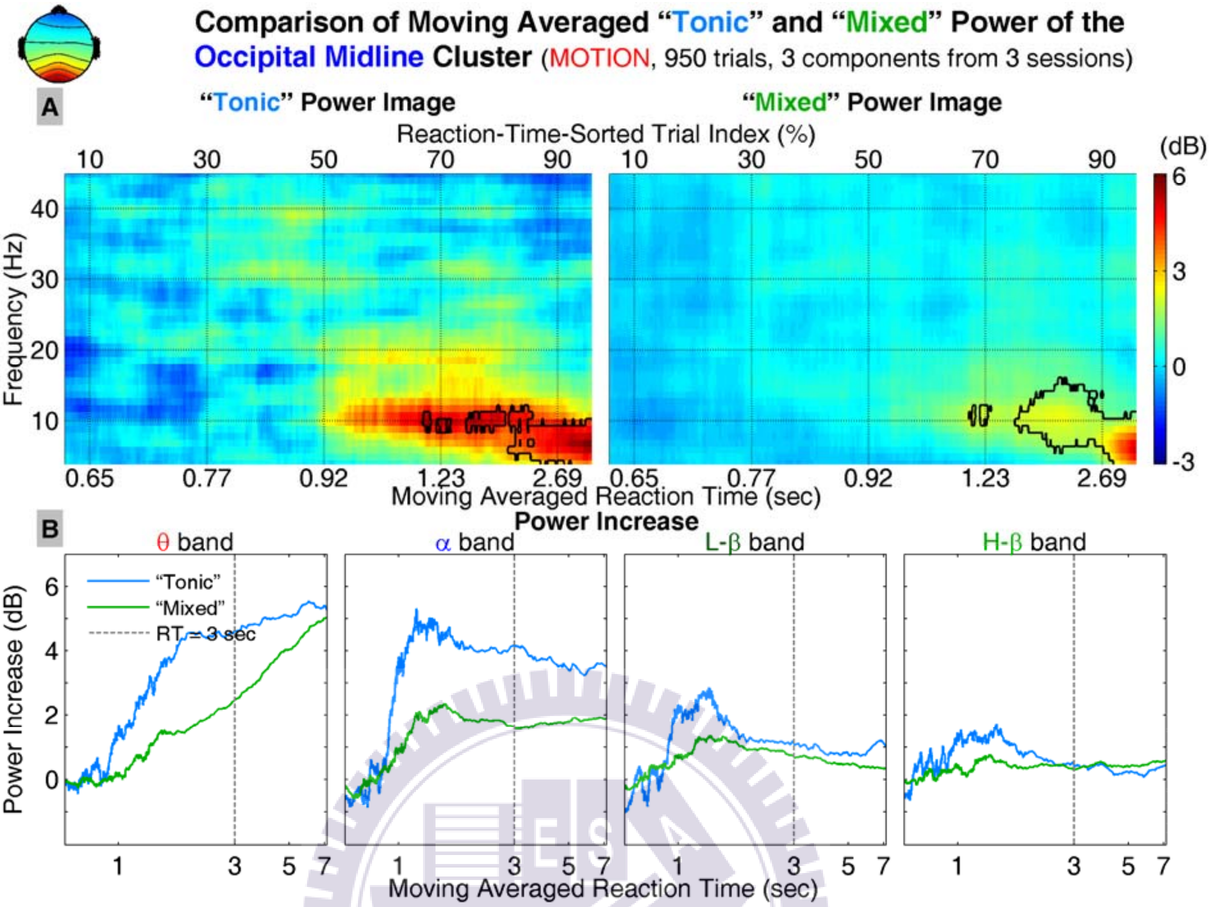

Figure 45: Comparison of the trends between "tonic" and "mixed" power spectra of the occipital midline cluster. Other conventions follow Figure 40.

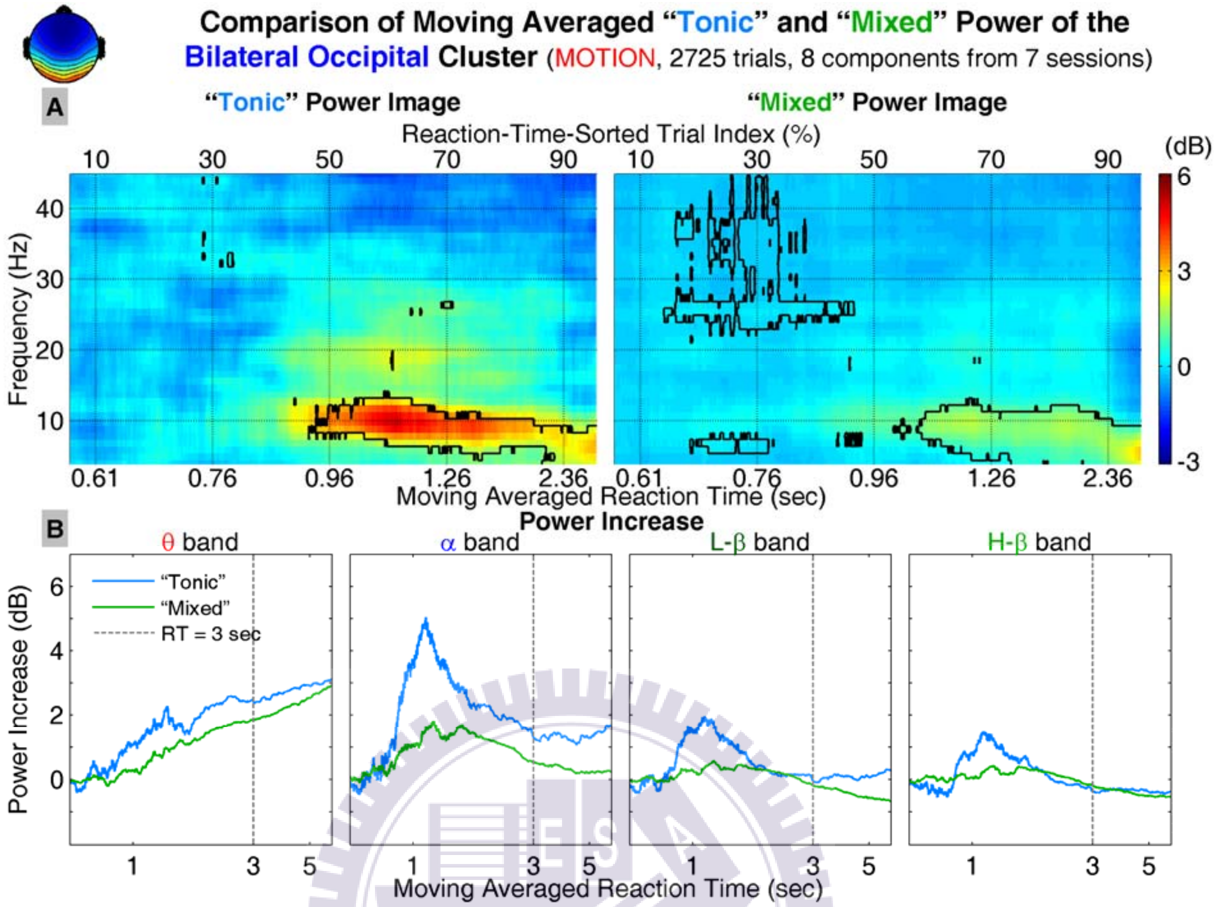

Figure 46: Comparison of the trends between "tonic" and "mixed" power spectra of the bilateral occipital cluster. Other conventions follow Figure 40.

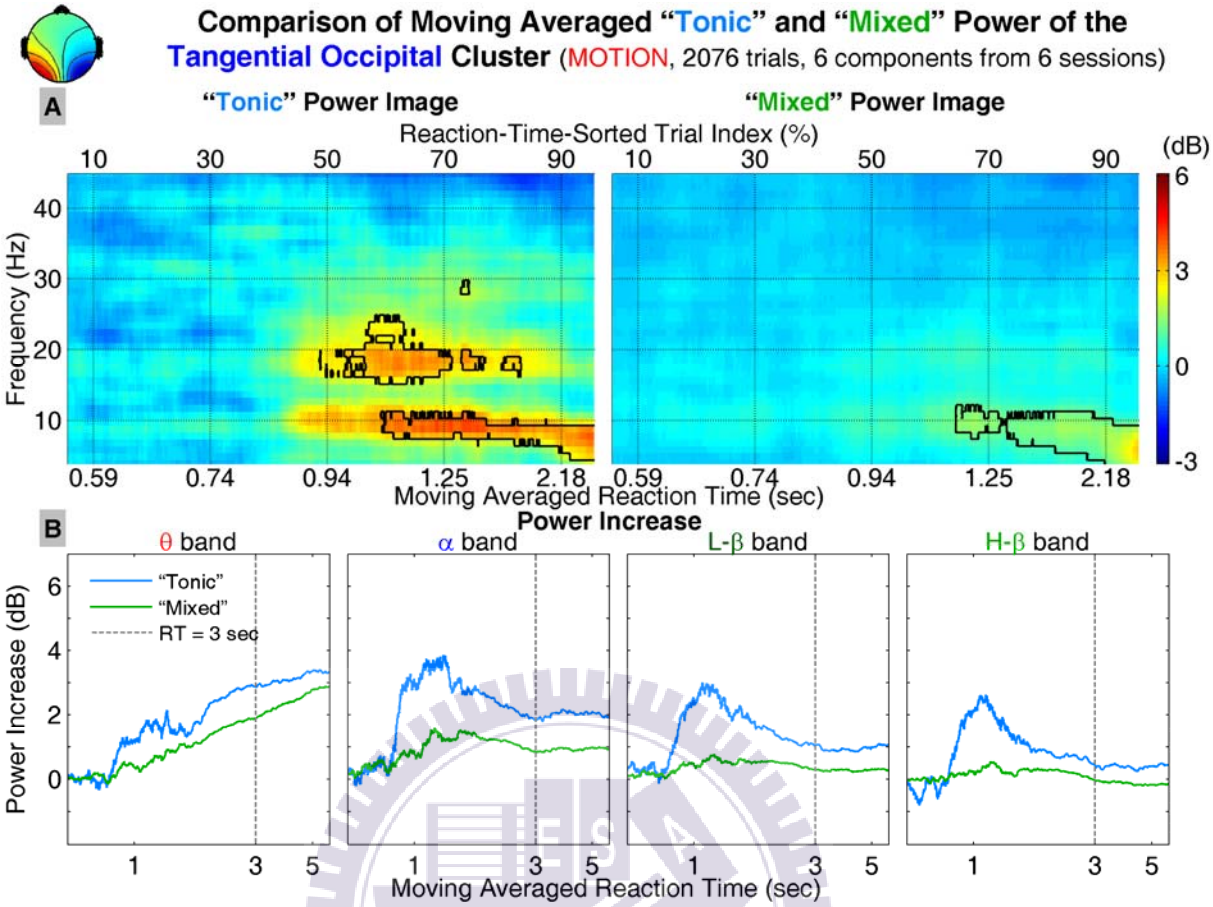

Figure 47: Comparison of the trends between "tonic" and "mixed" power spectra of the tangential occipital cluster. Other conventions follow Figure 40.

5.4 EEG Power Spectra in the Bilateral Occipital Cortex

In this study, the tonic power spectra in the bilateral occipital cortex exhibit a rising trend and then start to decline with increasing RTs in the alpha band power, and this phenomena is often referred to as the "biphasic" pattern [27]. In other sustained attention studies [13][14][17], they only show alpha and theta band increase with RTs or error, and did not show the biphasic pattern reported in this study. This is likely because that only a small percentage of trials have RTs longer than 3 sec, which suggests that their subjects were not very drowsy across all sessions in [14]. The theta band power increases monotonically with the increase of RTs. The increases in theta and alpha band power during long RTs periods are consistent with the findings in other studies [9], [13]-[17].

This study further shows the trends of power spectral changes in motion sessions during which the subjects received kinesthetic stimuli. The trend of theta band power remains the same in the motion sessions, whereas alpha band power shows steeper increase and decrease trend than that in the motionless sessions; in addition, these trends remain the same when “phasic” activities were included in the power spectral analysis.

5.5 The Optimal Cluster and Frequency Bands for Drowsiness Detection

From the results and discussions above, the bilateral occipital cluster could be considered the optimal cluster for drowsiness detection for two reasons: the trends in theta band power were quite stable in both motion and motionless conditions and were not influenced by driving events or the subject’s responses, and the bilateral occipital component is the most prevalent across sessions. Table 3 shows that there are 14 bilateral occipital components from 10 sessions in the motionless datasets (total 11 sessions) and 8 such components from 7 sessions in the motion datasets (total 7 sessions). On average, at least one such component exists in a session.

EEG power in the theta and alpha bands rises with increasing RTs; however, when RTs become even longer, alpha band power starts to decline, while theta band power continues to increase. Hence, EEG power on the theta band could be suitable for estimating drivers’ vigilance level, whereas that in the alpha band could be an auxiliary index.

TABLE 3: NUMBER OF COMPONENTS IN THE IDENTIFIED CLUSTERS

Condition Cluster	Motionless Datasets (11 Sessions)	Motion Datasets (7 Sessions)
Frontal	8	6
Central	9	5
Parietal	12	7
Left Somatomotor	9	3
Right Somatomotor	7	5
Occipital Midline	6	3
Bilateral Occipital	14	8
Tangential Occipital	7	6

Chapter VI Conclusions

In this study, subjects participated in simulated long-haul driving experiments on a motion platform in an immersive VR-based environment, during which their brain waves (EEG) and driving behavior were recorded. Driving performance was measured by reaction time (RT) as defined in an event-related lane-departure paradigm. Following strict criteria for artifact rejection in behavioral and EEG data, independent component analysis (ICA) was used to decompose EEG signals into independent brain processes, and power spectra were computed from the activation time course of each independent component. Independent components with similar features, such as topographic maps, dipole sources, and alert baseline power spectra, were grouped into clusters across subjects.

The results show that the power spectra of independent brain processes in the bilateral occipital regions are optimal for monitoring subject's vigilance states for two reasons: the bilateral occipital components are most prevalent across subjects, and the trends of EEG power spectral changes are most stable across different conditions. The tonic power in the alpha band initially rises with increasing RTs, but reverses to the downward trend when RTs become even longer; however, theta band power increases monotonically with RTs, and the center of mass in the power spectra shifts to lower frequencies at longer RTs. The trends of power spectral changes in the motion sessions are similar to those in the motionless sessions, but the upward and downward trends in alpha band power are steeper in the motion sessions; furthermore, significant power increase occurs at shorter RTs in the motion sessions than those in the motionless sessions. Finally, the rising trends of theta band power are affected by neither kinesthetic stimuli in the motion sessions nor "phasic" activities induced by events and responses.

This study not only shows results that are consistent with existing studies on drowsy driving, but also reports new findings in conditions that are close to real-life driving. These results may provide insights into the design of drowsiness detection system on the road.

References

[1] National Sleep Foundation (NSF), USA, http://drowsydriving.org/about/

[2] D. Royal, "National Survey of Distracted and Drowsy Driving Attitudes and Behavior: 2002," National Highway Traffic Safety Administration (NHTSA), U.S. Department of Transportation, April 2003

[3] NSF, USA, "2009 *Sleep in America*™ Poll: Summary of Findings," 2 March 2009

[4] K. Kozak, J. Pohl, W. Birk, J. Greenberg, B. Artz, M. Blommer, L. Cathey, and R. Curry, "Evaluation of Lane Departure Warnings for Drowsy Drivers," Proceedings of the Human Factors and Ergonomics Society 50th Annual Meeting, pp. 2400-2404, San Francisco, California, USA, 16-20 October 2006

[5] M. Rimini-Doering, T. Altmueller, and U. Ladstaetter, "Effects of Lane Departure Warning on Drowsy Drivers' Performance and State in a Simulator," Proceedings of the Third International Driving Symposium on Human Factors in Driver Assessment, Training and Vehicle Design, pp. 88-95, Rockport, Maine, USA, 27-30 June 2005

[6] D. K. McGregor and J. A. Stern, "Time on Task and Blink Effects on Saccade Duration," Ergonomics, Volume 39, Issue 4, pp. 649-660, March 1996

[7] J. C. Popieul, P. Simon, and P. Loslever, "Using Driver's Head Movements Evolution as a Drowsiness Indicator," Proceedings IEEE Intelligent Vehicles Symposium 2003, pp. 616-621, 9-11 June 2003

[8] Q. Ji, Z. Zhu, and P. Lan, "Real-Time Nonintrusive Monitoring and Prediction of Driver Fatigue," IEEE Transactions on Vehicular Technology, Volume 53, Issue 4, pp. 1052-068, 26 July 2004.

[9] C. -T. Lin, R. -C. Wu, S. -F. Liang, W. -H. Chao, Y. -J. Chen, and T. -P. Jung, "EEG-Based Drowsiness Estimation for Safety Driving Using Independent Component Analysis," IEEE Transactions on Circuits and Systems, Volume 52, Issue 12, pp. 2726-2738, 12 December 2005

[10] C. -T. Lin, Y. -C. Chen, T. -Y. Huang, T. -T. Chiu, L. -W. Ko, S. -F. Liang. H. -Y. Hsieh, S. -H. Hsu, and J. -R. Duann, "Development of Wireless Brain Computer Interface with Embedded Multitask Scheduling and its Application on Real-Time Driver's drowsiness Detection and Warning," IEEE Transactions on Biomedical Engineering, Volume 55, Issue 5, pp. 1582-1591, May 2008

[11] C. -T. Lin, L. -W. Ko, J. -C. Chiou, J. -R. Duann, R. -S. Huang, S. -F. Liang. T. -W. Chiu, and T. -P. Jung, "Noninvasive Neural Prostheses Using Mobile and Wireless EEG," Proceedings of the IEEE, Volume 96, Issue 7, pp. 1167-1183, July 2008

[12] J. Beatty, A. Greenberg, W. P. Deibler, and J. F. O'hanlon, "Operant Control of Occipital Theta Rhythm Affects Performance in a Radar Monitoring Task," Science, Volume 183, No. 4127, pp. 871-873, 1 March 1974

[13] R. -S. Huang, T. -P. Jung, A. Delorme, and S. Makeig, "Tonic and Phasic Electroencephalographic Dynamics During Continuous Compensatory Tracking," NeuroImage, Volume 39, Issue 4, pp. 1896-1909, 15 February 2008

[14] R. -S. Huang, T. -P. Jung, and S. Makeig, "Tonic Changes in EEG Power Spectra during Simulated Driving," D. D. Schmorrow, I. V. Estabrooke, and M. Grootjen (Editors): Augmented Cognition, HCII 2009, LNAI 5638, pp. 394-403, San Diego, CA, USA, 22-24 July 2009

[15] J. -L. Jeng, "Electroencephalographic Spectral Changes from Alertness to Drowsiness in a Driving Simulator," National Chiao Tung University, Master Thesis, October 2007

[16] R. -S. Huang, T. -P. Jung, J. -R. Duann, S. Makeig and M. I. Sereno, “Imaging Brain Dynamics During Continuous Driving Using Independent Component Analysis,” 35th Annual Meeting of the Society for Neuroscience, Abstract, Washington D. C., the USA, 12-16 November 2005

[17] R. -S. Huang, T. -P. Jung, and S. Makeig, “Multi-scale EEG Brain Dynamics during Sustained Attention Tasks,” IEEE International Conference on Acoustics, Speech, and Signal Processing (ICASSP), pp. IV-1173-IV-1176, Honolulu, Hawaii, USA, 4 June 2007

[18] J. Malmivuo and R. Plonsey, Bioelectromagnetism: Principles and Applications of Bioelectric and Biomagnetic Fields, Oxford University Press, USA, 1995

[19] A. Delorme and S. Makeig, “EEGLAB: an Open Source Toolbox for Analysis of Single-Trial EEG Dynamics Including Independent Component Analysis,” Journal of Neuroscience Methods, Volume 134, Issue 1, pp. 9-21, 15 March 2004

[20] J. Onton, M. Westerfield, J. Townsend, and S. Makeig, “Imaging Human EEG Dynamics Using Independent Component Analysis,” Neuroscience and Biobehavioral Reviews, Volume 30, Issue 6, pp. 808-822, 2006

[21] T. -P Jung, S. Makeig, T. -W. Lee, M. J. McKeown, G. Brown, A. J. Bell, and T. J. Sejnowski, “Independent Component Analysis of Biomedical Signals,” The 2nd International Workshop on Independent Component Analysis and Signal Separation, pp. 633-644, 2000.

[22] S. Makeig, A. J. Bell, T. -P Jung, and T. J. Sejnowski., “Independent Component Analysis of Electroencephalographic Data,” D. Touretzky, M. Mozer, and M. Hasselmo (Editors): Advances in Neural Information Processing Systems 8, pp.145-151, June 1996

[23] A. Delorme, T. Fernsler, H. Serby, and S. Makeig, EEGLAB Tutorial, 6.01b, Swartz Center for Computational Neuroscience, San Diego, California, USA, 12 April 2006

[24] J. N. Dang, “Preliminary Results Analyzing the Effectiveness of Electronic Stability Control (ESC) Systems,” NHTSA, U.S. Department of Transportation, September 2004

[25] A. Houser, J. Pierowicz, and D. Fuglewicz, “Concept of Operations and Voluntary Operational Requirements for Lane Departure Warning System (LDWS) On-board Commercial Motor Vehicles,” The Federal Motor Carrier Safety Administration (FMCSA), U. S. Department of Transportation, July 2005

[26] S. Makeig, “Auditory Event-Related Dynamics of the EEG Spectrum and Effects of Exposure to Tones,” Electroencephalography and Clinical Neurophysiology, Volume 86, Issue 4, pp. 283-293, April 1993

[27] T. Ota, R. Toyoshima, and T. Yamauchi, “Measurements by Biphasic Changes of the Alpha Band Amplitude as Indicators of Arousal Level,” International Journal of Psychophysiology, Volume 24, Issues 1-2, pp. 25-37, November 1996

Appendix

A.1 Output Frequency Bins and Time Points of Time-Frequency Transform in the Computing of Tonic Power Spectra

TABLE A1: OUTPUT FREQUENCY BINS

Bins	Frequency (Hz)									
1~10	2.93	3.91	4.88	5.86	6.84	7.81	8.79	9.77	10.74	11.72
11~20	12.70	13.67	14.65	15.63	16.60	17.58	18.55	19.53	20.51	21.48
21~30	22.46	23.44	24.41	25.39	26.37	27.34	28.32	29.30	30.27	31.25
31~40	32.23	33.20	34.18	35.16	36.13	37.11	38.09	39.06	40.04	41.02
41~44	41.99	42.97	43.95	44.92						

TABLE A2: OUTPUT TIME POINTS

Time Points	Times (sec)									
1~10	-.743	-.739	-.735	-.727	-.723	-.719	-.715	-.707	-.703	-.699
11~20	-.695	-.687	-.683	-.679	-.675	-.671	-.663	-.659	-.655	-.651
21~30	-.643	-.639	-.635	-.631	-.623	-.619	-.615	-.610	-.602	-.598
31~40	-.594	-.590	-.586	-.578	-.574	-.570	-.566	-.558	-.554	-.550
41~50	-.546	-.538	-.534	-.530	-.526	-.522	-.514	-.510	-.506	-.502
51~60	-.494	-.490	-.486	-.482	-.474	-.470	-.466	-.462	-.458	-.450
61~70	-.446	-.442	-.438	-.430	-.426	-.422	-.418	-.410	-.406	-.402
71~80	-.398	-.394	-.386	-.382	-.378	-.374	-.366	-.362	-.357	-.353
81~90	-.345	-.341	-.337	-.333	-.325	-.321	-.317	-.313	-.309	-.301
91~100	-.297	-.293	-.289	-.281	-.277	-.273	-.269	-.261	-.257	-.253

A.2 Clustered Scalp Maps, Alert Baseline Power, Dipole Locations, and Talairach Coordinates of Each Dipole in Each Cluster

A.2.1 The Motionless Datasets

A.2.1.1 The Frontal Cluster

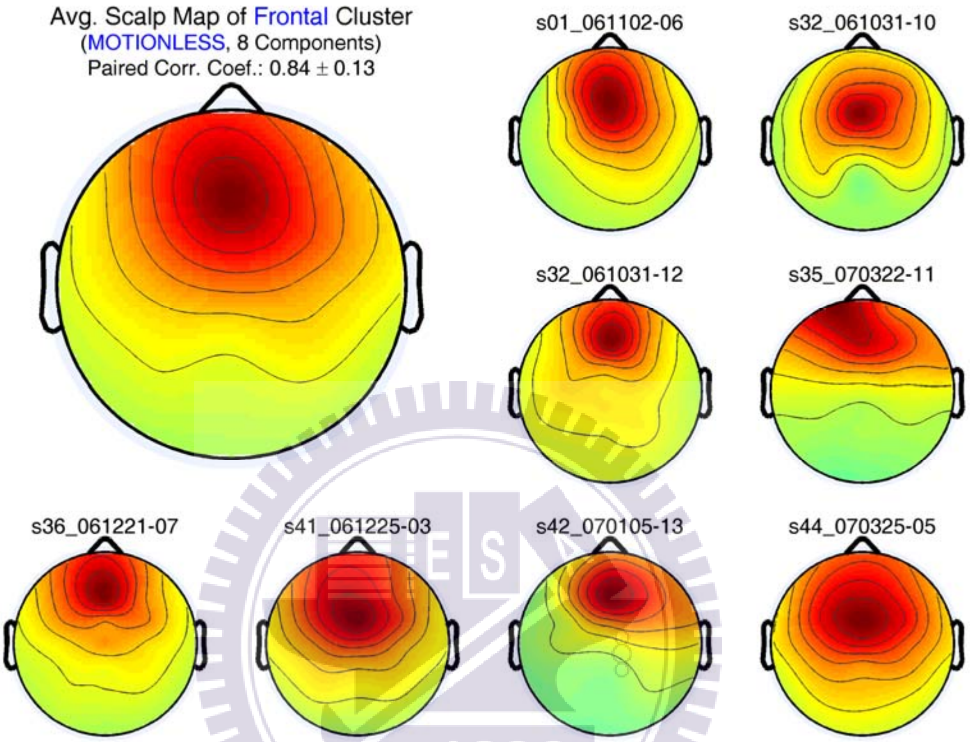

Figure A1: The ICA scalp map of each dataset in the frontal cluster (motionless datasets; 8 components; paired correlation coefficient: 0.84 ± 0.13). The left-top inset is the average scalp map of this cluster, and the others are the scalp map from each dataset in this cluster.

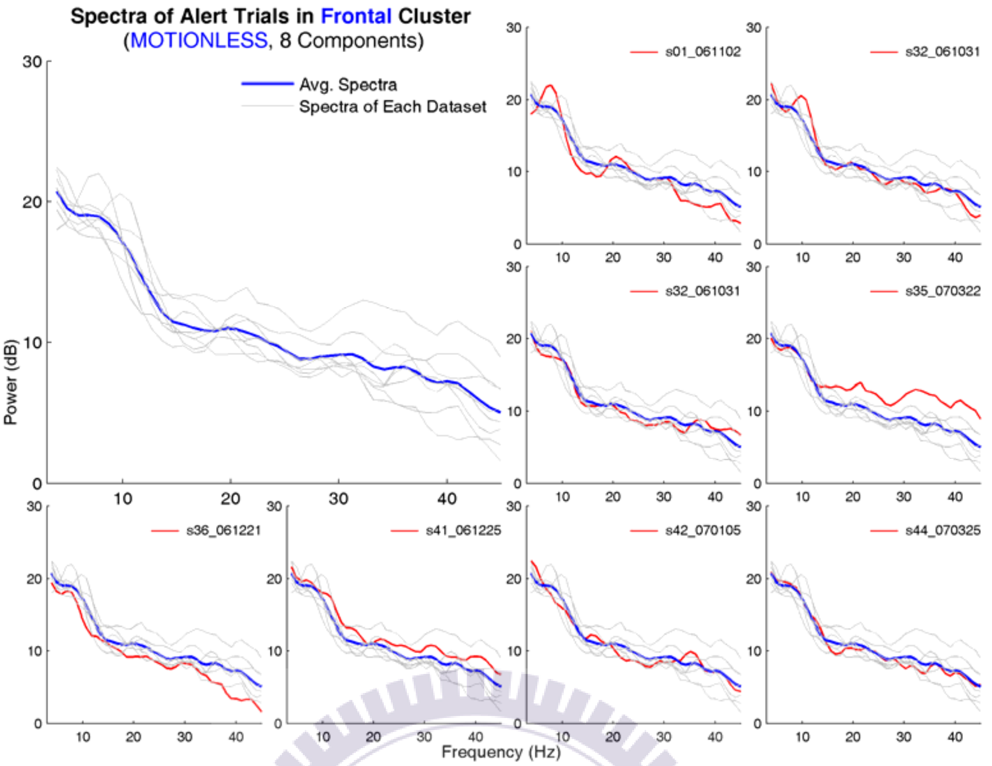

Figure A2: Tonic power spectra of alert trials (trials with shortest 10% RT in each dataset) in the frontal cluster (motionless datasets). The left-top inset is the average spectra of this cluster, and the others are the spectrum of each dataset. In each inset, the blue trace denotes the average spectra of this dataset, the red trace is the average spectrum of the indicated dataset, and the gray traces are the average spectra of the other dataset. The x-axis is frequency in Hz, and the y-axis is the power in dB.

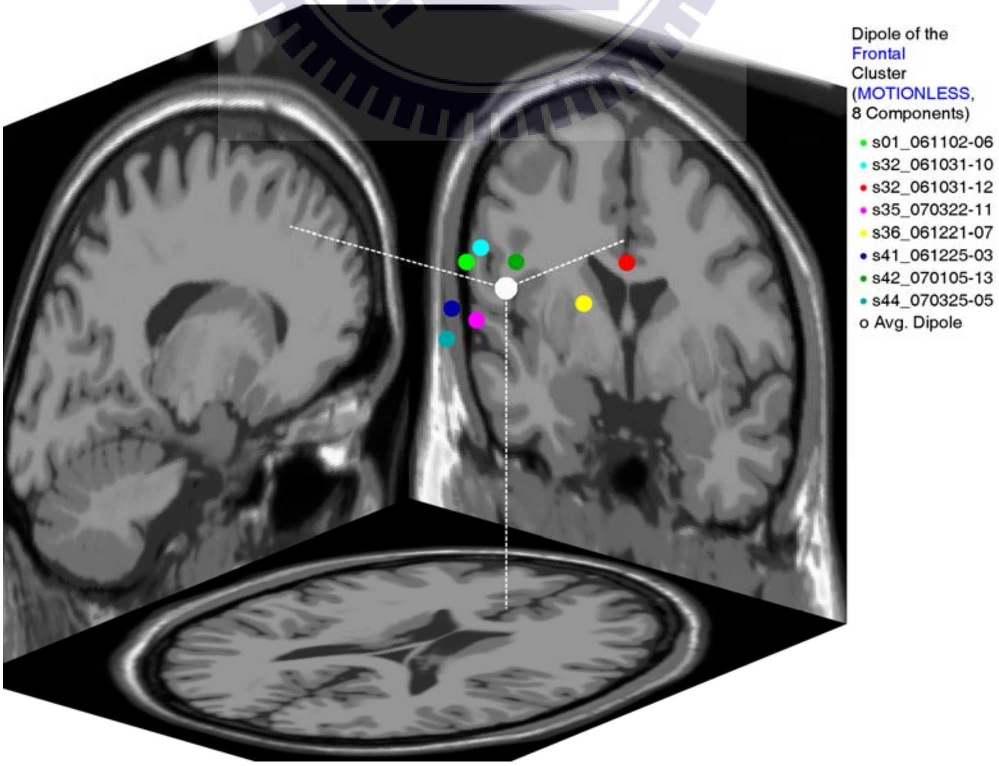

Figure A3: The locations of dipoles in the frontal cluster (motionless datasets). The white dot is the *average location of dipoles in this cluster (dashed line: projection lines to the coronal, horizontal, and sagittal planes), and the others are the location of each dipole in this cluster.*

TABLE A3: TALAIRACH COORDINATES OF THE FRONTAL CLUSTER (MOTIONLESS DATASETS)

Dataset	Component	Talairach Coordinates		
		X	Y	Z
s01_061102	6	-11.63	27.29	38.95
s32_061031	10	4.45	15.79	50.67
s32_061031	12	13.02	74.21	29.23
s35_070322	11	-9.65	28.77	20.48
s36_061221	7	-1.68	70.22	14.38
s41_061225	3	-3.98	10.89	31.10
s42_070105	13	2.47	34.47	39.71
s44_070325	5	-3.38	7.49	22.84
Mean		-1.30	33.64	30.92
Standard Deviation		7.93	25.55	11.85

A.2.1.2 The Central Cluster

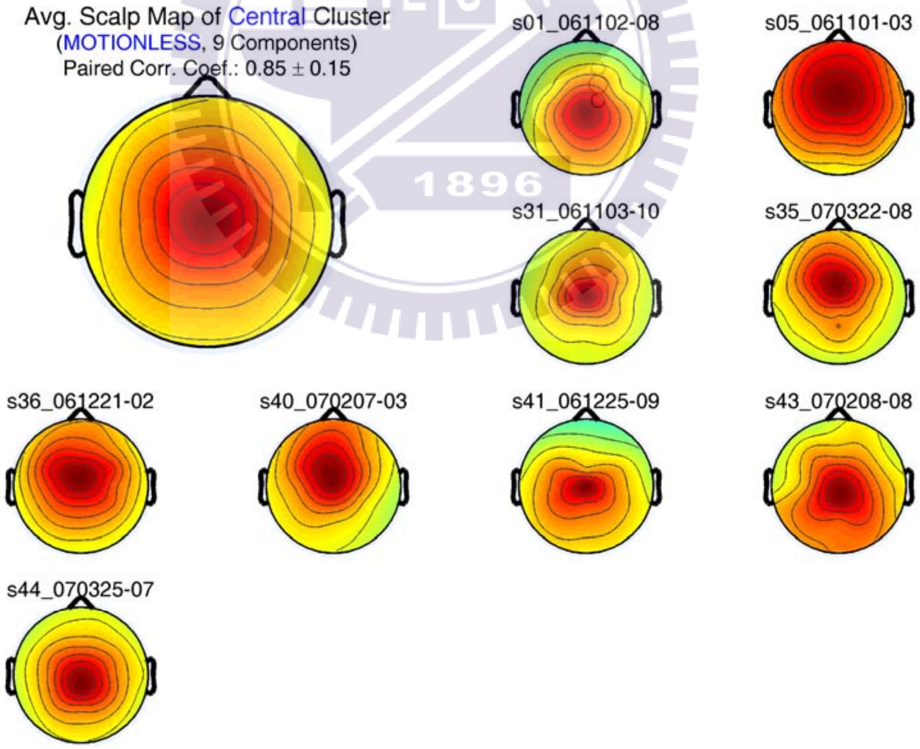

Figure A4: The ICA scalp map of each dataset in the central cluster (motionless datasets; 9 components; paired correlation coefficient: 0.85 ± 0.15). Other conventions follow Figure A1.

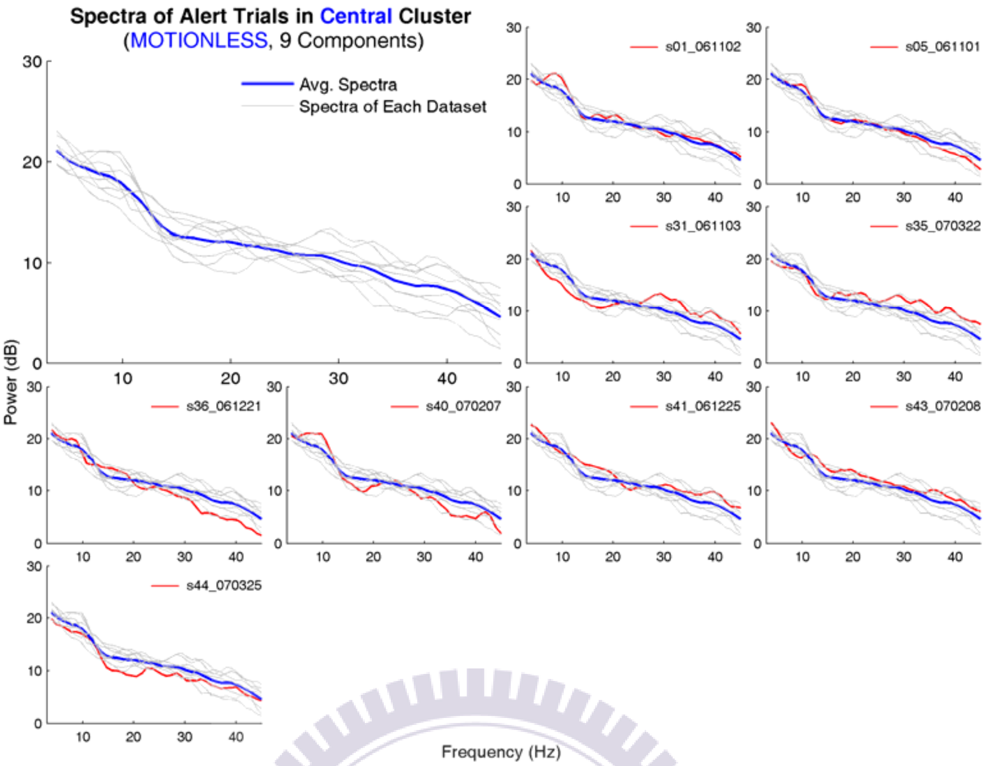

Figure A5: Tonic power spectra of alert trials in the central cluster (motionless datasets). Other conventions follow Figure A2.

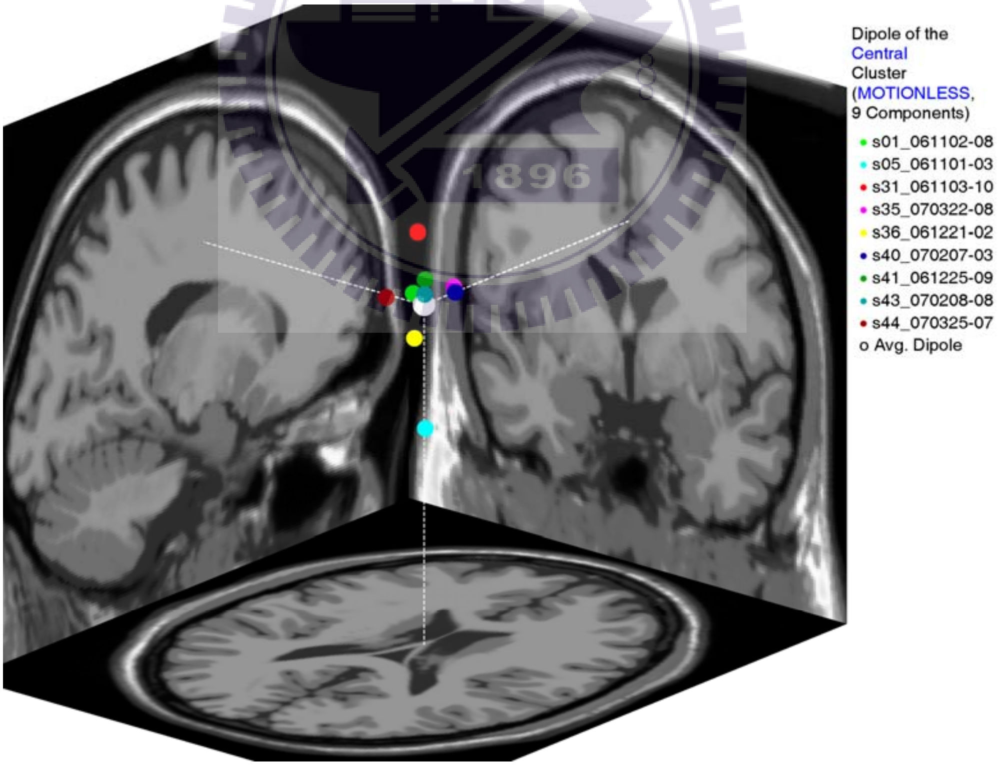

Figure A6: The locations of dipoles in the central cluster (motionless datasets). Other conventions follow Figure A3.

TABLE A4: TALAIRACH COORDINATES OF THE CENTRAL CLUSTER (MOTIONLESS DATASETS)

Dataset	Component	Talairach Coordinates		
		X	Y	Z
s01_061102	8	-3.34	-7.52	42.03
s05_061101	3	3.36	-11.72	2.55
s31_061103	10	1.19	-9.62	62.72
s35_070322	8	0.09	7.70	39.85
s36_061221	2	-3.75	-7.30	27.67
s40_070207	3	8.88	-1.82	43.17
s41_061225	9	-5.60	0.76	43.15
s43_070208	8	2.59	-9.02	43.47
s44_070325	7	-1.29	-22.52	45.94
Mean		0.24	-6.79	38.95
Standard Deviation		4.42	8.49	16.33

A.2.1.3 The Parietal Cluster

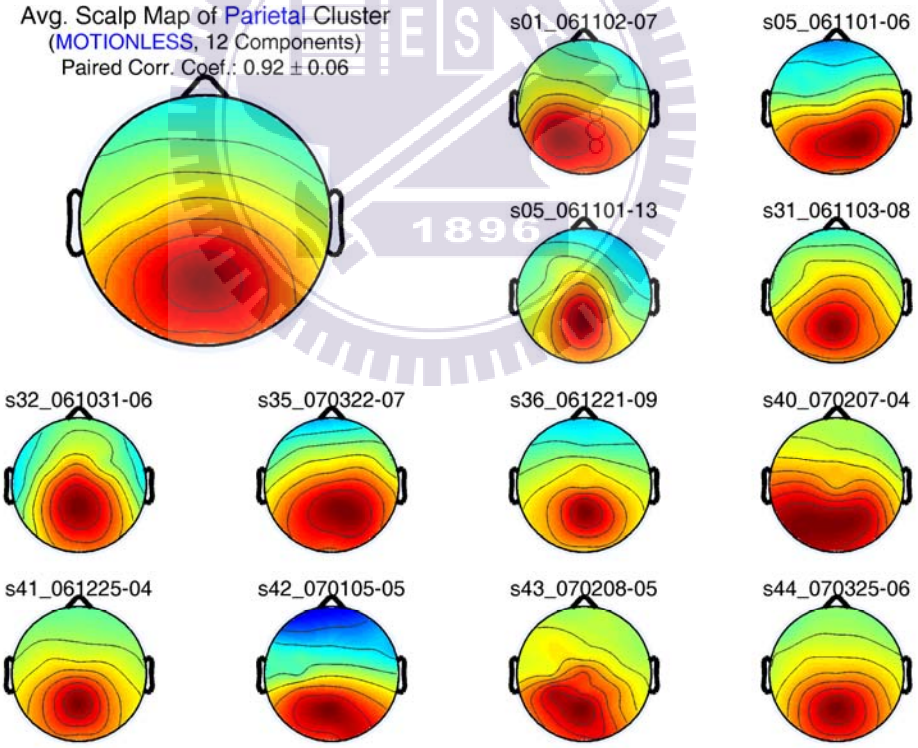

Figure A7: The ICA scalp map of each dataset in the parietal cluster (motionless datasets; 12 components; paired correlation coefficient: 0.92 ± 0.06). Other conventions follow Figure A1.

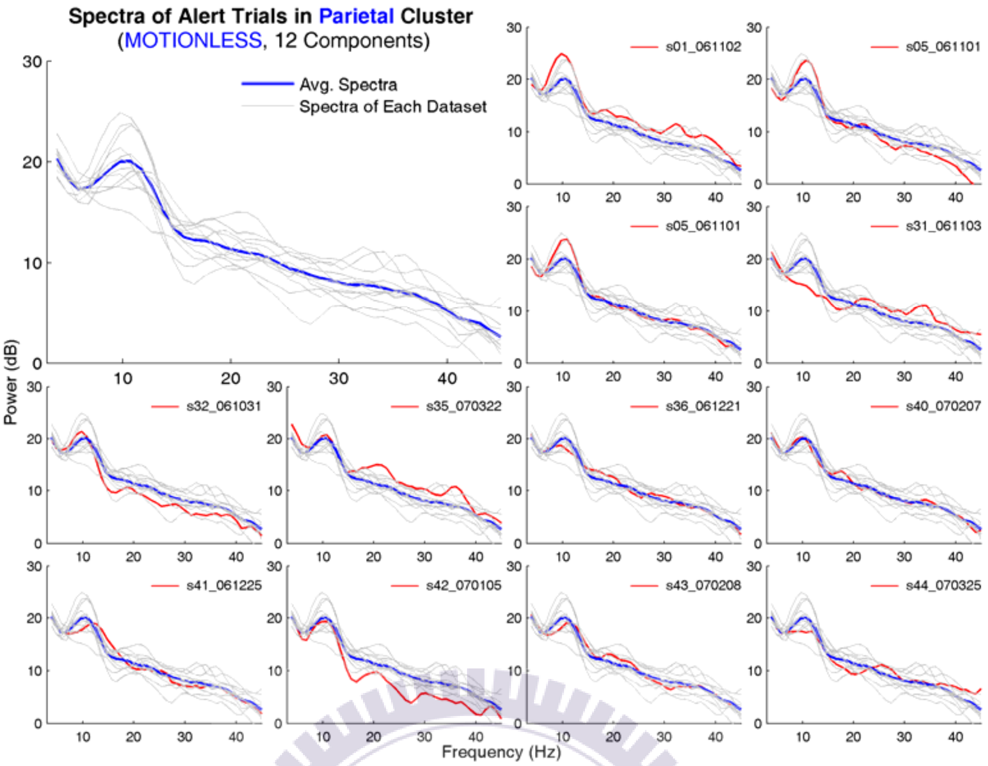

Figure A8: Tonic power spectra of alert trials in the parietal cluster (motionless datasets). Other conventions follow Figure A2.

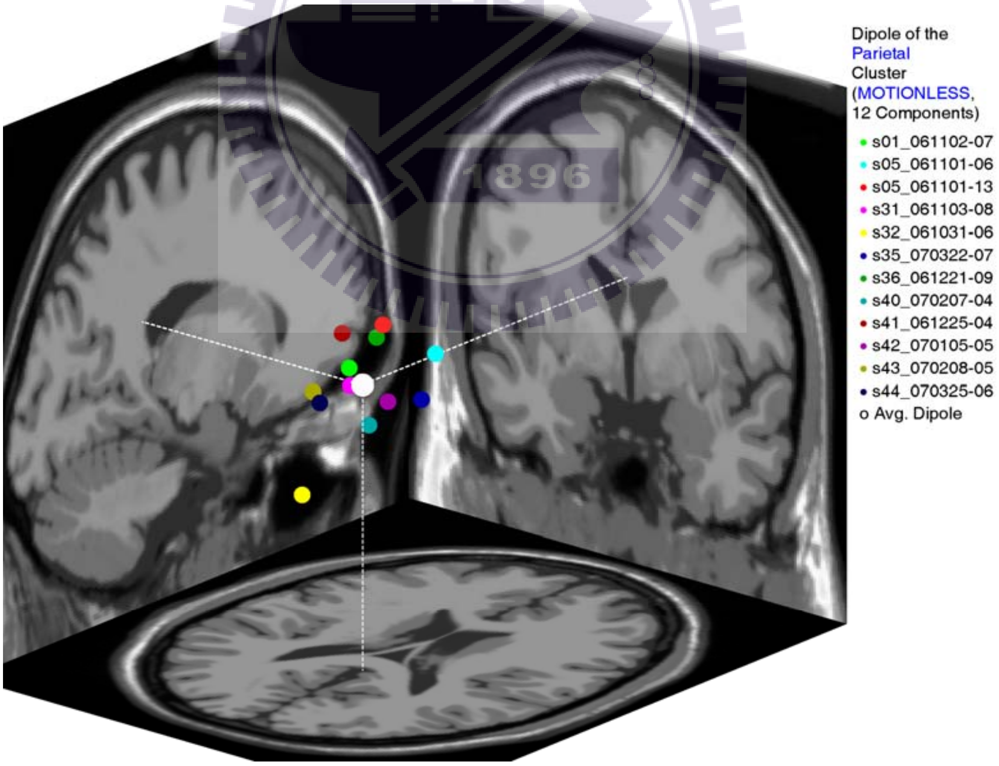

Figure A9: The locations of dipoles in the parietal cluster (motionless datasets). Other conventions follow Figure A3.

Table A5: Talairach Coordinates of the Parietal Cluster (Motionless Datasets)

Dataset	Component	Talairach Coordinates		
		X	Y	Z
s01_061102	7	-9.44	-31.70	24.91
s05_061101	6	9.09	-12.21	27.15
s05_061101	13	9.43	-36.89	44.22
s31_061103	8	-4.35	-37.14	22.28
s32_061031	6	-0.24	-66.16	-1.34
s35_070322	7	5.01	-14.77	12.92
s36_061221	9	4.10	-33.85	38.13
s40_070207	4	0.35	-34.57	10.17
s41_061225	4	-1.84	-43.16	41.15
s42_070105	5	-0.90	-23.94	13.96
s43_070208	5	-4.86	-54.16	25.70
s44_070325	6	-0.87	-55.75	23.71
Mean		0.46	-37.02	23.58
Standard Deviation		5.62	16.12	13.40

A.2.1.4 The Left Somatomotor Cluster

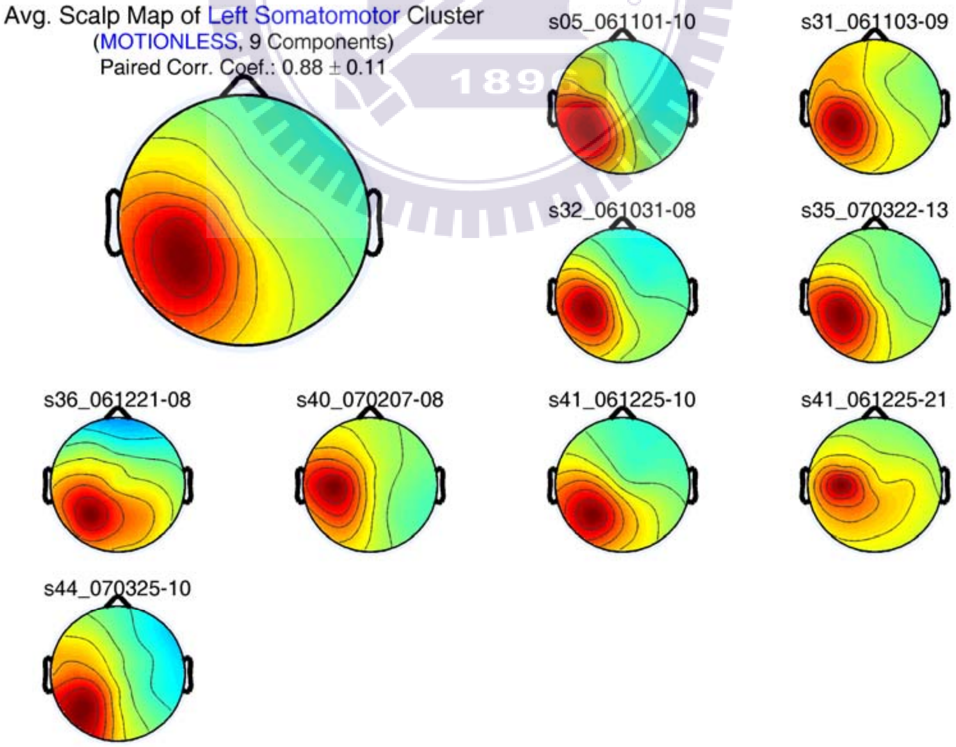

Figure A10: The ICA scalp map of each dataset in the left somatomotor cluster (motionless datasets; 9 components; paired correlation coefficient: 0.88 ± 0.11). Other conventions follow Figure A1.

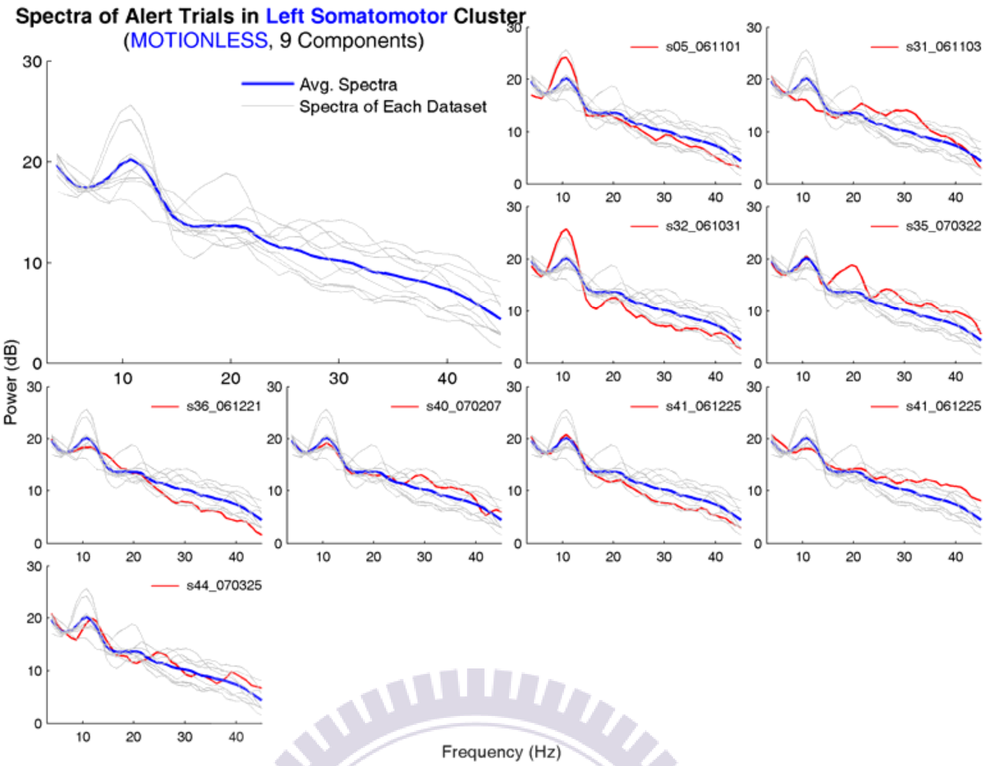

Figure A11: Tonic power spectra of alert trials in the left somatomotor cluster (motionless datasets). Other conventions follow Figure A2.

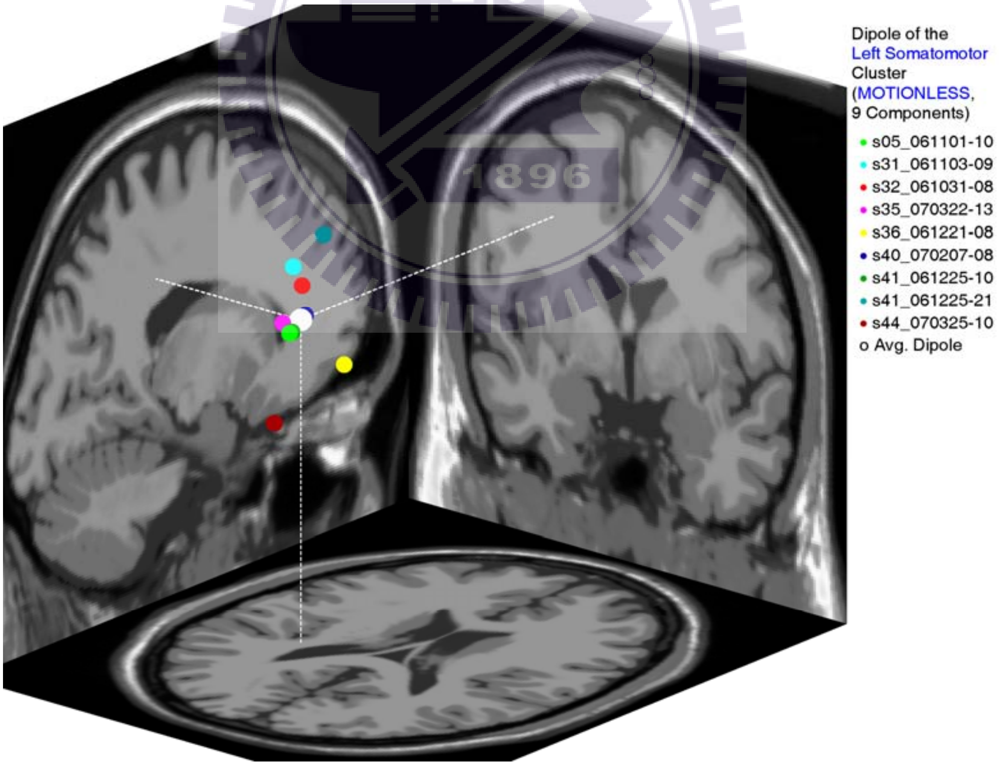

Figure A12: The locations of dipoles in the left somatomotor cluster (motionless datasets). Other conventions follow Figure A3.

Table A6: Talairach Coordinates of the Left Somatomotor Cluster (Motionless Datasets)

Dataset	Component	Talairach Coordinates		
		X	Y	Z
s05_061101	10	-29.64	-36.15	32.70
s31_061103	9	-24.53	-39.12	55.70
s32_061031	8	-38.27	-19.53	40.49
s35_070322	13	-33.57	-34.54	34.53
s36_061221	8	-24.78	-16.61	17.69
s40_070207	8	-31.43	-26.20	34.85
s41_061225	10	-29.35	-35.10	32.85
s41_061225	21	-42.87	-3.45	50.33
s44_070325	10	-18.36	-57.47	14.07
Mean		-30.31	-29.80	34.80
Standard Deviation		7.43	15.53	13.42

A.2.1.5 The Right Somatomotor Cluster

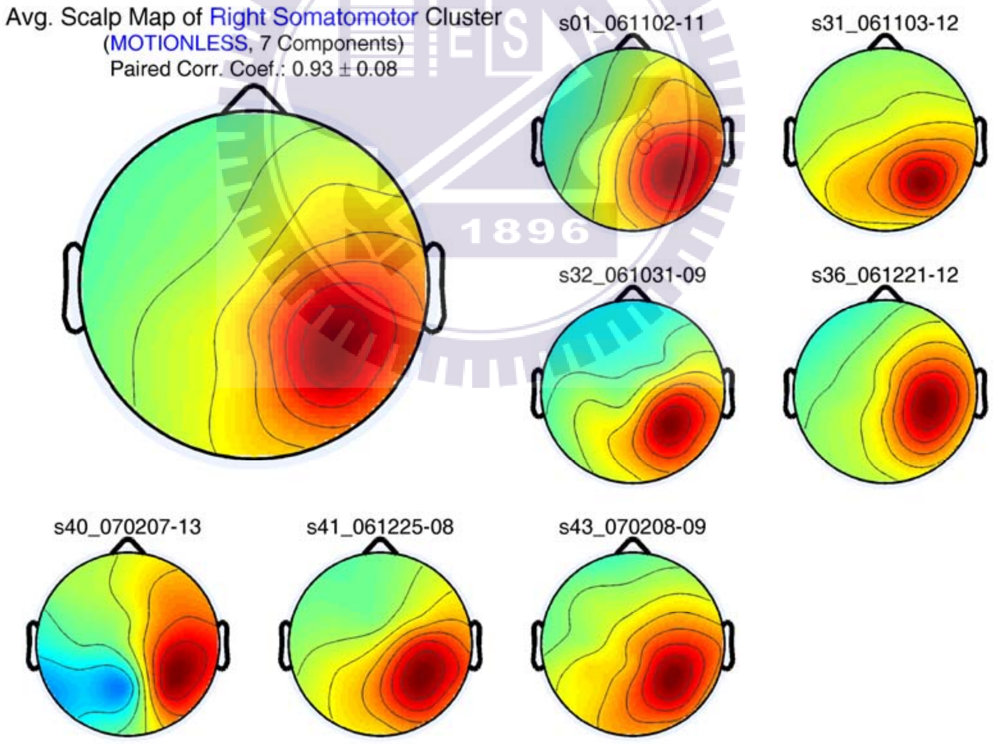

Figure A13: The ICA scalp map of each dataset in the right somatomotor cluster (motionless datasets; 7 components; paired correlation coefficient: 0.93 ± 0.08). Other conventions follow Figure A1.

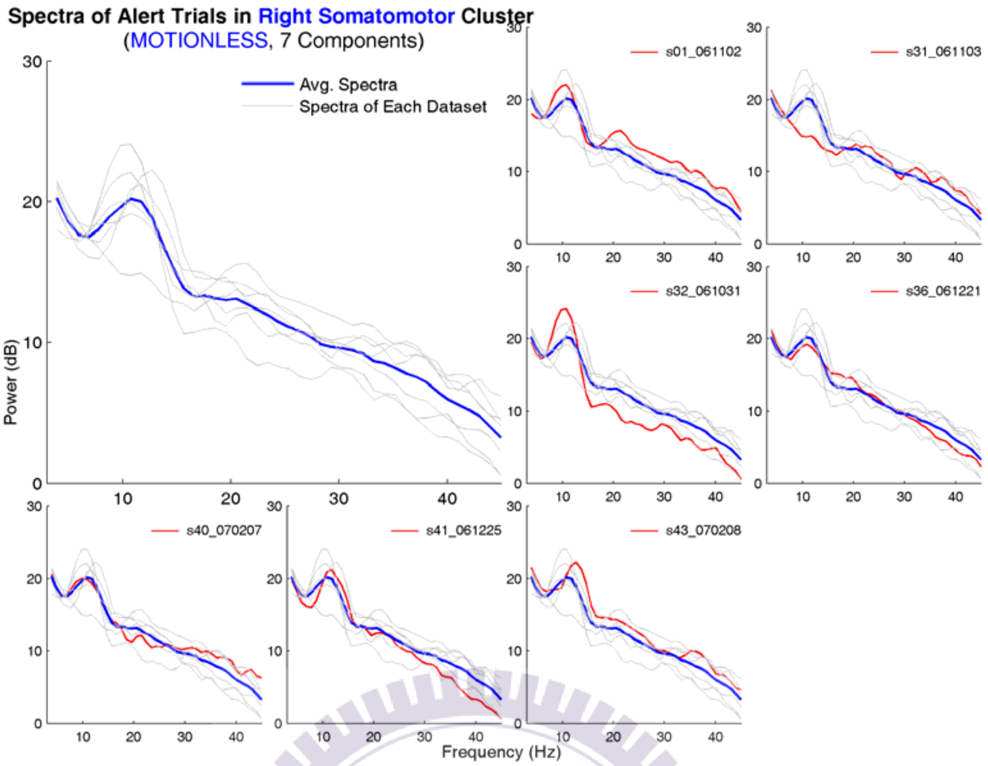

Figure A14: Tonic power spectra of alert trials in the right somatomotor cluster (motionless datasets). Other conventions follow Figure A2.

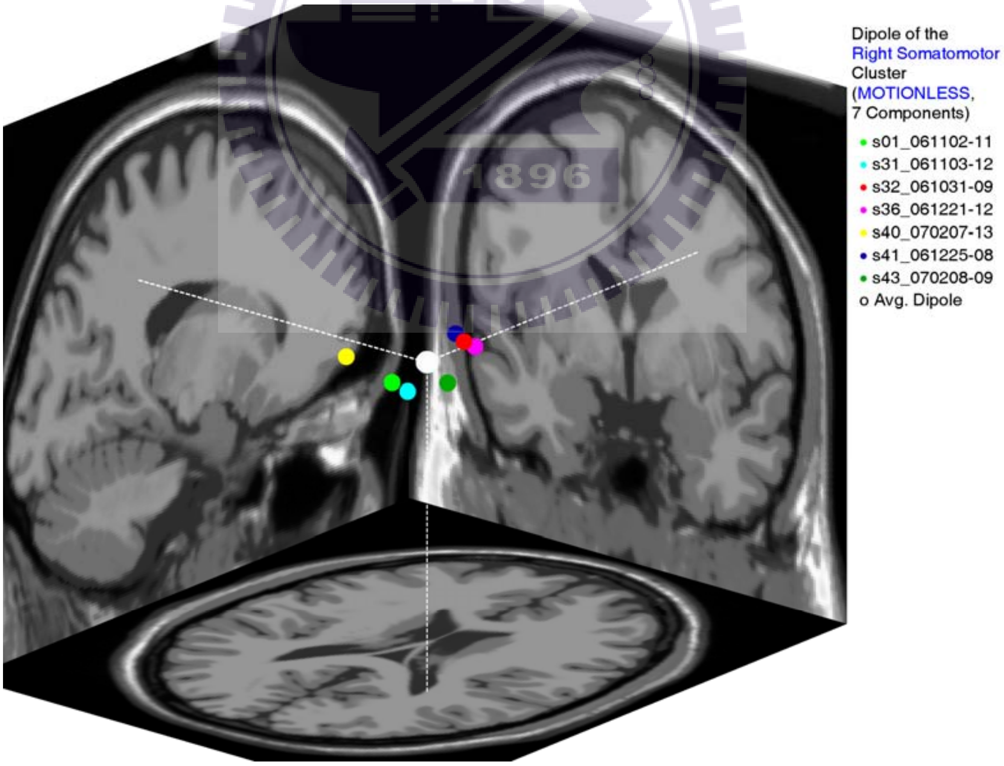

Figure A15: The locations of dipoles in the right somatomotor cluster (motionless datasets). Other conventions follow Figure A3.

Table A7: Talairach Coordinates of the Right Somatomotor Cluster (Motionless Datasets)

Dataset	Component	Talairach Coordinates		
		X	Y	Z
s01_061102	11	15.69	-40.54	28.77
s31_061103	12	33.29	-53.43	34.04
s32_061031	9	34.76	-28.04	41.79
s36_061221	12	33.84	-21.82	37.99
s40_070207	13	18.77	-64.97	45.23
s41_061225	8	30.22	-26.55	42.74
s43_070208	9	30.53	-31.40	28.95
Mean		28.16	-38.11	37.07
Standard Deviation		7.70	15.85	6.66

A.2.1.6 The Occipital Midline Cluster

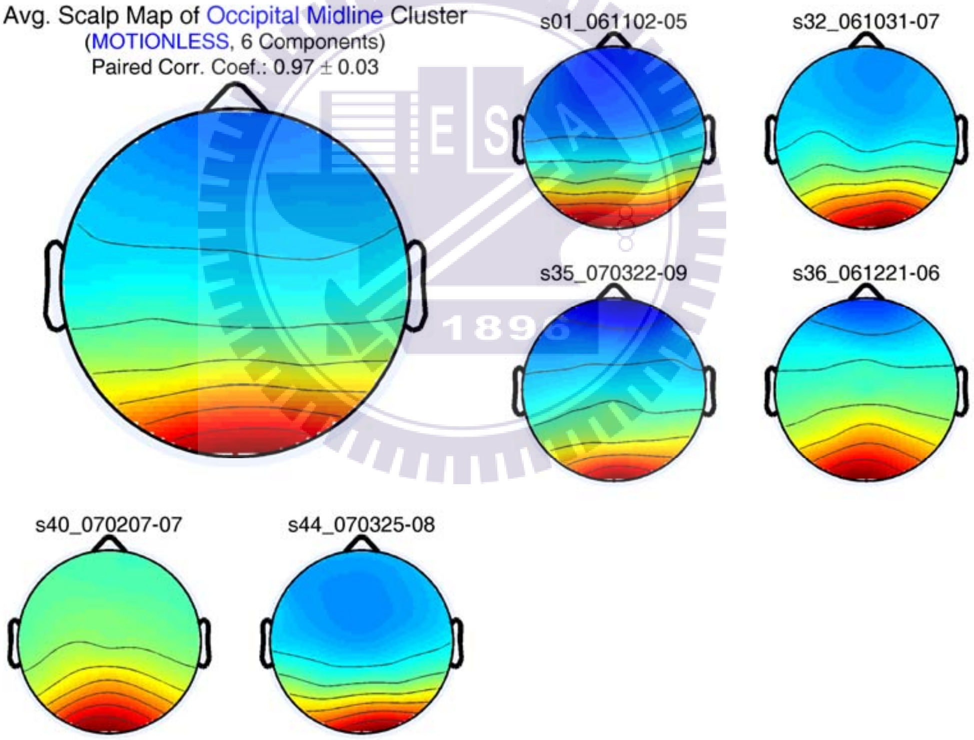

Figure A16: The ICA scalp map of each dataset in the occipital midline cluster (motionless datasets; 6 components; paired correlation coefficient: 0.97 ± 0.03). Other conventions follow Figure A1.

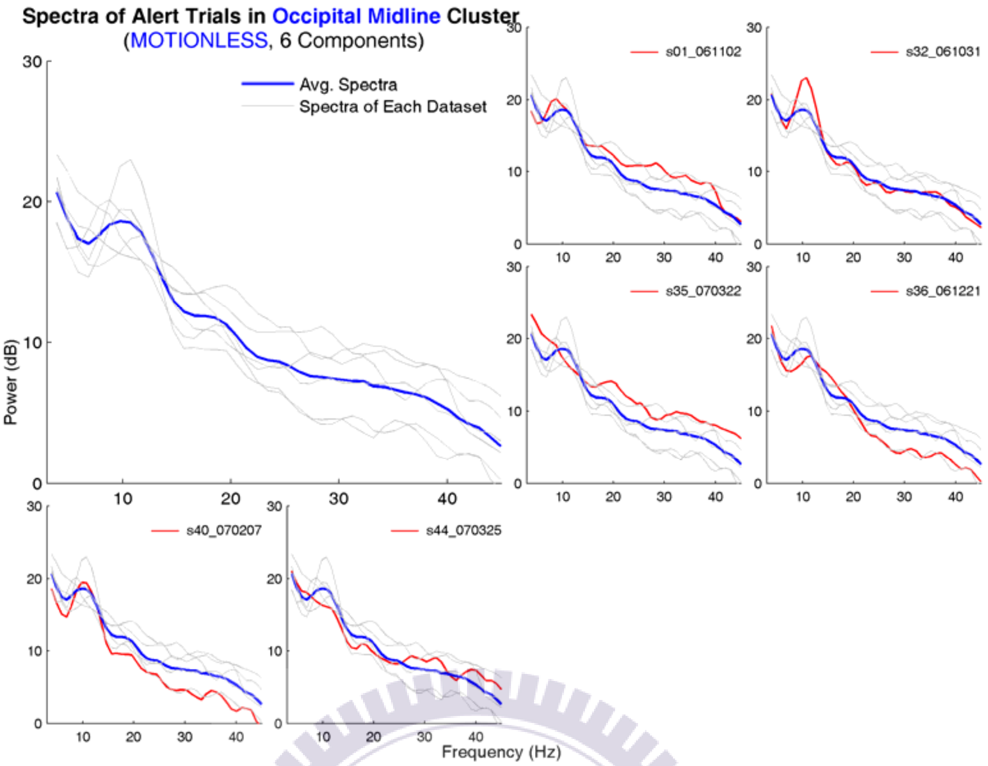

Figure A17: Tonic power spectra of alert trials in the occipital midline cluster (motionless datasets). Other conventions follow Figure A2.

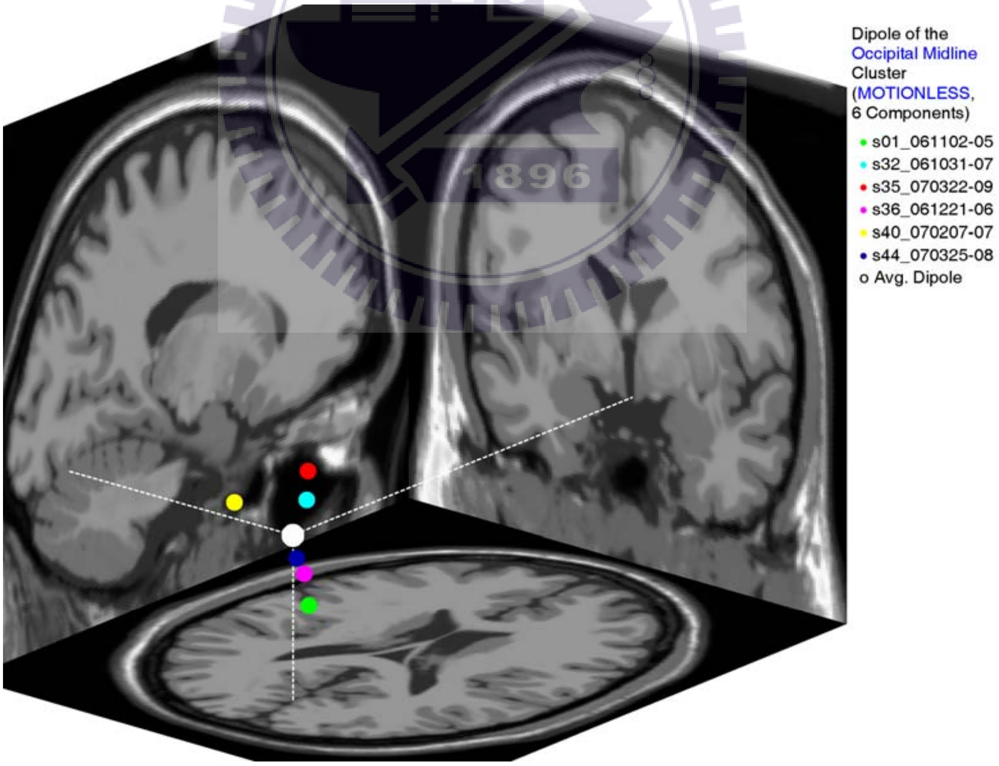

Figure A18: The locations of dipoles in the occipital midline cluster (motionless datasets). Other conventions follow Figure A3.

TABLE A8: TALAIRACH COORDINATES OF THE OCCIPITAL MIDLINE CLUSTER (MOTIONLESS DATASETS)

Dataset	Component	Talairach Coordinates		
		X	Y	Z
s01_061102	5	-1.00	-63.76	-33.74
s32_061031	7	8.47	-74.06	1.25
s35_070322	9	0.15	-63.43	4.86
s36_061221	6	-0.75	-65.71	-23.98
s40_070207	7	-1.36	-96.73	5.34
s44_070325	8	6.07	-76.91	-14.87
Mean		1.93	-73.43	-10.19
Standard Deviation		4.23	12.72	16.52

A.2.1.7 The Bilateral Occipital Cluster

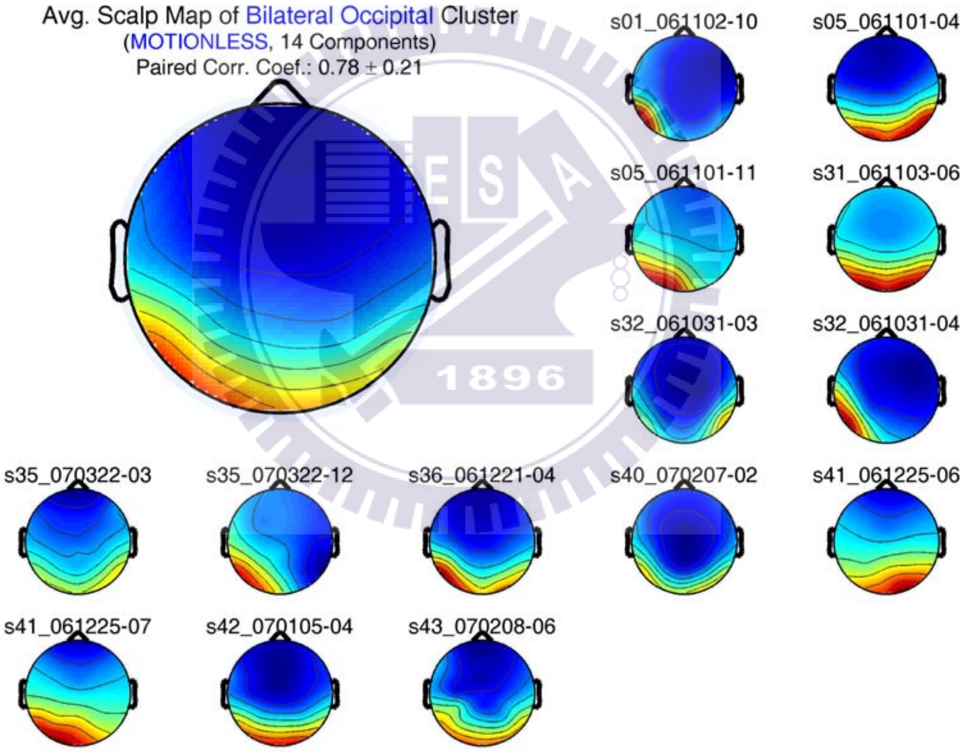

Figure A19: The ICA scalp map of each dataset in the bilateral occipital cluster (motionless datasets; 14 components; paired correlation coefficient: 0.78 ± 0.21). Other conventions follow Figure A1.

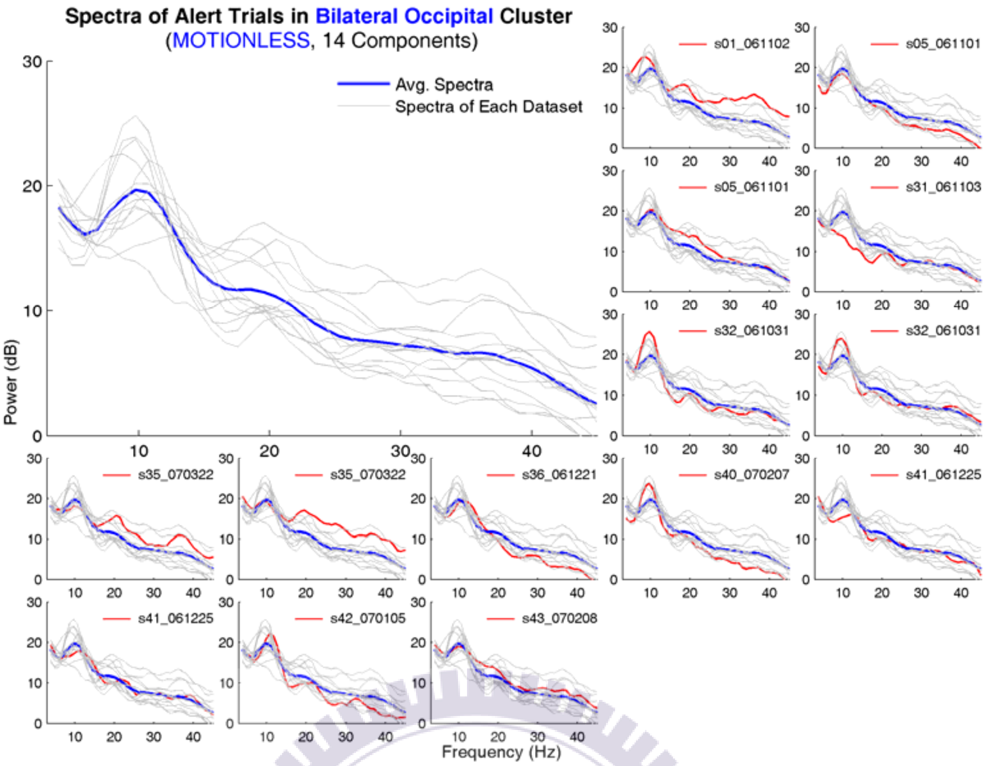

Figure A20: Tonic power spectra of alert trials in the bilateral occipital cluster (motionless datasets). Other conventions follow Figure A2.

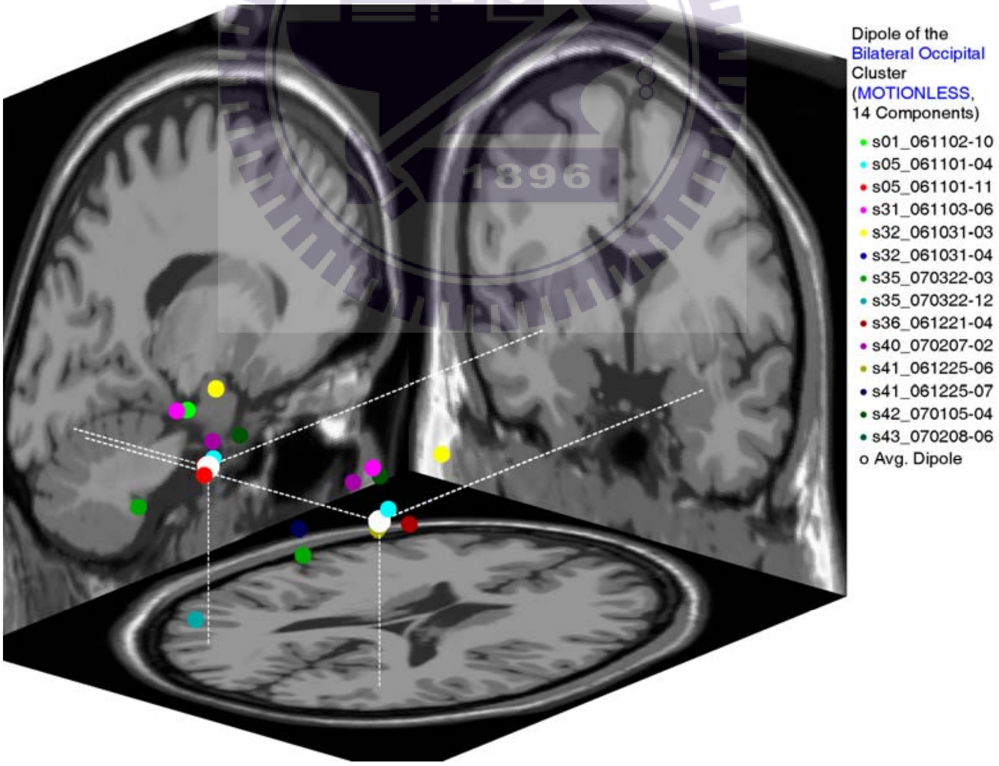

Figure A21: The locations of dipoles in the bilateral occipital cluster (motionless datasets). Other conventions follow Figure A3.

TABLE A9: TALAIRACH COORDINATES OF THE BILATERAL OCCIPITAL CLUSTER (MOTIONLESS DATASETS)

Dataset	Component	Talairach Coordinates (Left)			Talairach Coordinates (Right)		
		X	Y	Z	X	Y	Z
s01_061102	10	-47.34	-65.34	5.46	--	--	--
s05_061101	4	-35.65	-67.11	-5.72	35.91	-67.71	-5.69
s05_061101	11	-29.55	-78.62	-5.93	--	--	--
s31_061103	6	-40.09	-78.56	10.98	40.12	-79.23	11.01
s32_061031	3	-45.96	-53.13	8.53	46.43	-53.90	8.57
s32_061031	4	-44.84	-57.52	-10.92	--	--	--
s35_070322	3	-33.81	-104.96	-8.04	33.42	-105.52	-8.01
s35_070322	12	-20.74	-94.65	-40.58	--	--	--
s36_061221	4	-41.82	-64.36	-9.59	42.13	-65.06	-9.55
s40_070207	2	-28.70	-75.15	2.95	28.80	-75.62	2.97
s41_061225	6	--	--	--	16.78	-50.94	-20.17
s41_061225	7	-18.29	-47.92	-27.97	--	--	--
s42_070105	4	-28.46	-62.56	0.99	28.79	-63.03	1.01
s43_070208	6	--	--	--	4.87	-35.08	-74.53
Mean		-34.60	-70.82	-6.65	30.80	-66.23	-10.49
Standard Deviation		9.70	16.63	15.00	13.08	19.91	25.90

A.2.1.8 The Tangential Occipital Cluster

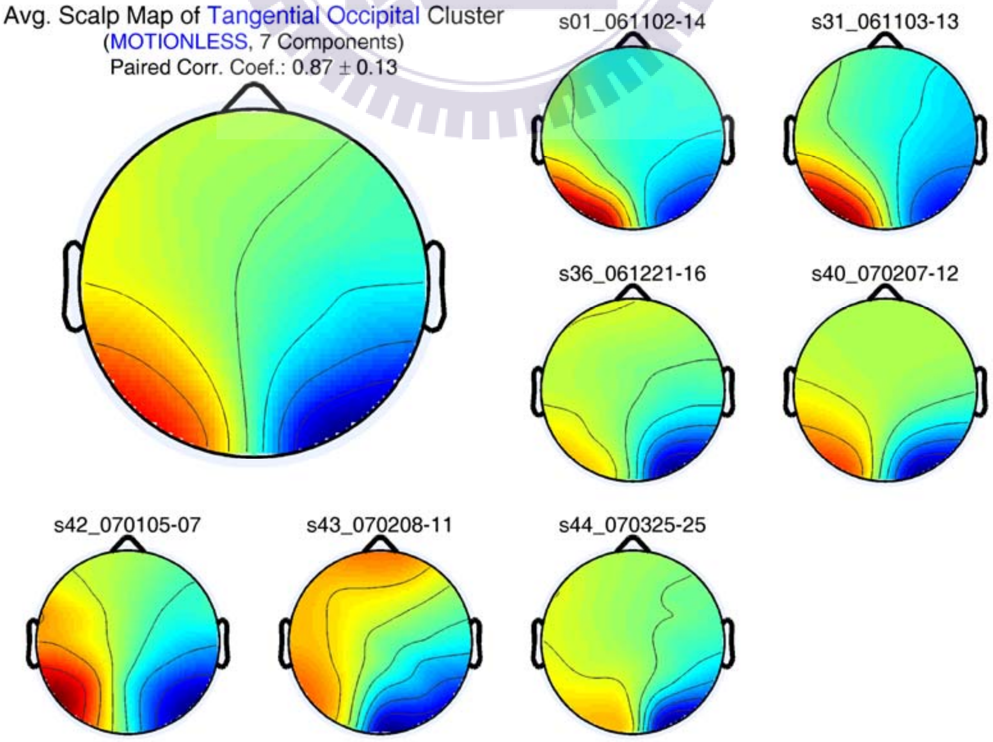

Figure A22: The ICA scalp map of each dataset in the tangential occipital cluster (motionless data-

sets; 7 components; paired correlation coefficient: 0.87 ± 0.13). Other conventions follow Figure A1.

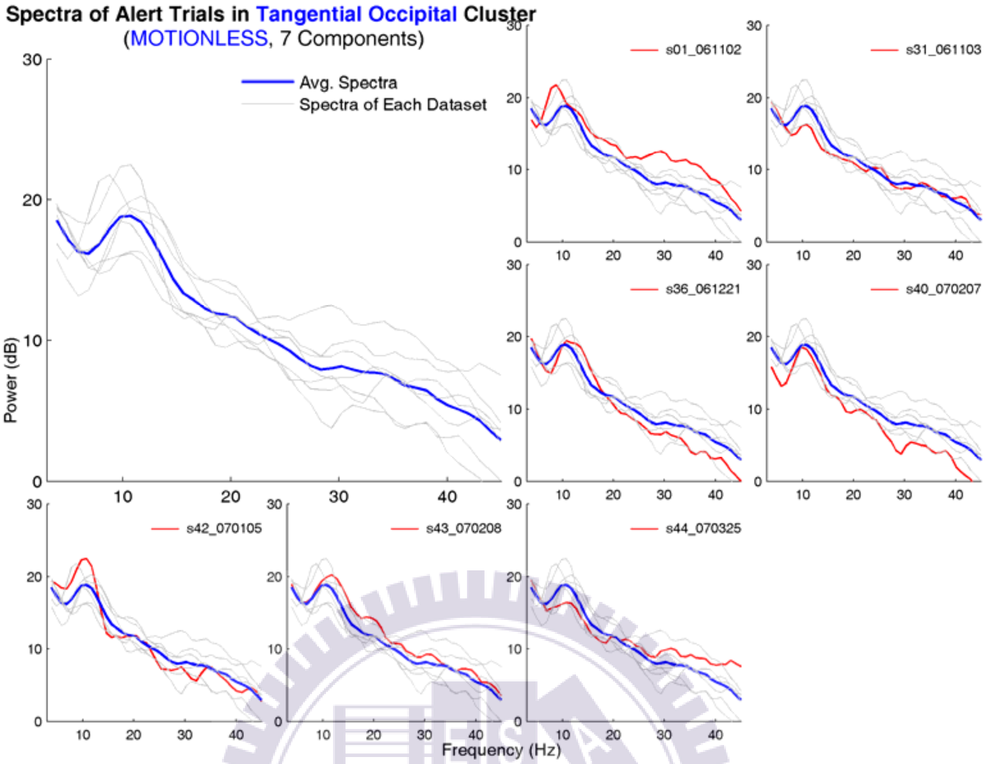

Figure A23: Tonic power spectra of alert trials in the tangential occipital cluster (motionless datasets). Other conventions follow Figure A2.

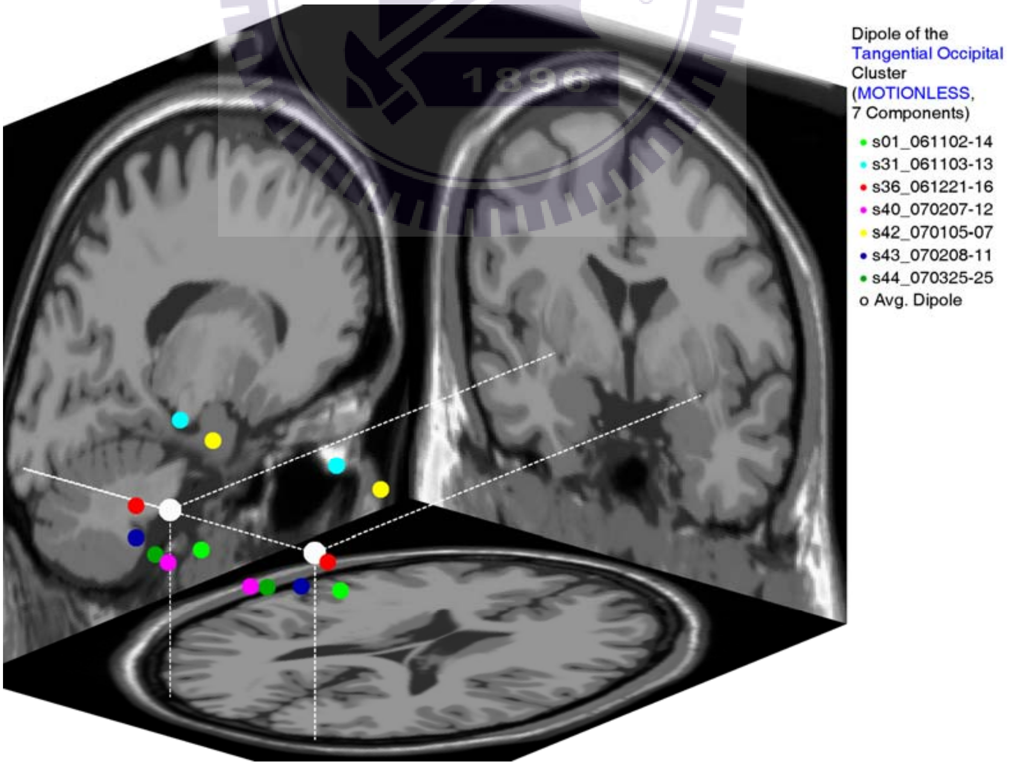

Figure A24: The locations of dipoles in the tangential occipital cluster (motionless datasets). Other conventions follow Figure A3.

TABLE A10: TALAIRACH COORDINATES OF THE TANGENTIAL OCCIPITAL CLUSTER (MO-

TIONLESS DATASETS)

Dataset	Compo-nent	Talairach Coordinates (Left)			Talairach Coordinates (Right)		
		X	Y	Z	X	Y	Z
s01_061102	14	-28.50	-81.91	-18.02	28.52	-82.38	-17.99
s31_061103	13	-32.07	-85.77	20.92	31.96	-86.30	20.95
s36_061221	16	-39.35	-99.34	-2.56	39.05	-99.99	-2.53
s40_070207	12	-17.11	-110.73	-10.77	16.62	-111.01	-10.75
s42_070105	7	-34.28	-68.30	8.45	34.49	-68.87	8.48
s43_070208	11	-34.10	-105.94	-8.65	33.69	-106.51	-8.62
s44_070325	25	-23.17	-109.60	-10.04	22.70	-109.99	-10.02
Mean		-29.80	-94.51	-2.95	29.58	-95.01	-2.93
Standard Deviation		7.55	16.16	13.36	7.67	16.10	13.36

A.2.2 The Motion Datasets

A.2.2.1 The Frontal Cluster

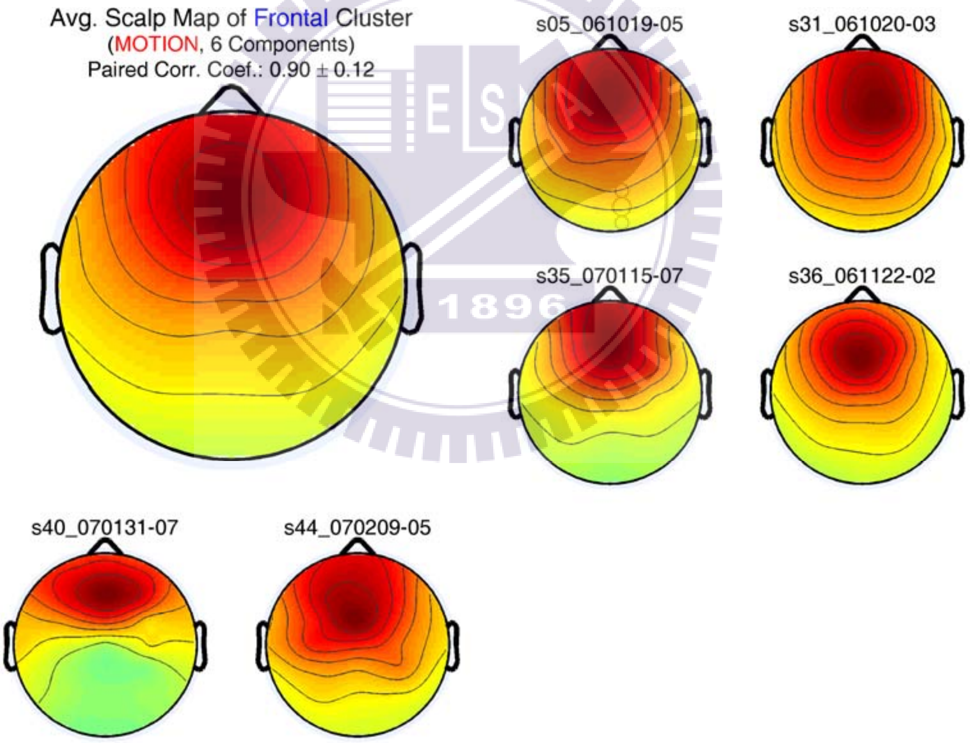

Figure A25: The ICA scalp map of each dataset in the frontal cluster (motion datasets; 6 components; paired correlation coefficient: 0.90 ± 0.12). Other conventions follow Figure A1.

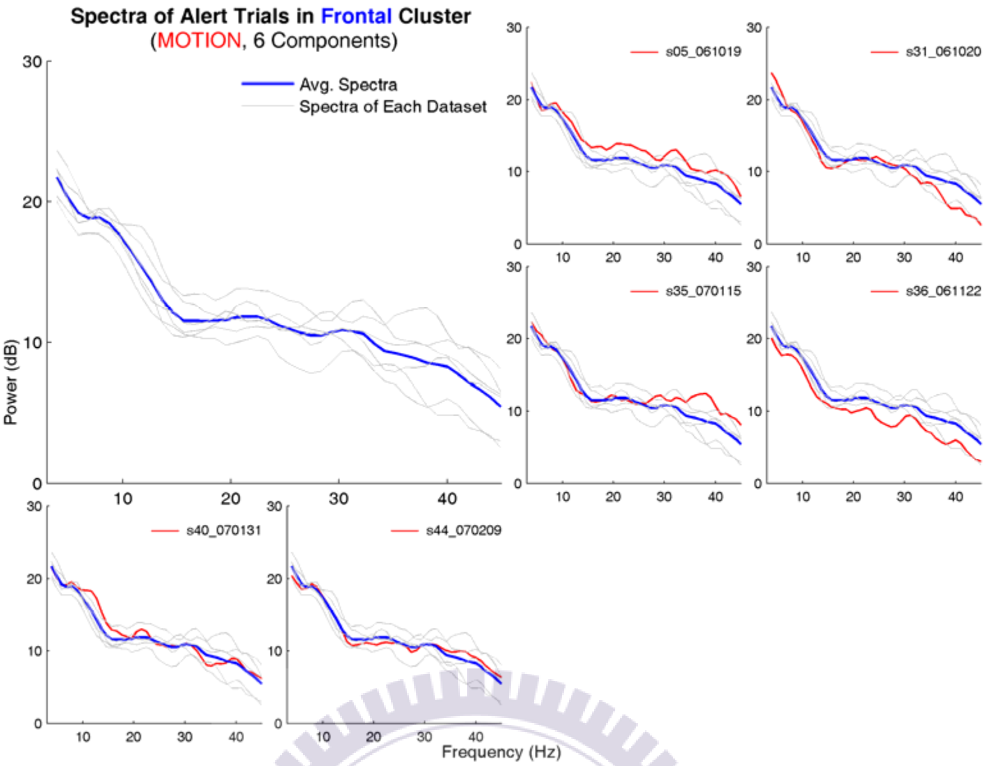

Figure A26: Tonic power spectra of alert trials in the frontal cluster (motion datasets). Other conventions follow Figure A2.

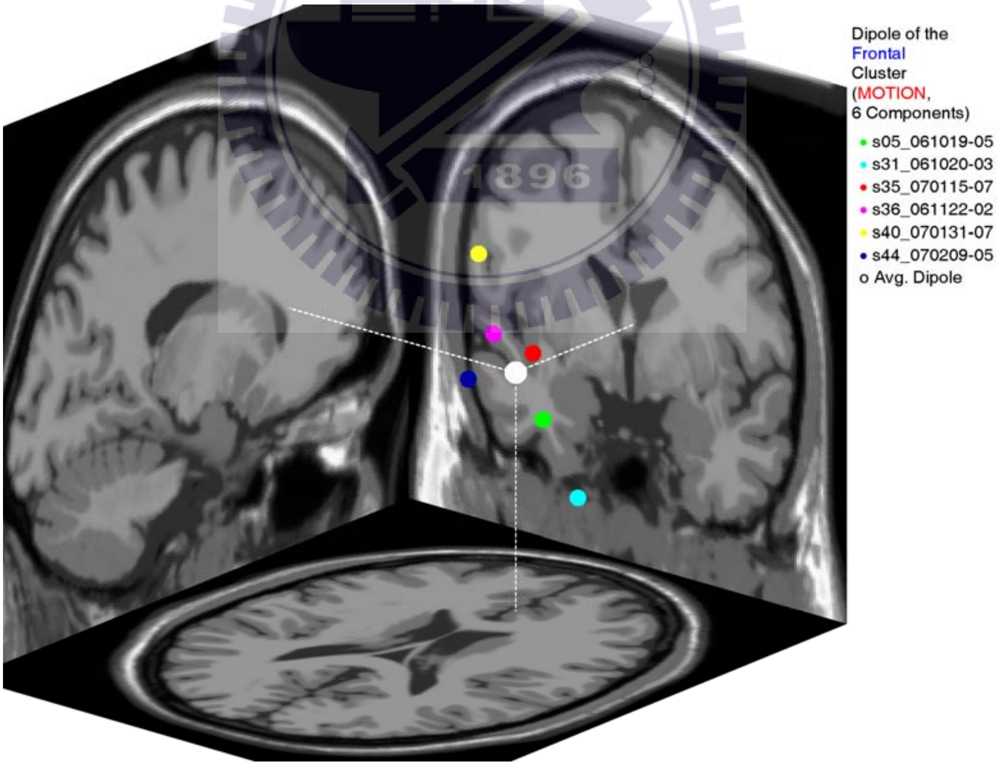

Figure A27: The locations of dipoles in the frontal cluster (motion datasets). Other conventions follow Figure A3.

TABLE A11: TALAIRACH COORDINATES OF THE FRONTAL CLUSTER (MOTION DATASETS)

Dataset	Component	Talairach Coordinates		
		X	Y	Z
s05_061019	5	2.98	44.05	-11.69
s31_061020	3	13.27	47.49	-32.96
s35_070115	7	0.41	43.28	7.74
s36_061122	2	-1.16	26.86	18.83
s40_070131	7	2.29	17.33	47.75
s44_070209	5	-1.50	14.67	8.43
Mean		2.71	32.28	6.35
Standard Deviation		5.47	14.52	27.38

A.2.2.2 The Central Cluster

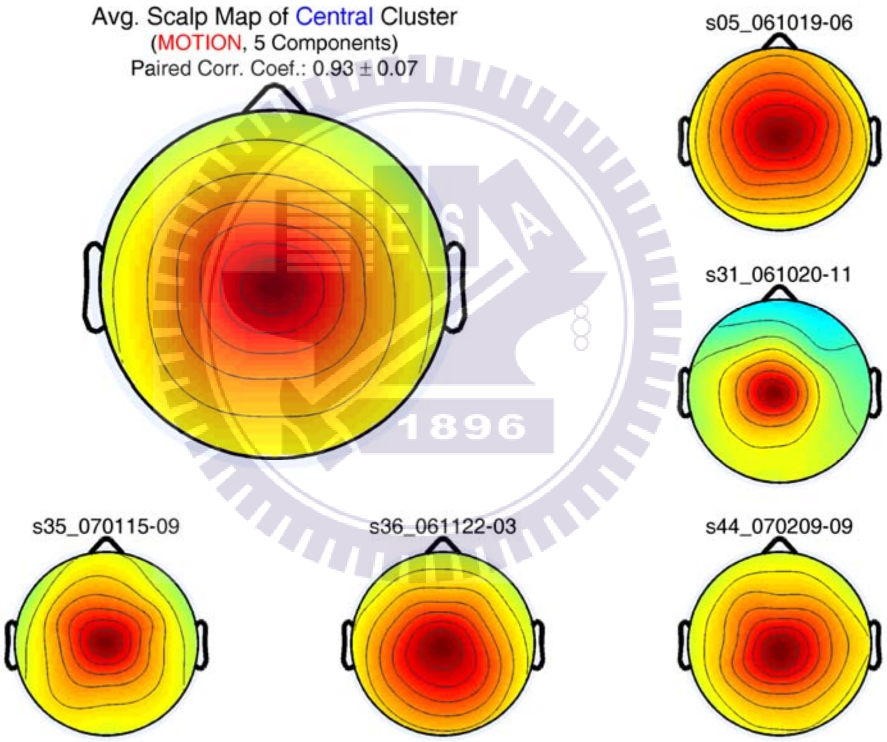

Figure A28: The ICA scalp map of each dataset in the central cluster (motion datasets; 5 components; paired correlation coefficient: 0.93 ± 0.07). Other conventions follow Figure A1.

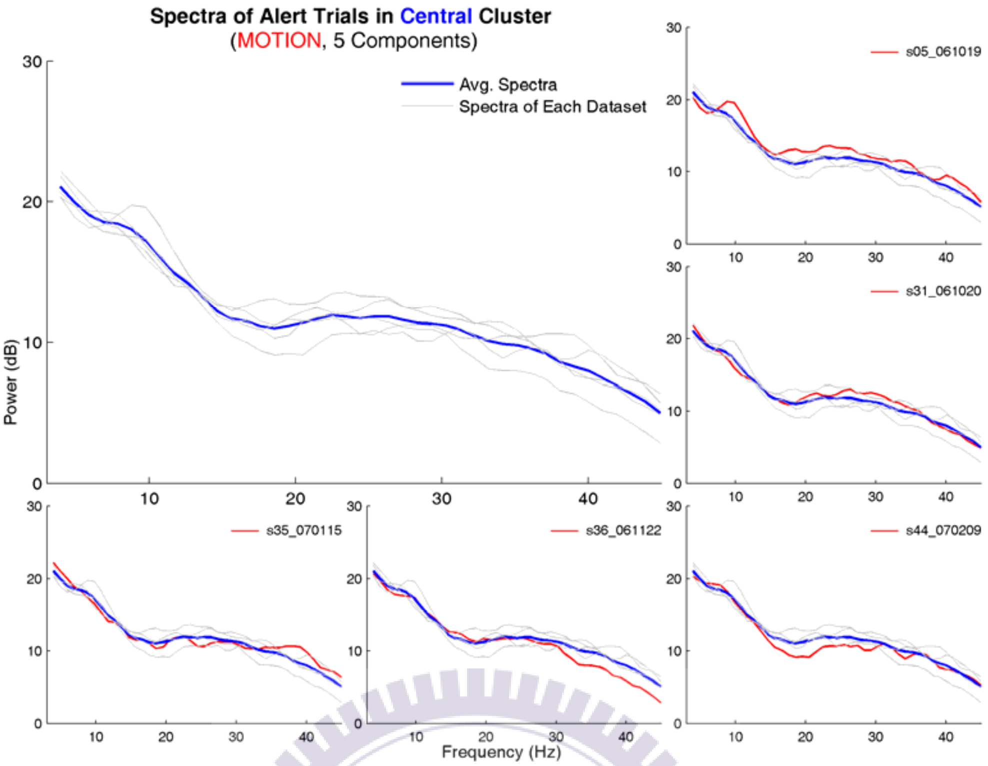

Figure A29: Tonic power spectra of alert trials in the central cluster (motion datasets). Other conventions follow Figure A2.

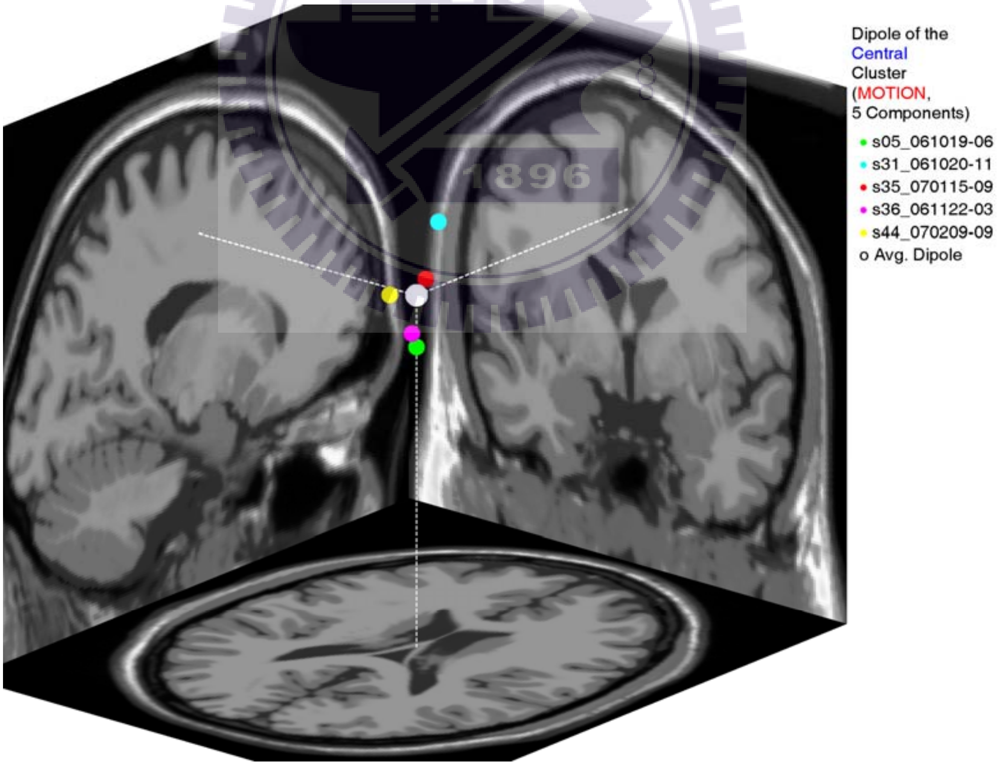

Figure A30: The locations of dipoles in the central cluster (motion datasets). Other conventions follow Figure A3.

TABLE A12: TALAIRACH COORDINATES OF THE CENTRAL CLUSTER (MOTION DATASETS)

Dataset	Component	Talairach Coordinates		
		X	Y	Z
s05_061019	6	0.59	-11.30	27.11
s31_061020	11	-3.02	4.88	60.35
s35_070115	9	-0.03	-5.28	46.55
s36_061122	3	2.63	-15.61	33.14
s44_070209	9	-0.56	-21.74	46.65
Mean		-0.08	-9.81	42.76
Standard Deviation		2.04	10.18	13.01

A.2.2.3 The Parietal Cluster

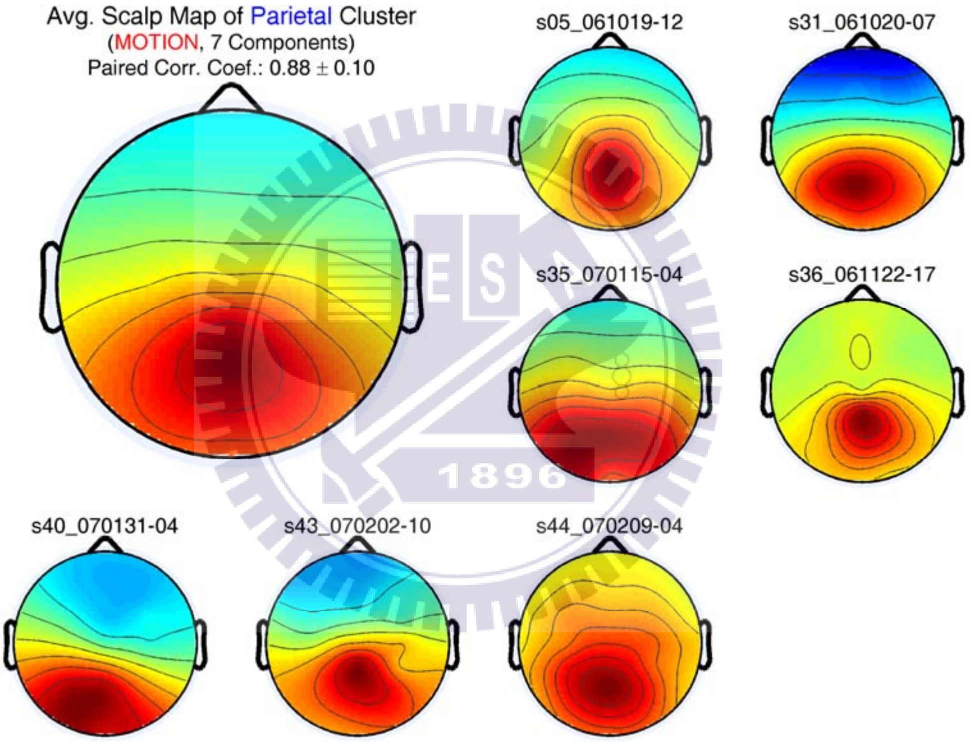

Figure A31: The ICA scalp map of each dataset in the parietal cluster (motion datasets; 7 components; paired correlation coefficient: 0.88 ± 0.10). Other conventions follow Figure A1.

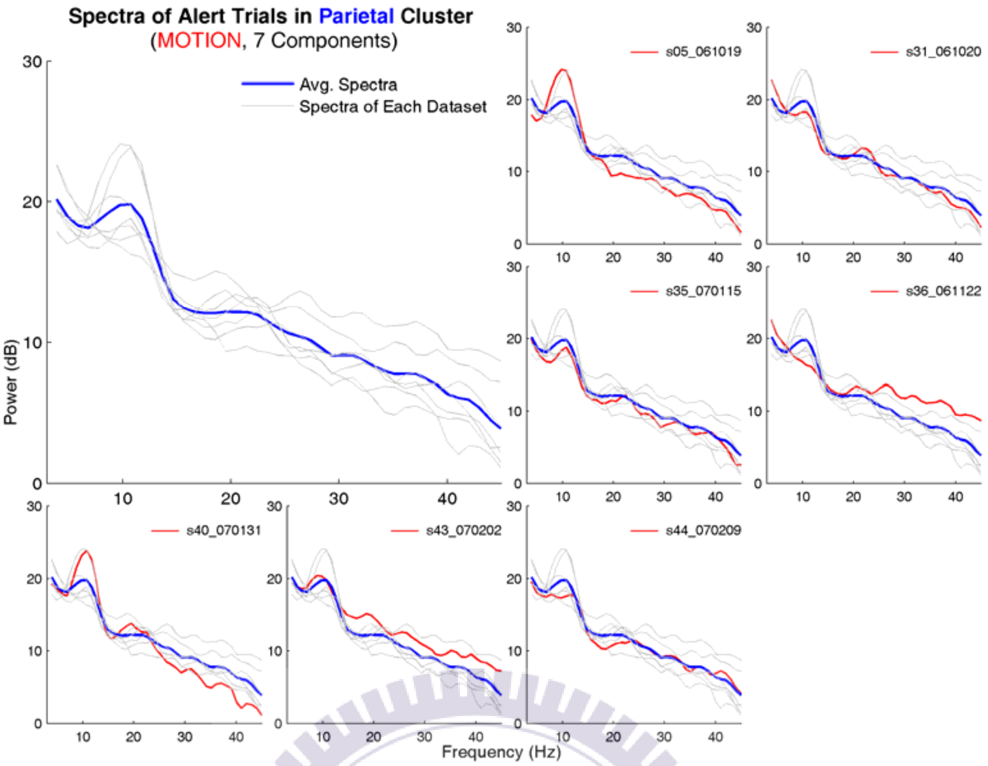

Figure A32: Tonic power spectra of alert trials in the parietal cluster (motion datasets). Other conventions follow Figure A2.

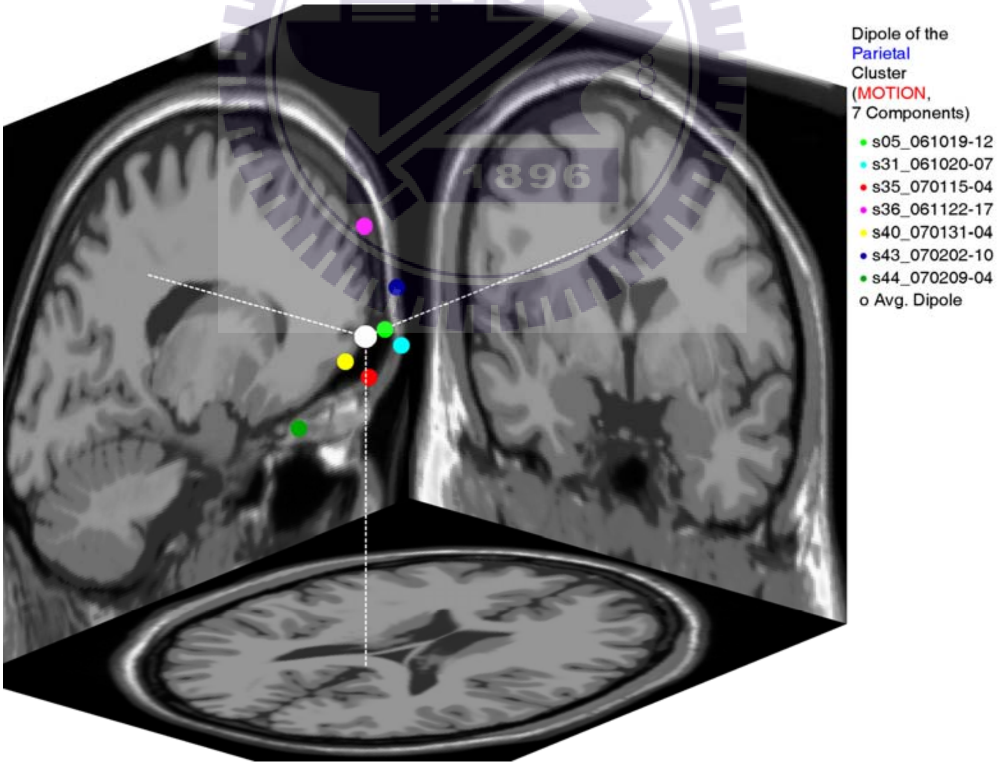

Figure A33: The locations of dipoles in the parietal cluster (motion datasets). Other conventions follow Figure A3.

TABLE A13: TALAIRACH COORDINATES OF THE PARIETAL CLUSTER (MOTION DATASETS)

Dataset	Component	Talairach Coordinates		
		X	Y	Z
s05_061019	12	5.65	-31.51	40.21
s31_061020	7	-2.32	-15.16	28.21
s35_070115	4	-7.64	-24.59	20.07
s36_061122	17	15.63	-51.02	80.97
s40_070131	4	-4.53	-39.05	30.31
s43_070202	10	-4.50	-13.92	45.61
s44_070209	4	-4.16	-62.21	16.98
Mean		-0.27	-33.92	37.48
Standard Deviation		8.14	18.09	21.70

A.2.2.4 The Left Somatormotor Cluster

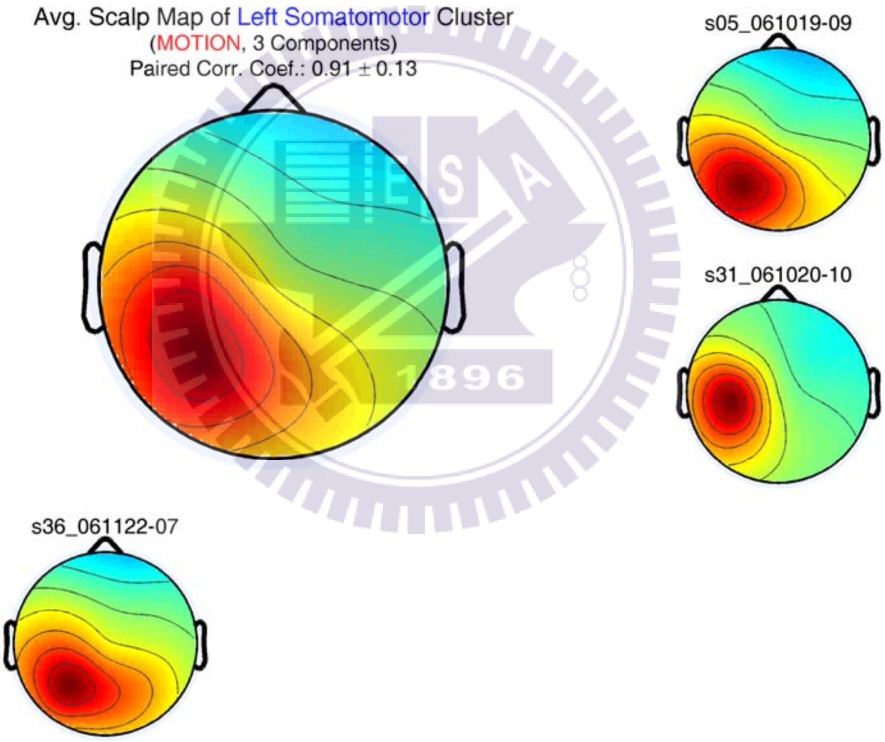

Figure A34: The ICA scalp map of each dataset in the left somatomotor cluster (motion datasets; 3 components; paired correlation coefficient: 0.91 ± 0.13). Other conventions follow Figure A1.

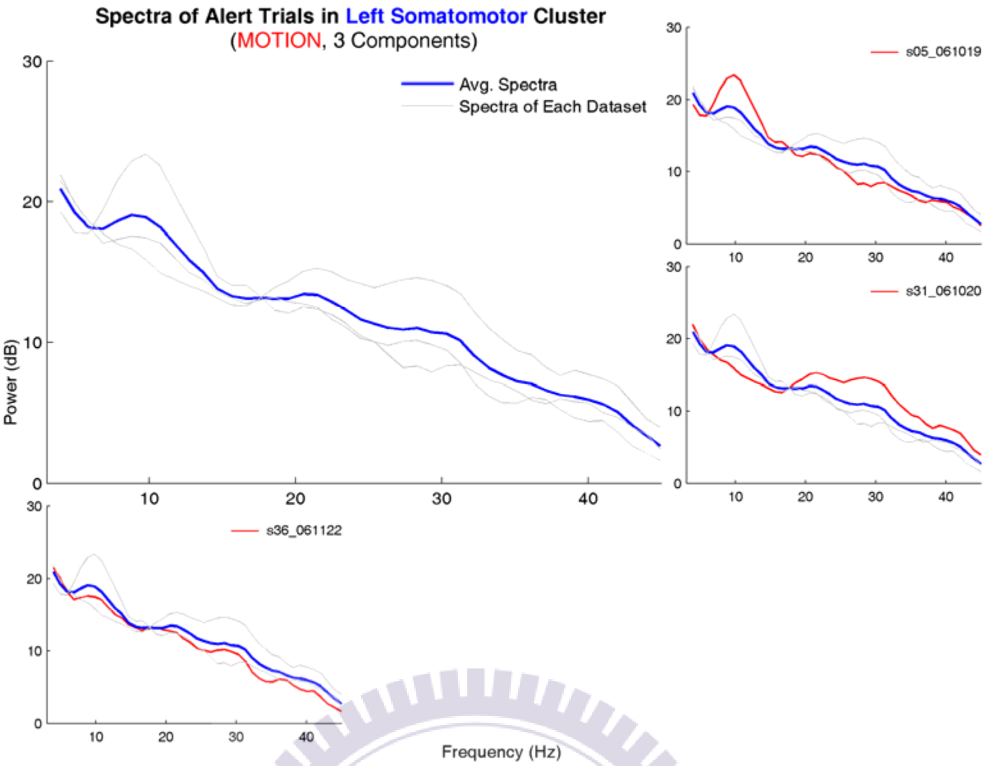

Figure A35: Tonic power spectra of alert trials in the left somatomotor cluster (motion datasets). Other conventions follow Figure A2.

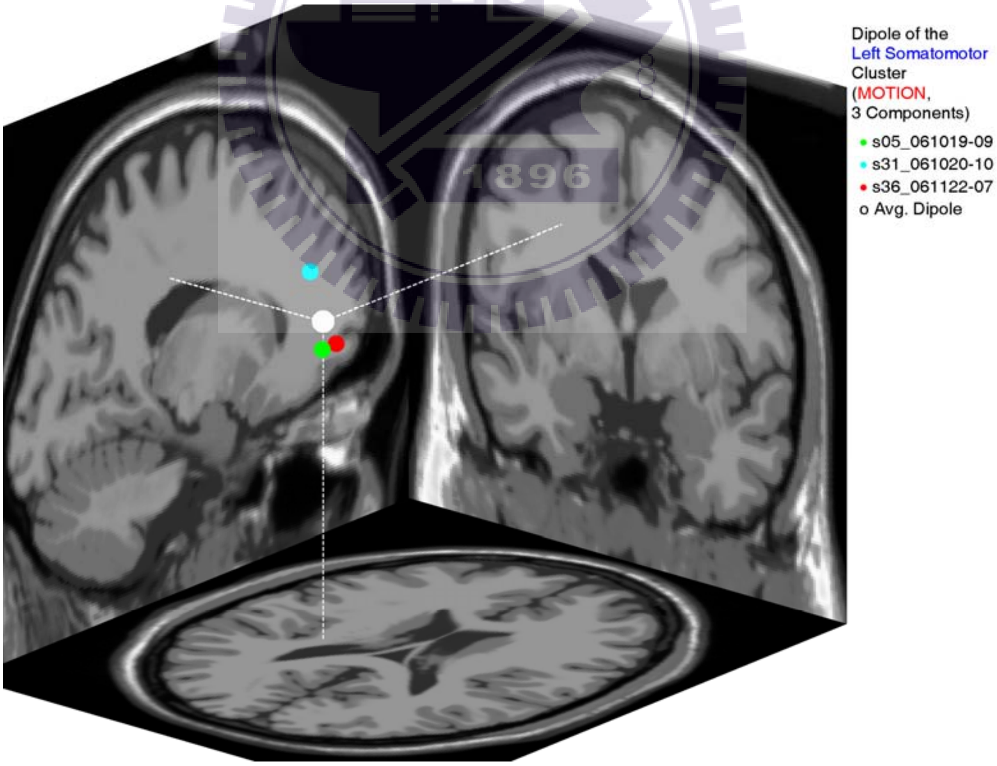

Figure A36: The locations of dipoles in the left somatomotor cluster (motion datasets). Other conventions follow Figure A3.

TABLE A14: TALAIRACH COORDINATES OF THE LEFT SOMATOMOTOR CLUSTER (MOTION DATASETS)

Dataset	Component	Talairach Coordinates		
		X	Y	Z
s05_061019	9	-22.08	-29.63	27.18
s31_061020	10	-36.26	-17.89	44.73
s36_061122	7	-22.78	-22.12	26.52
Mean		-27.04	-23.21	32.81
Standard Deviation		7.99	5.94	10.33

A.2.2.5 The Right Somatomotor Cluster

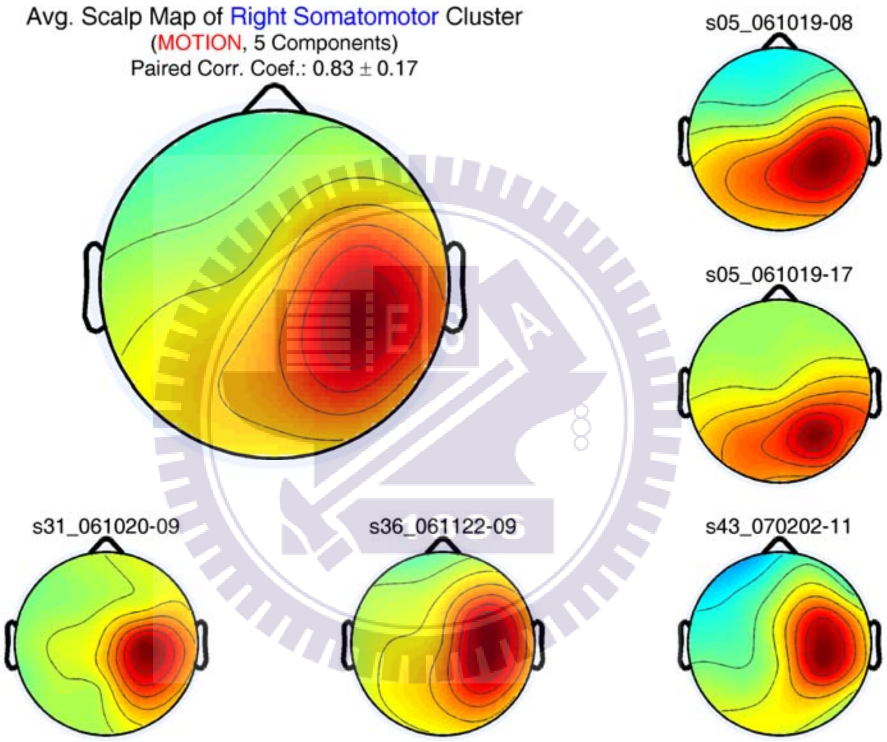

Figure A37: The ICA scalp map of each dataset in the right somatomotor cluster (motion datasets; 5 components; paired correlation coefficient: 0.83 ± 0.17). Other conventions follow Figure A1.

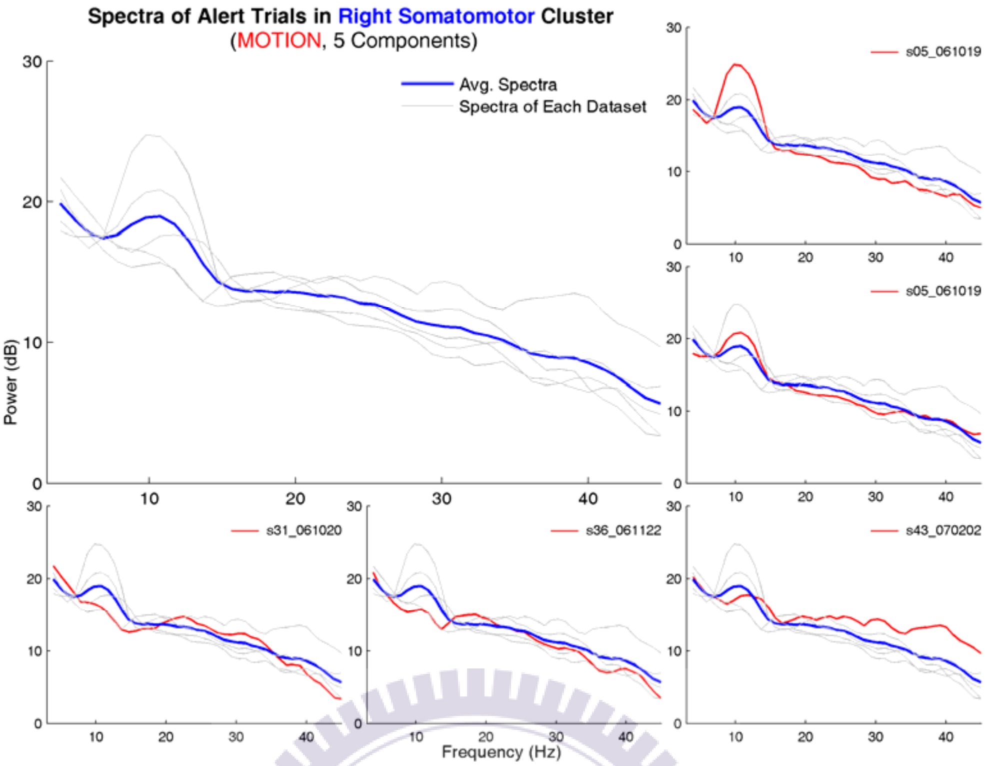

Figure A38: Tonic power spectra of alert trials in the right somatomotor cluster (motion datasets). Other conventions follow Figure A2.

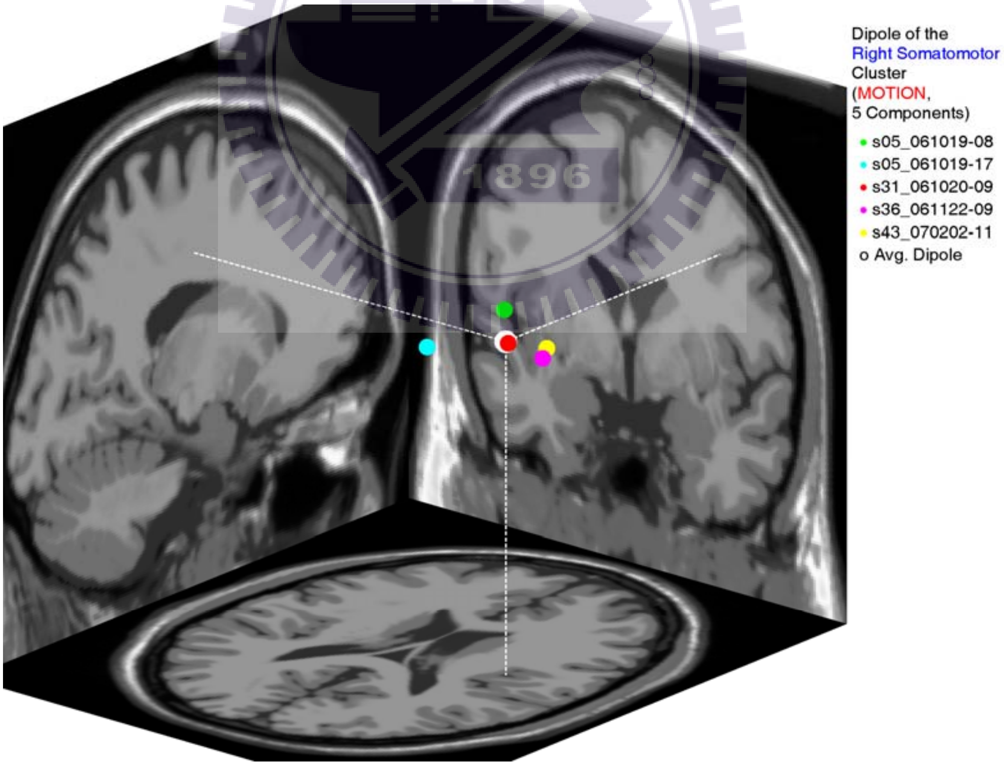

Figure A39: The locations of dipoles in the right somatomotor cluster (motion datasets). Other conventions follow Figure A3.

TABLE A15: TALAIRACH COORDINATES OF THE RIGHT SOMATOMOTOR CLUSTER (MOTION DATASETS)

Dataset	Component	Talairach Coordinates		
		X	Y	Z
s05_061019	8	25.93	1.54	40.28
s05_061019	17	27.70	-37.31	41.39
s31_061020	9	51.27	-26.21	44.30
s36_061122	9	41.86	0.35	28.96
s43_070202	11	40.34	4.19	30.58
Mean		37.42	-11.49	37.10
Standard Deviation		10.57	18.97	6.88

A.2.2.6 The Occipital Midline Cluster

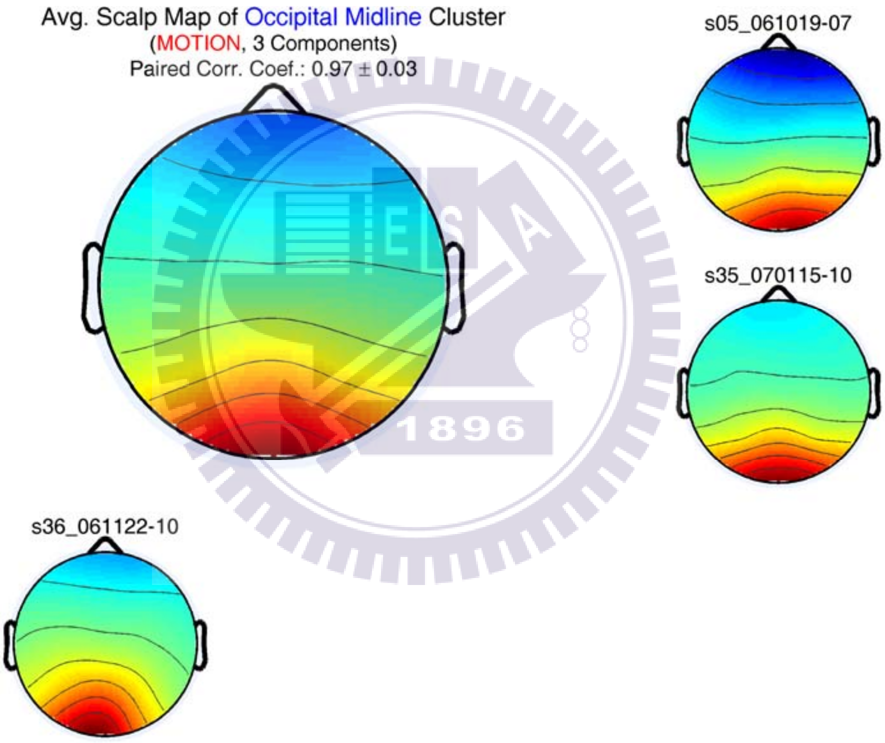

Figure A40: The ICA scalp map of each dataset in the occipital midline cluster (motion datasets; 3 components; paired correlation coefficient: 0.97 ± 0.03). Other conventions follow Figure A1.

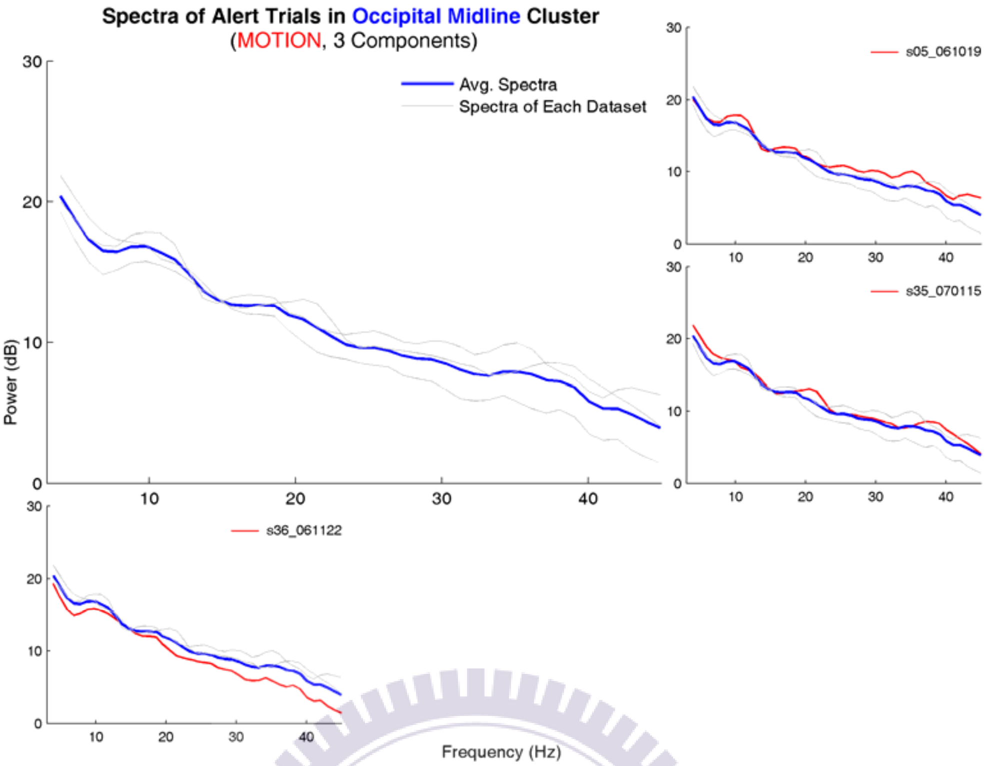

Figure A41: Tonic power spectra of alert trials in the occipital midline cluster (motion datasets). Other conventions follow Figure A2.

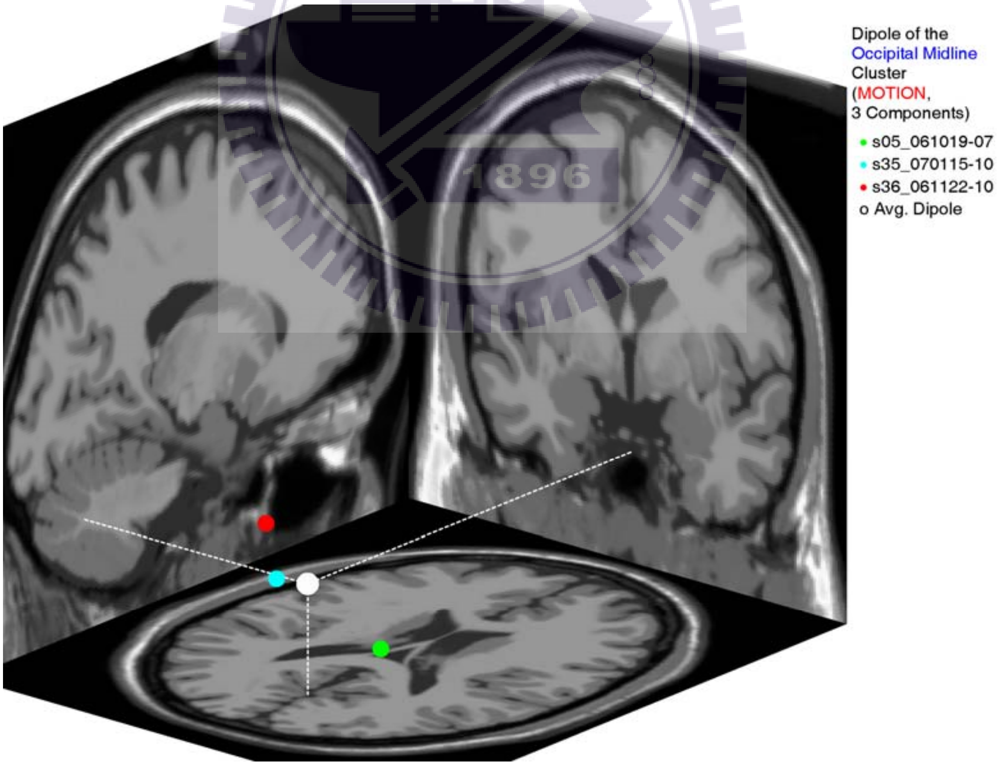

Figure A42: The locations of dipoles in the occipital midline cluster (motion datasets). Other conventions follow Figure A3.

Table A16: Talairach Coordinates of the Occipital Midline Cluster (Motion Datasets)

Dataset	Component	Talairach Coordinates		
		X	Y	Z
s05_061019	7	10.78	-44.05	-49.52
s35_070115	10	0.34	-80.06	-20.96
s36_061122	10	-5.78	-77.10	-7.33
Mean		1.78	-67.07	-25.94
Standard Deviation		8.37	19.99	21.53

A.2.2.7 The Bilateral Occipital Cluster

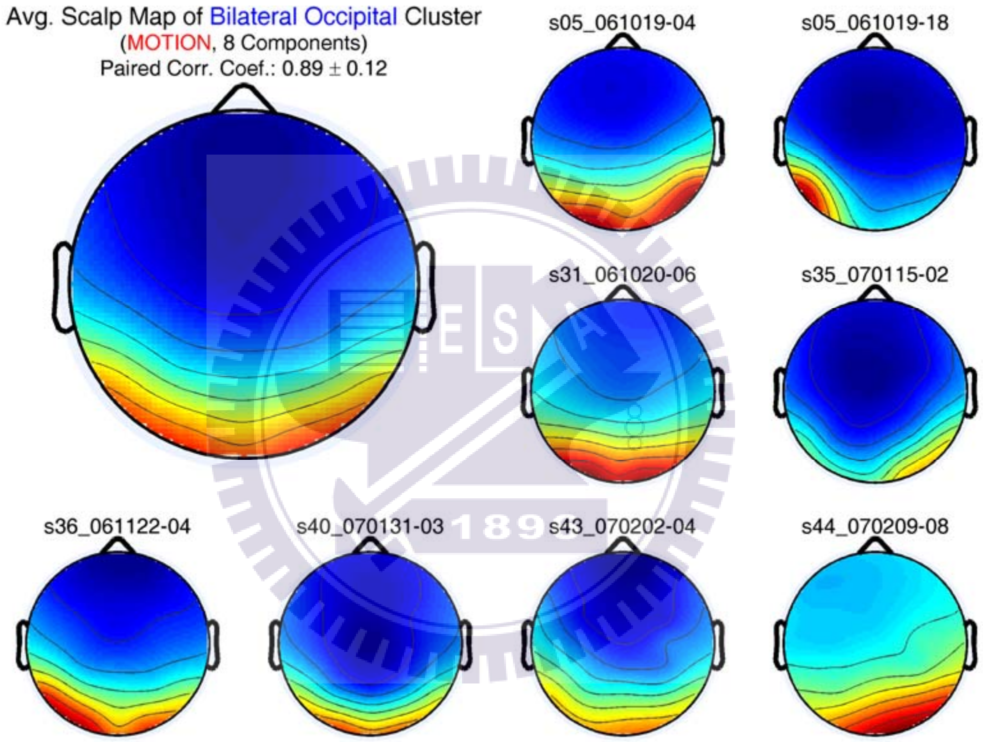

Figure A43: The ICA scalp map of each dataset in the bilateral occipital cluster (motion datasets; 8 components; paired correlation coefficient: 0.89 ± 0.12). Other conventions follow Figure A1.

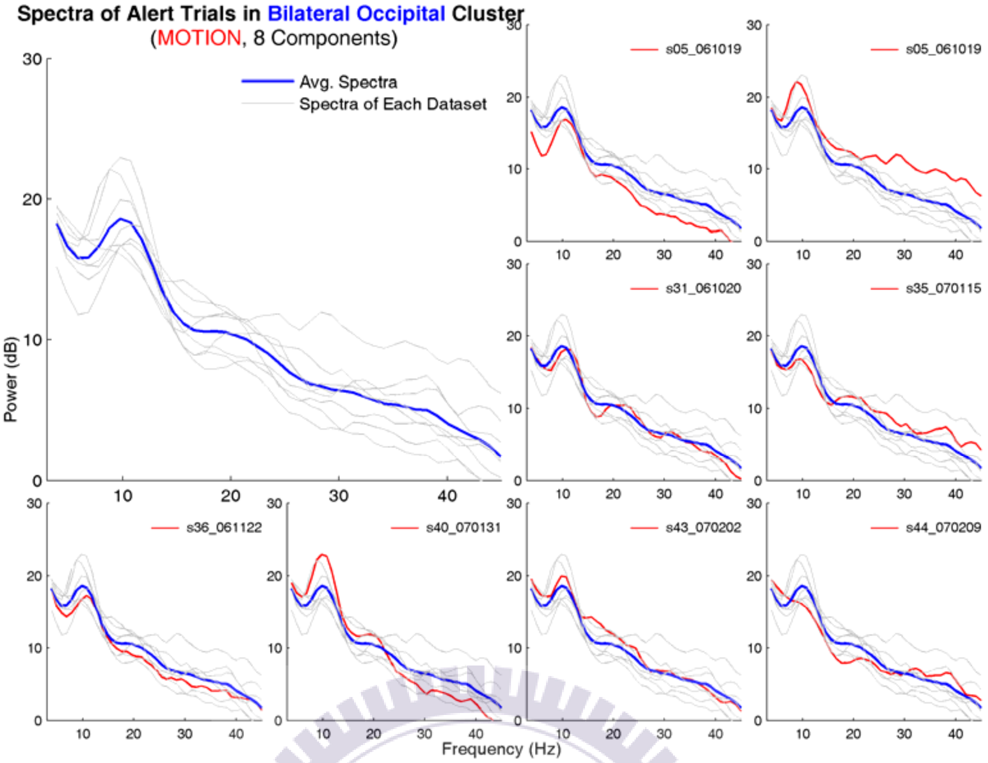

Figure A44: Tonic power spectra of alert trials in the bilateral occipital cluster (motion datasets). Other conventions follow Figure A2.

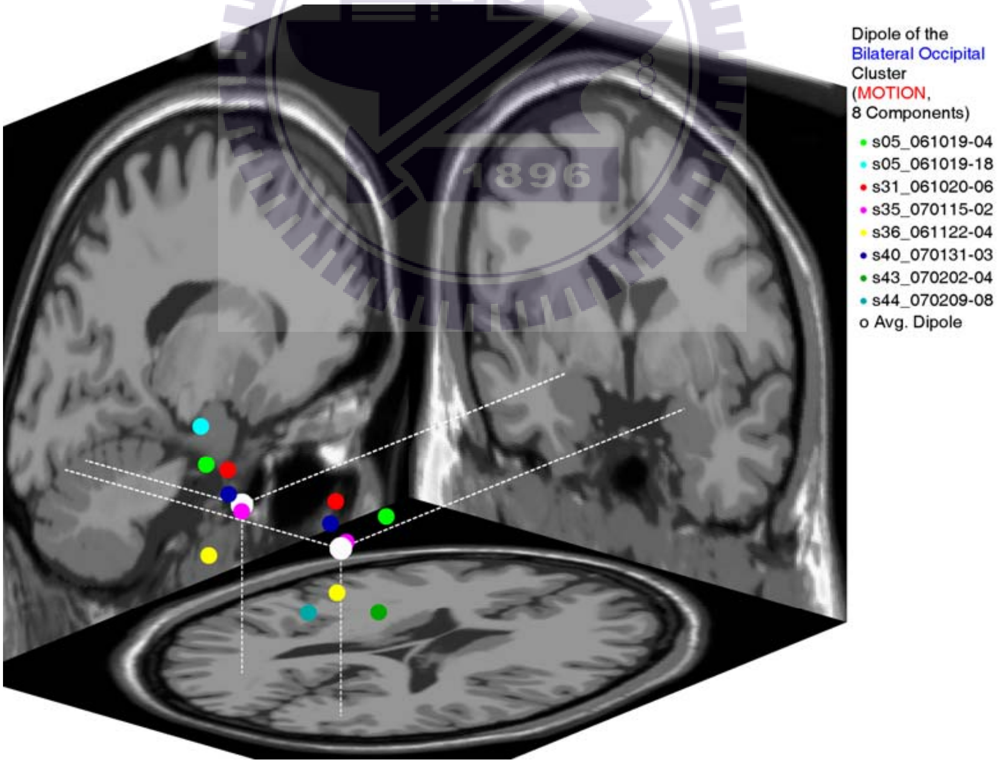

Figure A45: The locations of dipoles in the bilateral occipital cluster (motion datasets). Other conventions follow Figure A3.

TABLE A17: TALAIRACH COORDINATES OF THE BILATERAL OCCIPITAL CLUSTER (MOTION DATASETS)

Dataset	Compo-nent	Talairach Coordinates (Left)			Talairach Coordinates (Right)		
		X	Y	Z	X	Y	Z
s05_061019	4	-36.68	-68.94	0.58	36.90	-69.55	0.61
s05_061019	18	-50.78	-54.90	4.79	--	--	--
s31_061020	6	-22.09	-75.74	3.96	22.18	-76.11	3.98
s35_070115	2	-21.27	-70.66	-9.28	21.48	-71.01	-9.26
s36_061122	4	-26.16	-81.05	-19.79	26.20	-81.48	-19.77
s40_070131	3	-20.83	-77.16	-2.31	20.91	-77.51	-2.30
s43_070202	4	-2.40	-29.54	-46.47	--	--	--
s44_070209	8	--	--	--	9.39	-75.86	-30.57
Mean		-25.74	-65.43	-9.79	22.84	-75.26	-9.55
Standard Deviation		14.99	17.92	18.31	8.90	4.37	13.30

A.2.2.8 The Tangential Occipital Cluster

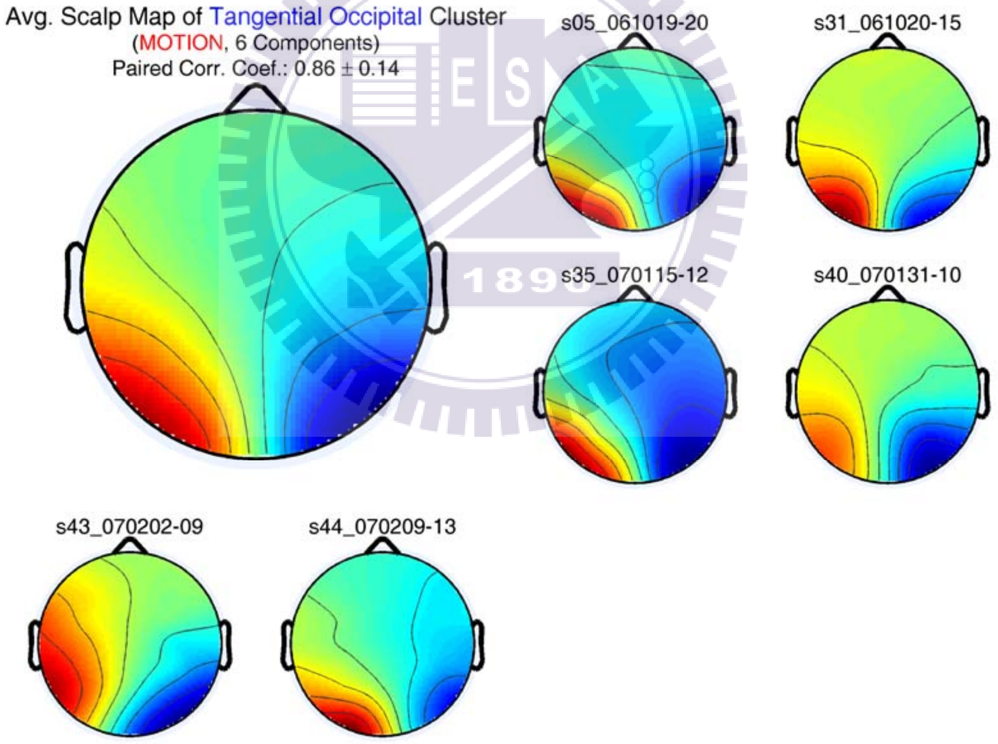

Figure A46: The ICA scalp map of each dataset in the tangential occipital cluster (motion datasets; 6 components; paired correlation coefficient: 0.86 ± 0.14). Other conventions follow Figure A1.

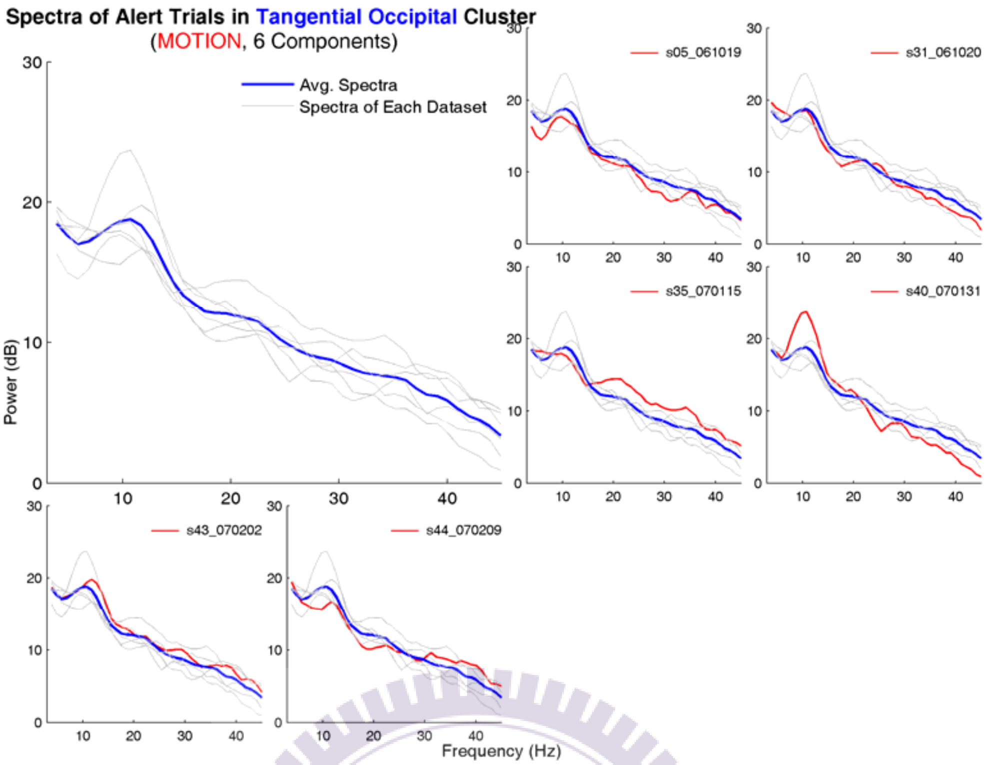

Figure A47: Tonic power spectra of alert trials in the tangential occipital cluster (motion datasets). Other conventions follow Figure A2.

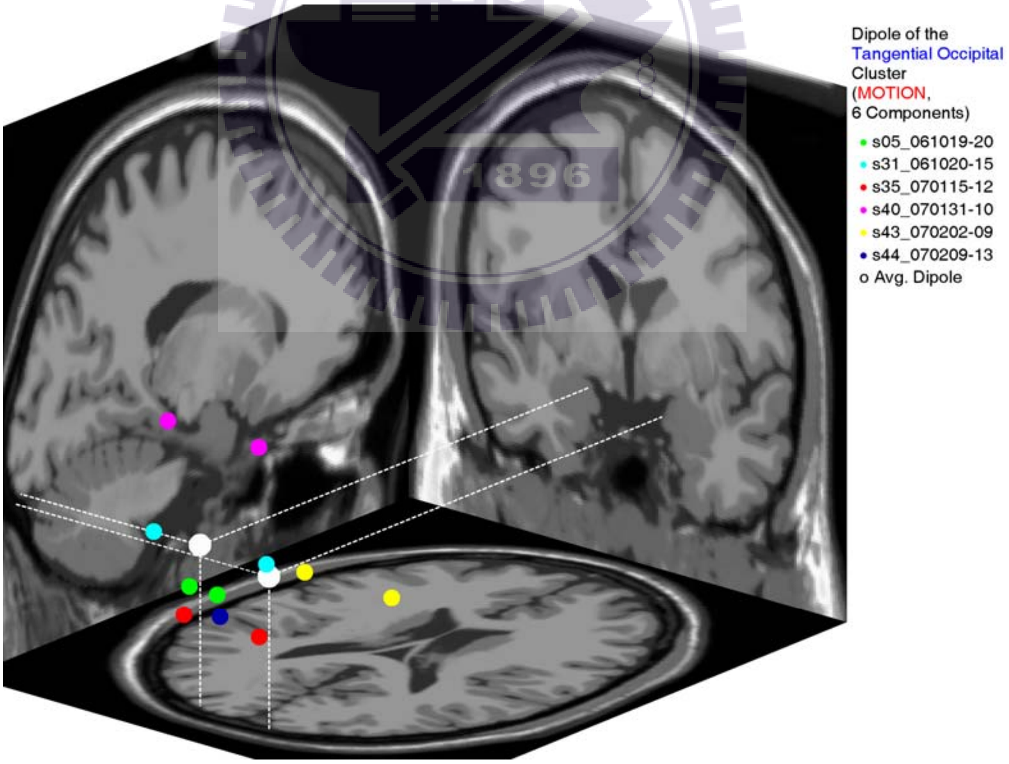

Figure A48: The locations of dipoles in the tangential occipital cluster (motion datasets). Other conventions follow Figure A3.

TABLE A18: TALAIRACH COORDINATES OF THE TANGENTIAL OCCIPITAL CLUSTER (MOTION DATASETS)

Dataset	Compo-nent	Talairach Coordinates (Left)			Talairach Coordinates (Right)		
		X	Y	Z	X	Y	Z
s05_061019	20	-5.93	-113.71	-14.99	5.41	-113.80	-14.99
s31_061020	15	-23.29	-109.79	-3.84	22.81	-110.17	-3.82
s35_070115	12	-15.61	-105.62	-27.45	15.25	-105.88	-27.44
s40_070131	10	-18.83	-106.50	30.00	18.35	-106.81	30.02
s43_070202	9	-17.48	-46.45	-33.04	18.15	-46.75	-33.03
s44_070209	13	--	--	--	3.21	-110.29	-22.85
Mean		-16.23	-96.41	-9.87	13.86	-98.95	-12.02
Standard Deviation		6.42	28.11	24.99	7.82	25.73	22.98